UNIVERSITY OF CALIFORNIA
SANTA CRUZ

# VARIATIONS OF ATMOSPHERIC CHEMICAL SYSTEMS ON VENUS AND THE ICE SHELL ON ENCELADUS

A dissertation submitted in partial satisfaction
of the requirements for the degree of

DOCTOR OF PHILOSOPHY

In

EARTH SCIENCES

by

**Wencheng Shao**

June 2022

The Dissertation of Wencheng Shao
is approved:

_____
Professor Xi Zhang, chair

_____
Professor Francis Nimmo

_____
Professor Patrick Y. Chuang

_____
Professor Bruce Bills

_____
Peter Biehl
Vice Provost and Dean of Graduate Studies

# Table of Contents

# List of Figures

# List of Tables

# Abstract

Variations of Atmospheric Chemical Systems on Venus and the Ice Shell on Enceladus

by

Wencheng Shao

The principal theme of this thesis is to see the planetary processes underlying observable variations. Various planetary processes in atmosphere, surface and interior exert long-term or short-timescale influence on the superficial properties that can be easily observed. This thesis combines observations with theoretical modelling to mine out the essential information of the Venus atmosphere and Enceladus's ice shell and promote the understanding of variations and evolution of our Solar System.

The Venus atmosphere is essential for understanding why Earth and Venus have evolved so differently even though they are similar in mass and radius. However, the complicated coupling among atmospheric dynamics, chemistry and clouds on Venus is still not well investigated. Using chemical-transport models (CTMs), I aimed to disentangle the effects from various atmospheric processes and guide observations of future Venus missions (DAVINCI+, VERITAS and EnVision).

Recent ground observations from TEXES/IRTF have for the first time revealed the co-evolution of $SO_2$ and $H_2O$ at the cloud top of Venus. The two species exhibit a temporal anti-correlation. I used a one-dimensional CTM to investigate the

mechanism of this anti-correlation. I found that the anti-correlation can originate from the sulfur photochemistry in the middle atmosphere, while the variations can be caused by the lower-atmosphere perturbations. Eddy diffusion alone cannot explain the observations. This study emphasizes the urgent need of detecting the cloud layer and the deep atmosphere of Venus.

The instrumentation TEXES/IRTF also found a two-peak feature in the local-time distribution of $SO_2$ at the cloud top, consistent with SPICAV/VEx observations. I developed a two-dimensional CTM and connected it to a Venus GCM to investigate this feature. My work revealed that the two peaks can be explained by the combination of the semi-diurnal tides and the retrograde superrotating zonal (RSZ) flow. SOIR/VEx also observed a statistical difference between terminators for CO in the upper atmosphere. From my simulations, this difference can be explained by the transition from the RSZ flow to the sub-solar to anti-solar (SS-AS) circulation. My work also discussed mechanisms underlying the local-time distributions of other species and implied a complex coupling of photochemistry and dynamics in the Venus mesosphere.

The Cassini flyby observed that Enceladus currently experiences a high surface heat flow. This leads to the question whether its ice shell is in steady state or its sub-surface ocean is freezing with time. To support the steady state of the ice shell, amounts of endogenic heat are required, which are currently thought coming from tidal dissipation. However, the exact process that produces sufficient tidal dissipation to match the observations remains elusive. I used a libration model to investigate the

heating effect of the diurnal forced libration. I found that although the forced libration enhances the tidal dissipation in the ice shell, the total heating in the shell is still insufficient to match the observed surface heat loss. If Enceladus is in steady state, there should exist a large heat source beneath the shell, either in the ocean or in the core. If in steady state, Enceladus is likely to be in a stable thermal equilibrium, which resists small perturbations on the ice shell. This implies that thermal runaway or episodic heating is unlikely to originate from the librations of the ice shell.

# Acknowledgements

In the last four years, at many times, I truly felt that acquiring a PhD degree is not easy. Even though I had a master degree before my journey in UC Santa Cruz, I was like a novice knowing poorly about scientific research and had to learn amounts of expertise in my PhD. Thanks to all the wonderful and excellent people I encountered in my PhD, at this moment, I finally standing at the starting line of my research career.

I was fortunate enough to work with a kind, patient advisor with encyclopedic knowledge in my PhD. I majored in atmospheric science in my bachelor and master studies, so it is a big challenge for me to step into the planetary science field. Xi, the advisor of my PhD thesis, has led me to step carefully and firmly into this field. Looking back on the four-year achievements in my PhD, each of them has received a great amount of instructions and assistance from Xi. One recent example is my postdoctoral application, which owes a lot of credits to Xi. Expressing my gratitude to him here is definitely the least thing I can do right now. I hope in the future I will get a chance to repay him.

In my second project, I also encountered the problem that I stepped into a brand-new field where I am not well equipped. However, Francis advised me with great patience in this project and led me step by step out of the difficulty. Like walking from aridity to fruitfulness, I greatly enjoyed this scientific journey. This journey extended my view on planetary science and enlarged my knowledge base. I foresee that this experience will continue benefiting my research road in the future.

My thesis reading committee Patrick and Bruce have kept the pursuing of my PhD always on track. The constructive advice and questions they provided in my qualified exam and annual progress report have further improved my understanding of my research. I am sincerely grateful for their important contributions to my PhD thesis.

When I started the study of the Venus atmosphere, Carver has offered amounts of help to me. I learned the chemical model from him, and I received the countless instructions and advice from him. When I was stressed by the qualified exam, Carver was there by my side to cheer me up. I owe many thanks to him. I am always looking forward to seeing him in conferences and then just having a casual conversation.

Therese, João and I have collaborated closely on the Venus science. They have provided great help on my research. They shared the observation and simulation data with me, and we discussed scientific and technical problems together. Without them, my Venus publications would not be achieved. I feel grateful for their contributions and meanwhile honored to collaborate with and learn from them.

This short article cannot cover all of my thanks. Though, I would like to thank many graduate students in the EPS department including Coby, Jack, Szilard, Brynna, Linfeng, Rachel, Nathan, Nick, Will and Jason, and many postdocs including Xinting, Laurent and Josh. I owe great thanks to Amy, Jennifer, Grace and Lisa for kindly assisting my graduate studies at UC Santa Cruz. And I want to give special thanks to Huazhi and Cheng for helping me on the SNAP model and to my friends in other

departments of UC Santa Cruz including Kejun and Yan who offered great help when I am struggling with the difficulty of life. I am also grateful to Shidong, my good friend in China, for the casual conversations we had in the last four years, which really relieved my stress. Finally, I would like to convey my gratitude to my parents in China for the tremendous worries they have for me and the wordless support they provide to me. What you have done is invaluable for me!

**Previously Published Material**

The text of this thesis includes reprints of the following previously published material:

Chapter I: Shao, W. D., Zhang, X., Bierson, C. J., & Encrenaz, T. (2020). Revisiting the Sulfur-Water Chemical System in the Middle Atmosphere of Venus. *Journal of Geophysical Research: Planets*, *125*(8), e2019JE006195. https://doi.org/10.1029/2019JE006195

Chapter II: Shao, W. D., Zhang, X., Mendonça, J., & Encrenaz, T. (2022). Local-time Dependence of Chemical Species in the Venusian Mesosphere. *The Planetary Science Journal*, *3*(1), 3. https://doi.org/10.3847/PSJ/ac3bd3

Chapter III: Shao, W. D., & Nimmo, F. (2022). An investigation of libration heating and the thermal state of Enceladus's ice shell. *Icarus*, *373*, 114769. https://doi.org/10.1016/j.icarus.2021.114769

# Chapter I. Co-evolution of $SO_2$ and $H_2O$ in the middle atmosphere of Venus

## 1.1 Introduction

The sulfur cycle is one major part of the complicated chemistry in the Venus atmosphere. (Yung & DeMore, 1982). Sulfur oxides react with water and form the sulfuric acid clouds at 60-70 km (Young, 1973; Hansen & Hovenier, 1974). Those clouds block the ultraviolet photons globally and separate the Venus atmosphere into two distinct regions in terms of tracer transport and chemistry. The lower atmosphere is characterized by thermochemistry and vigorously convective mixing. The upper part, usually termed as the middle atmosphere ranging from 60 to 100 km, is stably stratified, and photochemistry plays an important role. Previous work (e.g., Yung & DeMore, 1982; Mills, 1998; Zhang et al., 2012; Krasnopolsky, 2012, 2013, 2018) used one-dimensional photochemistry-transport models to explain species abundances in the middle atmosphere. Those models can explain vertical profiles of species like HCL, OCS, $SO_2$ and SO. But not much effort has been put forth on explaining variability of those species.

The Pioneer Venus spacecraft and the International Ultraviolet Explorer observed that $SO_2$ mixing ratio at the cloud top (~70 km) decreases by an order of magnitude during 1970s and 1980s (Esposito, 1984; Esposito et al., 1988; Na et al., 1990). The SPICAV instrument onboard the Venus Express spacecraft observed a

secular increase in $SO_2$ at the cloud top between mid-2006 and 2007 (Marcq et al., 2013) and then an overall decrease from 2007 to 2014 (Marcq et al., 2013, 2019b; Vandaele et al., 2017). Ground-based observations from the TEXES high-resolution imaging spectrometer at the NASA Infrared Telescope Facility (IRTF) also detected long-term variations of $SO_2$ at 64 km (near the cloud top) in 2012-2019 (Encrenaz et al., 2016, 2019a). The SPICAV and the TEXES data also show that $SO_2$ above or near the cloud top has large short-term and spatial variations (Encrenaz et al., 2012, 2013, 2016; Vandaele et al., 2017). For water, ground-based telescopes found temporal variations in the disk-integrated $H_2O$ abundance (Sandor & Clancy, 2005; Encrenaz et al., 2016, 2019a). But TEXES discovered that $H_2O$ at 64 km, unlike $SO_2$, exhibits relatively uniform spatial distribution over the Venus disk (Encrenaz et al., 2012, 2013).

Although one-dimensional models can explain the observed vertical profiles of $SO_2$ in the middle atmosphere through eddy diffusion and photochemistry (e.g., Yung and DeMore 1982; Mills 1998; Zhang et al., 2012; Krasnopolsky, 2012, 2013, 2018), mechanisms underlying horizontal and temporal variations of sulfur species and water are still not well understood. Proposed explanations include middle-atmospheric photochemistry (e.g., Parkinson et al. 2015; Vandaele et al., 2017) and flux variations from the lower atmosphere due to either periodic volcanic injections (e.g., Esposito, 1984; Esposito et al., 1988) or atmospheric dynamical fluctuations (e.g., Cottini et al., 2012; Marcq et al., 2013). Discriminating these mechanisms

requires detailed sulfur-water chemical models and detailed observations in high temporal and spatial resolutions.

Encrenaz et al. (2019b; 2020) simultaneously observed variations of $SO_2$ and $H_2O$ at 64 km. These observations range from 2012 to 2019 and are made by TEXES in the spectral range around 7.4 $\mu m$. These observations show not only temporal variations of disk-integrated abundances but also a seemingly temporal anti-correlation between $SO_2$ and $H_2O$. The evidence of this anti-correlation is not very clear in Encrenaz et al. (2019a), but with more data taken recently the correlation is stronger (Encrenaz et al., 2019b, 2020). The cause for this anti-correlation is unknown. Parkinson et al. (2015) (hereafter P15) used the one-dimensional chemistry-diffusion model in Zhang et al. (2012) to study the sulfur-water chemical system in the middle atmosphere. It was found that the system is extremely sensitive to the middle cloud top mixing ratios of $SO_2$ and $H_2O$ at 58 km. But mechanisms of this sensitivity are not well explored. Bierson and Zhang (2020) used a photochemical model describing the full atmosphere of Venus and pointed out that sulfur species abundances in the middle atmosphere are very sensitive to the vertical transport in the lower and middle clouds. The new TEXES data provide a unique opportunity to revisit the sulfur-water chemical system and understand the co-evolution of $SO_2$ and $H_2O$ in the Venus atmosphere in detail.

Using a one-dimensional chemistry-diffusion model, we explore the mechanisms underlying the anti-correlation and variations of $SO_2$ and $H_2O$ from TEXES in this study. We find that the sulfur-water chemical system has three chemical regimes. We

show that there is no chemical bifurcation claimed in previous studies (e.g., P15). We also point out that the $SO_2$ self-shielding effect plays an important role in this system. Combining our model with the TEXES data, we find that sulfur chemistry in the middle atmosphere accounts for the long-term anti-correlation of $SO_2$ and $H_2O$. Eddy mixing variations alone cannot produce the observed anti-correlation of both species. The temporal variations of $SO_2$ and $H_2O$ at the observed altitude (64 km) are linked to variations of mixing ratios and fluxes at the middle cloud top (58 km). This implies the observed variability probably originates from processes inside the clouds or from the lower atmosphere.

### 1.2 Model Description

In this study we use the JPL/Caltech Kinetics Venus model (e.g., Yung & DeMore, 1982; Mills, 1998; Zhang et al., 2012), as was used in P15. This chemical kinetics model has 51 species, 41 photodissociation reactions and over 300 neutral reactions. The model details are described in Zhang et al. (2012). This is the same model used by P15, and following P15 we set the lower boundary at 58 km, the middle cloud top (Knollenberg & Hunten, 1980). Below this altitude the middle and lower cloud layers have low static stability, while above it the Venus atmosphere is stably stratified (Tellman et al., 2009; Imamura et al., 2017; Limaye et al., 2018). To explore the parameter space of the sulfur-water chemical system, we vary lower boundary mixing ratios of two parent species—$SO_2$ and $H_2O$—that are transported upward from the middle cloud region. The range of $SO_2$ lower boundary mixing ratio

is 1-75 ppm and that of $H_2O$ is 1-35 ppm, covering the ranges of two species in P15. The temperature, pressure, total number density and eddy diffusion profiles are all the same as Zhang et al. (2012) and P15.

Above 80 km, the volume mixing ratio of $SO_2$ has been observed to increase with height, implying a high-altitude sulfur source (e.g., Sandor et al., 2010; Belyaev et al., 2012). This source may be sulfuric acid or poly-sulfur species (Zhang et al., 2010; 2012). In this study we only use sulfuric acid as the upper sulfur source, same as in P15. Note that the amount of sulfuric acid in the upper atmosphere required to match the sulfur inversion does exceed the upper limits from ground based observations (Sandor et al., 2012). But using poly-sulfur instead or even not including any upper sulfur source (thus no inversion above 80 km) does not alter our conclusions in this paper (see discussions in Section 1.4.1).

The chemical model we use in this study solves the one-dimensional atmospheric continuity equation:

$$\frac{\partial X}{\partial t} = e^{\xi}\frac{\partial}{\partial z}\left(e^{-\xi}K_{zz}\frac{\partial X}{\partial z}\right) + \frac{P-L}{n} \qquad (1.1)$$

(e.g., Zhang et al., 2013). Here $X$ is the volume mixing ratio of a chemical species. $\xi = z/H$, and H is the pressure scale height of the background atmosphere. $K_{zz}$ is the eddy diffusivity. $P$ and $L$ are the total production and loss rates respectively. $n$ is the number density of the background atmosphere. The first and second terms in the right hand side are the eddy diffusion and net production respectively. The molecular diffusion is ignored below the homopause, ~125 km, on Venus. When the chemical

system reaches the steady state, the eddy diffusion and net production should balance each other for every species.

The chemistry-diffusion system is usually numerically stiff as the chemical reaction rates could differ by several orders of magnitude. This system can be solved using an implicit Euler time stepping scheme, allowing the time step to exponentially increase in the time marching. A traditional convergence criterion is to check the abundance differences of the chemical species in two successive time steps. If the relative difference is sufficiently small, the model is considered to have reached the steady state. This was the criterion used in P15. Using the same model setup and the traditional convergence criterion, we can reproduce the simulation results of P15 (Fig. S1.2 (a-c)). However, we found that some cases do not actually reach the steady states defined by Equation (1), i.e., the eddy diffusion and net production terms do not exactly balance each other. See Appendix A and Fig. S1.1 for an example case and discussions.

To ensure that the model simulations reach the real steady state, in this study we reinforce a more rigorous convergence criterion, i.e., eddy diffusion and net production must equal in Equation (1) for every species. See an example case in the supplementary materials. Under this new criterion, we reached different simulation results and conclusions from that of P15 (see Fig. S1.2), as discussed in the following section.

### 1.3 $SO_2$ and $H_2O$ Variability above the Clouds

Following P15, Fig. 1.1 shows $SO_2$, $H_2O$ and $SO_3$ mixing ratio variations (hereafter "maps") at 80 km as a function of $SO_2$ and $H_2O$ mixing ratios at 58 km (the middle cloud top). Here we adopt the same parameter setting as that in P15 to make comparison. In P15's Fig. 9 and 10, $SO_2$ and $H_2O$ maps are "anti-symmetric" across mixing ratio ranges at 58 km (also see Fig. S1.2 (a-b) in this study). P15 found two regimes, high-$SO_2$-low-$H_2O$ and low-$SO_2$-high-$H_2O$. The transition between the two regimes is abrupt and is called the "chemical bifurcation". However, in our work the $SO_2$ and $H_2O$ maps (Fig. 1.1; Fig. S1.2 (d-f)) do not have these behaviors. First, the $SO_2$ and $H_2O$ maps are not "anti-symmetric". Second, it appears no chemical bifurcation or abrupt transition. Instead, the most salient feature is the non-monotonic behavior of $H_2O$ variations as a function of $SO_2$ at 58 km (Fig. 1.1b).

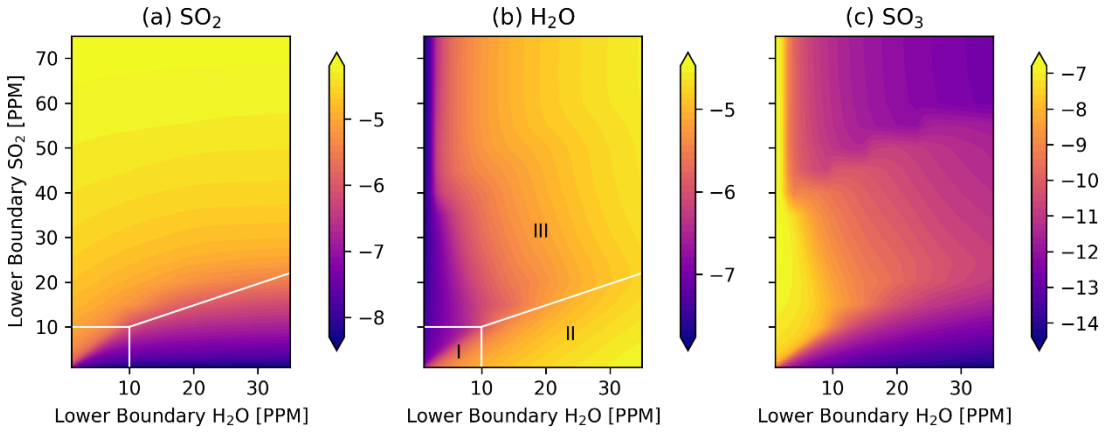


**Fig. 1. 1** Mixing ratios of $SO_2$ (a), $H_2O$ (b), and $SO_3$ (c) at 80 km as functions of $SO_2$ and $H_2O$ mixing ratios at 58 km. The white lines divide species maps into three regimes, I, II and III. Colors are volume mixing ratios on a logarithmic scale.

According to Fig. 1.1, we summarize behaviors of the chemical system at 80 km within three regimes:

I. Low-$SO_2$-low-$H_2O$. $H_2O$ mixing ratio decreases as $SO_2$ at 58 km increases. $SO_2$ mixing ratio decreases as $H_2O$ at 58 km increases. This pattern is similar to that of P15 except that two species do not have very abrupt changes in this regime, i.e., no "chemical bifurcation".

II. Low-$SO_2$-high-$H_2O$. $H_2O$ is oversupplied. $H_2O$ mixing ratio still decreases as $SO_2$ at 58 km increases. $SO_2$ mixing ratio remains relatively low and insensitive to changes in $H_2O$ at 58 km. $H_2O$ behavior is similar to that in regime I, but $SO_2$ behavior is different.

III. High-$SO_2$. $H_2O$ mixing ratio increases as $SO_2$ at 58 km increases. $SO_2$ mixing ratio decreases as $H_2O$ at 58 km increases. $SO_2$ behavior is similar to that regime I, but $H_2O$ behavior is different from that in regime I.

In all three regimes, the mixing ratio of an individual species at 80 km increases as its own mixing ratio at 58 km increases. This is primarily a result of eddy diffusive transport from the lower boundary. We also found that $SO_3$ and $H_2O$ maps (Fig. 1.1b and c) exhibit an anti-correlated pattern. This is possibly due to sulfuric acid formation:

$$SO_3 + 2H_2O \rightarrow H_2SO_4 + H_2O. \qquad (R1)$$

This reaction is the main chemical sink for both $SO_3$ and $H_2O$ near and insides the clouds. The supply of $H_2O$ is mainly from diffusion. Thus, in steady state, the reaction rate of (R1) should be roughly equal to the diffusion contribution to the $H_2O$ supply. If the diffusion contribution does not vary largely, the reaction rate of (R1)

should be roughly constant, and then increase of $H_2O$ (or $SO_3$) can cause decrease of $SO_3$ (or $H_2O$) .

Fig. 1.1b shows that $H_2O$ responds non-monotonically to changes in $SO_2$ at 58 km. From regime I or II to regime III, $H_2O$ at 80 km first decreases and then increases as $SO_2$ at 58 km increases. This behavior is due to the $SO_2$ self-shielding effect. $SO_3$ and $H_2O$ consume each other via reaction (R1). In all regimes, when $SO_3$ above the clouds decreases, $H_2O$ above the clouds increases. $SO_3$ above the clouds is mainly produced by $SO_2$ oxidation:

$$O + SO_2 + M \rightarrow SO_3 + M, \qquad (R2)$$

where $M$ is the background atmosphere. Reaction (R2) suggests that $SO_3$ production is affected by abundances of both atomic oxygen O and $SO_2$. The atomic oxygen O above the clouds is mainly produced by $SO_2$ photolysis:

$$SO_2 + hv \rightarrow SO + O. \qquad (R3)$$

Reaction (R3) suggests that atomic oxygen production is affected by $SO_2$ abundance and the amount of photons (or UV light intensity).

When $SO_2$ at the middle cloud top increases, $SO_2$ above the clouds increases. This increase produces more atomic oxygen via $SO_2$ photolysis (R3). $SO_2$ oxidation (R2) then increases $SO_3$ production due to increase of both $SO_2$ and atomic oxygen. Increased $SO_3$ consumes more $H_2O$. This is the chemistry in regimes I and II. Fig. 1.2 shows an example with $H_2O$ mixing ratio fixed as 10 ppm at 58 km. When $SO_2$ at 58

km increases from 1 to 10 ppm, at 80 km $SO_2$, atomic oxygen and $SO_3$ all increase while $H_2O$ decreases.

As $SO_2$ inside the clouds continues increasing, $SO_2$ at higher altitudes becomes abundant due to eddy transport. Abundant $SO_2$ absorbs many photons, and thus less photons reach lower altitudes such as 80 km. This limits atomic oxygen production via $SO_2$ photolysis (R3). Less atomic oxygen is produced, and this decreases $SO_3$ production via $SO_2$ oxidation (R2). Then sulfuric acid formation (R1) consumes less $H_2O$ and $H_2O$ is accumulated. In this process $SO_2$ absorption and photolysis at higher altitudes "shield" $SO_2$ photolysis at lower altitudes. This is the $SO_2$ self-shielding effect. This effect causes $H_2O$ behaviors in regime III. See the example in Fig. 1.2 where $H_2O$ at 58 km is fixed as 10 ppm. When $SO_2$ at 58 km increases from 10 to 50 ppm, at 80 km $SO_2$ increases, atomic oxygen and $SO_3$ both decrease due to the $SO_2$ self-shielding, and consequently $H_2O$ increases.

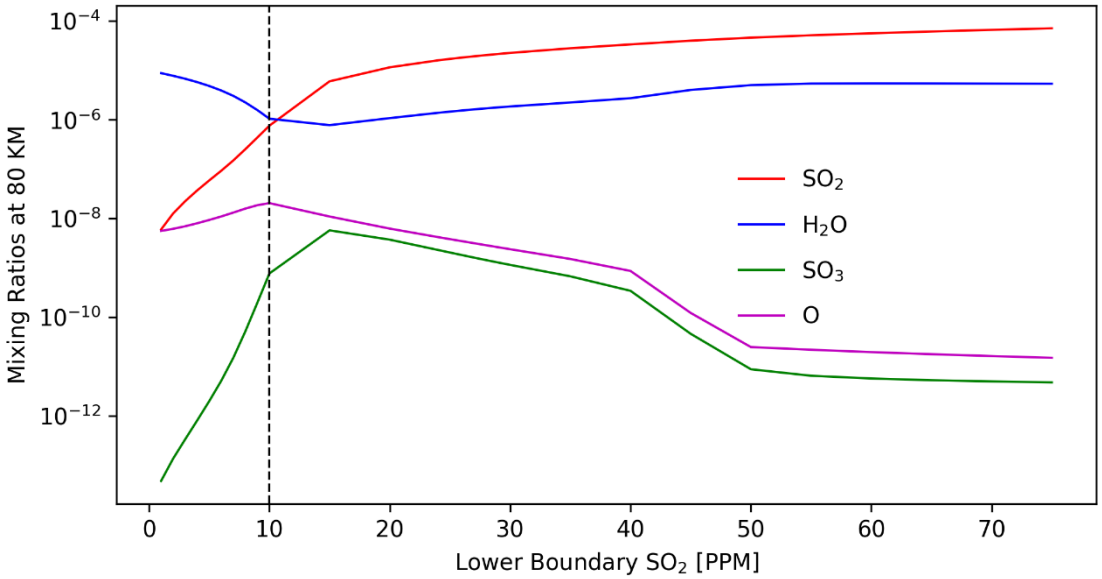


**Fig. 1. 2** $SO_2$, $H_2O$, $SO_3$ and atomic oxygen mixing ratios at 80 km vary with $SO_2$ mixing ratio at 58 km. $H_2O$ mixing ratio at 58 km is fixed as 10 ppm. The black dashed

line delimits regime I and regime III.

$SO_2$ mixing ratio at 80 km generally decreases as $H_2O$ at 58 km increases (Fig. 1.1a). This behavior is strong in regime I, weaker in regime III and almost negligible in regime II. Our analysis suggests that some $SO_3$-involved reactions are key for this behavior. These reactions convert $SO_3$ to $SO_2$ and are here called $SO_3$ pathways:

$$SO_3 + hv \rightarrow SO_2 + O, \quad (R4)$$

$$O + SO_3 \rightarrow SO_2 + O_2, \quad (R5)$$

$$S + SO_3 \rightarrow SO_2 + SO, \quad (R6)$$

$$S_2 + SO_3 \rightarrow S_2O + SO_2, \quad (R7)$$

$$SO + SO_3 \rightarrow 2SO_2. \quad (R8)$$

To investigate the role of these $SO_3$ pathways, we do a test in which we shut off all pathways (R4-R8) and see how the chemical system behaves. In our test cases, $SO_2$ lower boundary mixing ratios are all 9 ppm. We designed two groups with (control) and without (experimental) the $SO_3$ pathways, respectively.

Fig. 1.3 shows mixing ratio variations at 80 km in two groups. In the control group, $SO_2$ at 80 km decreases when $H_2O$ at 58 km increases from 1 to 10 ppm. This is because more $H_2O$ consumes more $SO_3$ and causes less $SO_2$ produced via the $SO_3$ pathways. When $SO_3$ pathways are not included (the experimental), $SO_2$ mixing ratio is not affected. Consequently $SO_2$ at 80 km remains low and insensitive to variations when $H_2O$ at 58 km increases from 1 to 35 ppm.

When $H_2O$ mixing ratio at 58 km is above 10 ppm, $H_2O$ is oversupplied. In this situation, $SO_3$ mixing ratio is low due to efficient sulfuric acid formation and $SO_3$ pathways (R4-R8) contribute little to the $SO_2$ production. As a result, $SO_2$ at 80 km in both the control and experimental groups remain low and insensitive to $H_2O$ variations at 58 km. This explains the $SO_2$ behavior in regime II.

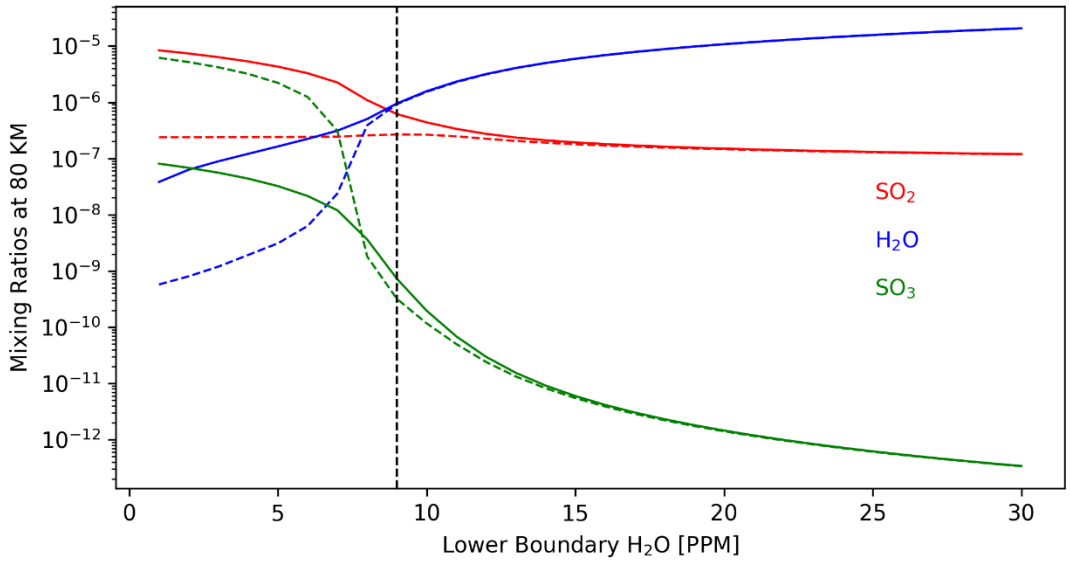


**Fig. 1. 3** The mixing ratios of $SO_2$ (red), $H_2O$ (blue), and $SO_3$ (green) at 80 km for two groups vary with $H_2O$ mixing ratio at 58 km. $SO_2$ mixing ratio at 58 km is fixed as 9 ppm. In the control group (solid lines) reactions (R4-R8) convert $SO_3$ to $SO_2$, while in the experiment group (dashed lines) these reactions are shut off. The black dashed line delimits regime I and II.

### 1.4 Comparison with the TEXES data

Encrenaz et al. (2019b; 2020) reported an anti-correlation of disk-averaged abundances of simultaneously observed $SO_2$ and $H_2O$ at ~64 ± 2 km (near the upper cloud top) in 2012-2019 from TEXES/IRTF. As shown in Fig. S1.5a and Fig. 1.6a, these data provide unique information about how the two parent chemical species vary together in the middle atmosphere. In particular, the apparent anti-correlation

between the disk-averaged $SO_2$ and $H_2O$ could be used to distinguish different proposed mechanisms for the long-term variation. Using our simple one-dimensional chemistry-diffusion model, here we specifically explore two possibilities. First, if the temporal variation of $SO_2$ and $H_2O$ is a result of perturbations below the middle cloud top (e.g. Esposito, 1984; Esposito et al., 1988), varying the lower boundary conditions in our model should be able to reproduce the anti-correlation. On the other hand, if the variation is due to changes in the vertical mixing inside the upper cloud (e.g., Lefevre et al., 2018, 2020), changing the eddy diffusivity in our model should be able to explain the data.

To compare our model with these disk-averaged observations, we set the latitude at $45°N$ and assume that the $SO_2$-$H_2O$ chemical system is in steady state at each individual observational time. The Venus atmosphere is highly variable on timescales of hours and days (e.g., Encrenaz et al., 2013). To isolate longer-period variations (which are more comparable to steady state simulations) we spatially average over the entire disk and temporally average over observations taken within 2 months. The chemical lifetimes of $SO_2$ and $H_2O$ at 64 km are generally less than two months.

### 1.4.1 Middle Cloud Top Variations

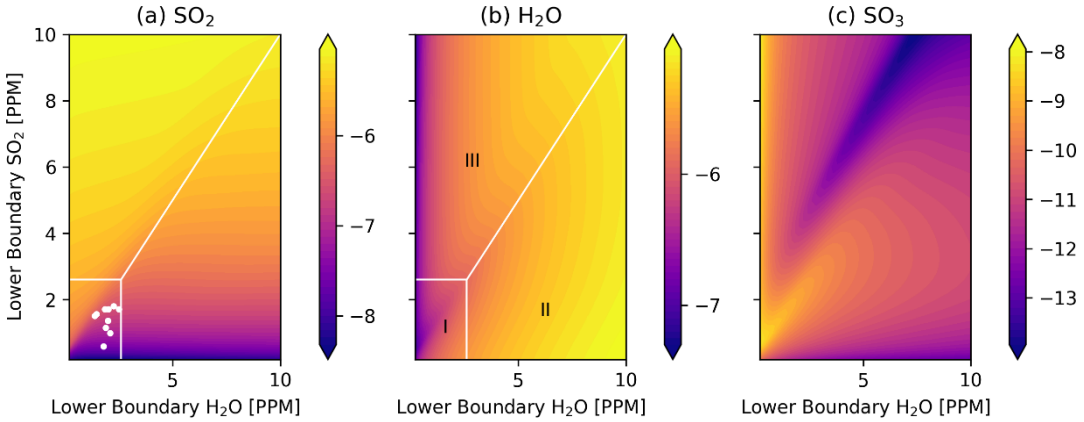


**Fig. 1. 4** Same as Fig. 1.1, but at 64 km and $45°N$. White dots are models that match the TEXES observations.

To test whether the variations of $SO_2$ and $H_2O$ come from the lower atmospheric processes, we first perform simulations by varying $SO_2$ and $H_2O$ mixing ratios at the middle cloud top (58 km) but fixing the eddy diffusivity. We analyze $SO_2$, $H_2O$ and $SO_3$ variations at 64 km to explore the parameter space (Fig. 1.4). There are also three chemical regimes at 64 km, similar to that in Fig. 1.1 where we showed the same species at 80 km. For example, in regime I at both altitudes, $SO_2$ decreases as $H_2O$ at 58 km increases, and $H_2O$ decreases as $SO_2$ at 58 km increases. But the regime boundaries are different between Fig. 1.1 and 1.4. The regime I in Fig. 1.4 only covers $H_2O$ and $SO_2$ at 58 km from 0-2.6 ppm, while regime I in Fig. 1.1 covers both species at 58 km from 0-10 ppm.

For each individual observational data point of $SO_2$ and $H_2O$ at 64 km, we fix the eddy mixing and carefully tune the $SO_2$ and $H_2O$ mixing ratios at the lower boundary of our model to match the disk-averaged TEXES observations. Fig. 1.5 shows our simulated $SO_2$ and $H_2O$ mixing ratio profiles. As altitude increases, $SO_2$

decreases by orders of magnitude below 80 km. $H_2O$ remains relatively constant within a factor of 2. These structures are consistent with measurements from SOIR onboard Venus Express (e.g., Belyaev et al., 2012; Bertaux et al., 2007). From 2012 to 2019, $SO_2$ mixing ratio below 80 km varies in a similar way to $SO_2$ at 64 km, consistent with the correlated observations from TEXES and SPICAV (Encrenaz et al., 2019a). $H_2O$ below 80 km also follows the same variation pattern as that at 64 km. In the region between 60 and 80 km, the primary sink for both $SO_2$ and $H_2O$ is sulfuric acid formation (R1). Above 90 km both $H_2O$ and $SO_2$ mixing ratios are supplied by our prescribed sulfur acid source. Note that removing this prescribed source hardly changes $SO_2$ and $H_2O$ profiles below 70 km (Fig. 1.5). There is some difference at 80 km between cases with and without the source, but this difference does not change three regimes discussed in Section 1.3 except that the transitions

among regimes could shift. In this section the mainly focused altitude region is below 70 km, the existence of this source is not important to our results.

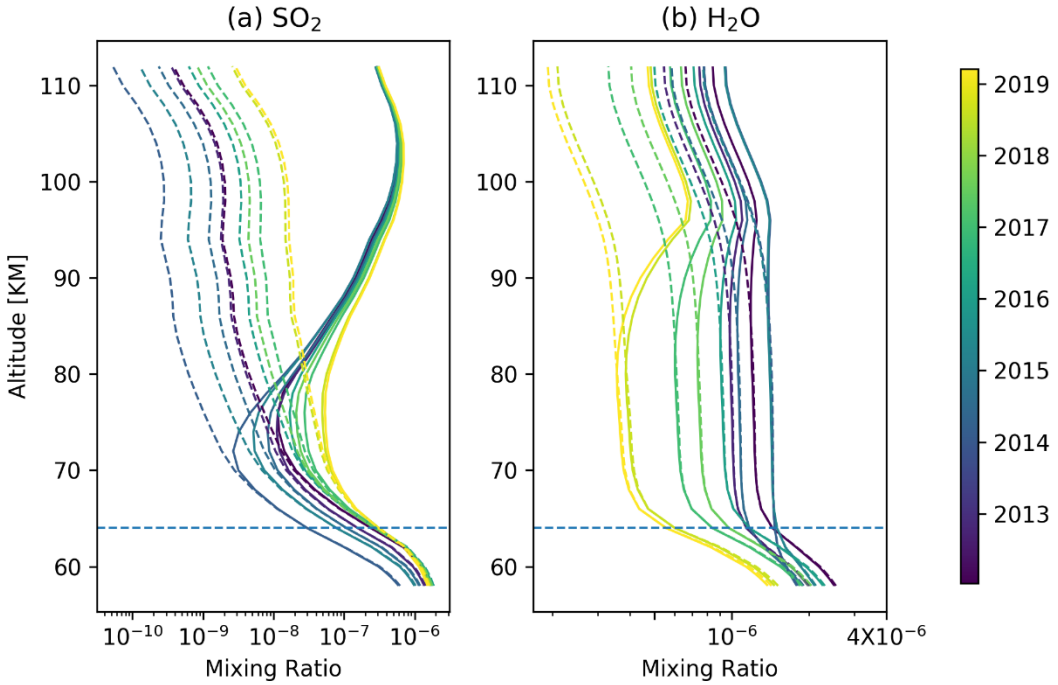


**Fig. 1. 5** Simulated vertical profiles of $SO_2$ (a) and $H_2O$ (b) mixing ratios consistent with the TEXES data at 64 km (horizontal dashed lines). Curves are colored by the observational dates. Solid curves are of cases with the prescribed upper source (sulfuric acid) and dashed curves are of cases without this source (i.e. no sulfuric acid photolysis).

Constrained by the TEXES data, the derived $SO_2$ and $H_2O$ mixing ratios at 58 km are shown in Fig. 1.6, along with the upward fluxes of two species at 58 km. Mixing ratio variations at 64 km can be divided into two periods: 2012-2015 and 2015-2019 (Fig. 1.6a; Encrenaz et al., 2019a). In 2012-2015 $SO_2$ at 64 km varies significantly, by a factor up to 5. $H_2O$ varies gently by a factor up to 1.5. In 2015-2019, $H_2O$ varies by a factor over 2, and $SO_2$ remains relatively constant. The two different periods at 64 km also exist at 58 km (Fig. 1.6b). This similarity between 58

km and 64 km suggests that eddy diffusion plays an important role in the system in addition to photochemistry below 80 km (e.g., Jessup et al., 2015).

The fluxes of two species at 58 km show similar temporal variations to mixing ratios at 64 km (see Fig. S1.5a and S5c). More interestingly, the two fluxes are strongly and positively correlated (Fig. 1.6c), and the correlation coefficient is 0.99. This linear-relationship feature for fluxes of two species is a result of the middle-atmosphere photochemistry in our model. Sulfuric acid formation (R1) is the major sink for $SO_2$ and $H_2O$ in the middle atmosphere. If there are no other sinks, then by mass conservation, the two fluxes have to both equal the sulfuric acid formation rate. In fact because some $SO_2$ is also lost to the formation of the poly-sulfur haze, the $SO_2$ flux is larger than the $H_2O$ flux (Fig. 1.6c).

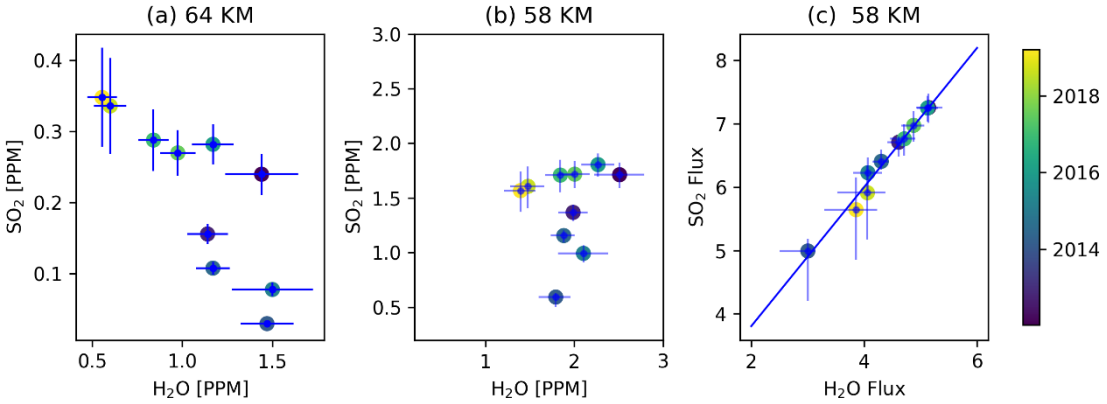


**Fig. 1. 6** Scatter plots of (a) the observed $SO_2$ and $H_2O$ mixing ratios at 64 km, (b) inferred mixing ratios at 58 km and (c) upward fluxes at 58 km. Points are colored by the observational dates. The two fluxes (not considering error bars) can be fit (with1-sigma error) by $y = (1.10 \pm 0.06)x + (1.61 \pm 0.25)$, where y and x are the $SO_2$ and $H_2O$ fluxes, respectively. Units of x, y and the intercept are $10^{11} cm^{-2} \cdot s^{-1}$. This fit is shown by the solid line in (c). The $SO_2$ and $H_2O$ fluxes are also correlated in this manner in all of our model simulations, not just those shown.

### 1.4.2 Origin of the Anti-correlation

The TEXES data show that $SO_2$ and $H_2O$ at 64 km are anti-correlated (Fig. 1.6a). The correlation coefficient is -0.80, and the linear regression slope is -0.27. But the inferred $SO_2$ and $H_2O$ at the middle cloud top (58 km) do not show a good linear correlation (Fig. 1.6b), implying that the anti-correlation behavior is not universal at all altitudes. This prediction can be tested in future observations. More importantly, the lack of a strong correlation between the two species at 58 km suggests that, although the variations of $SO_2$ and $H_2O$ at 64 km might come from the lower atmospheric processes, the anti-correlation between the two species has a different mechanism.

To diagnose the system, we first notice that the TEXES observations are well located in regime I, i.e., Low-$SO_2$-Low-$H_2O$ (Fig. 1.4a). In this regime, the $SO_2$ self-shielding effect is insignificant. $SO_2$ and $H_2O$ are linked by $SO_3$ via $SO_2$ oxidation (R2), sulfuric acid formation (R1) and $SO_3$ pathways (R4-R8). More $SO_2$ produces more $SO_3$ that consumes more $H_2O$. More $H_2O$ consumes more $SO_3$ that results in

less $SO_2$. It looks that the anti-correlation of $SO_2$ and $H_2O$ might just be a characteristic of the regime I chemistry.

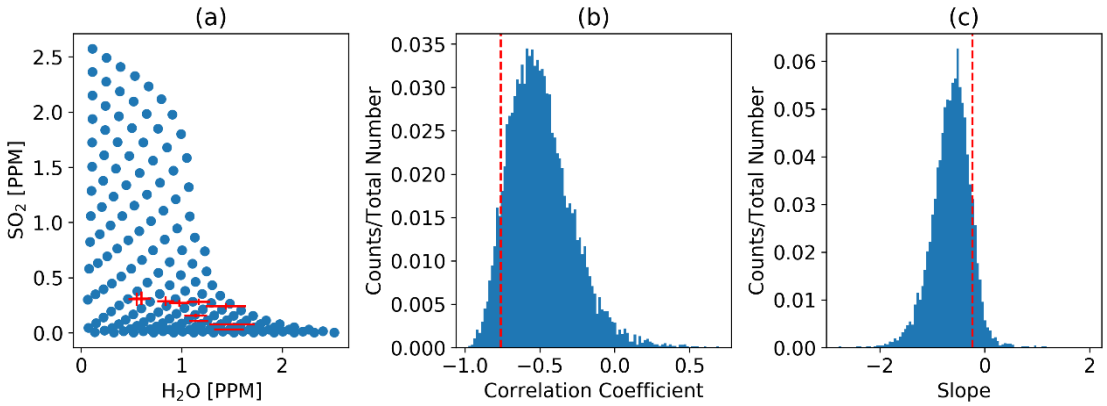


**Fig. 1. 7** (a) Scatter plot of the $SO_2$ and $H_2O$ mixing ratios at 64 km for all cases in the regime I (Fig. 1.4). Red crosses are the TEXES data with error bars. (b) Statistics of ten-case correlation coefficients and (c) linear regression slopes of $SO_2$ and $H_2O$ at 64 km from our model. In total we have 10 000 correlation coefficients and slopes. We use 100 bins to plot the statistical distributions. The red dashed lines are the values calculated from the TEXES data.

To test this idea, we do a statistical correlation analysis. First we run a suite of model cases in the regime I, and among these cases both $SO_2$ and $H_2O$ at 58 km are evenly spaced by 0.2 ppm between 0.2 and 2.6 ppm. Since we have ten observations, we randomly choose ten cases and calculate the correlation coefficient and the linear slope of $SO_2$ and $H_2O$ at 64 km. We repeat the above analysis for 10 000 times and obtain the distribution of correlation coefficients and slopes (Fig. 1.7b and c). 97.7% of correlation coefficients and slopes are negative, qualitatively consistent with the sensitivity test in Krasnopolsky (2018). The correlation coefficient peaks at -0.5, and the slope peaks at -0.8. This analysis shows that if $H_2O$ and $SO_2$ vary uniformly and independently at the middle cloud top, a negative correlation of $SO_2$ and $H_2O$ at 64 km would be expected due to the regime I chemistry. This suggests that sulfur

chemistry in the regime I together with the lower boundary variations can produce the anti-correlation of $SO_2$ and $H_2O$ at 64 km.

Fig. 1.7 shows that the observed correlation of $SO_2$ and $H_2O$ differs somewhat from the model's prediction. The observed value does not locate at the center of the distributions. Although there are uncertainties in the observations, this discrepancy could also suggest that there are some second-order processes involved. It is likely that the mixing ratios of $SO_2$ and $H_2O$ at 58 km do not follow a uniform distribution as assumed and may be somewhat correlated through atmospheric dynamics inside the middle clouds. Also, the exact location of the center of the distribution might depend on the choice of the eddy mixing profile in the model. But note that changing the eddy mixing alone would not produce the anti-correlation, as detailed below in Section 1.4.3. Future observations, both remote and in-situ, could help distinguish influences from these factors.

### 1.4.3 Eddy Mixing Change

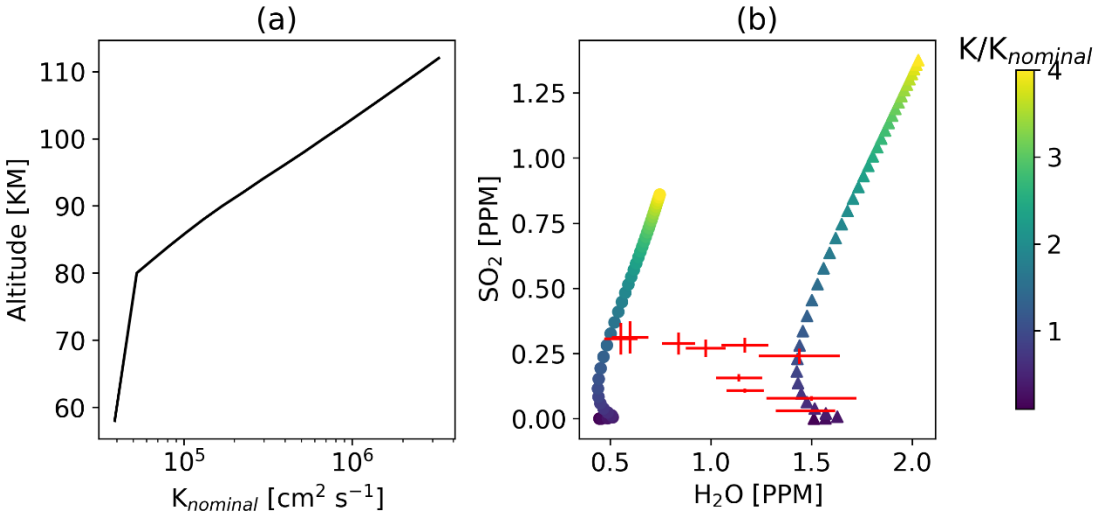


**Fig. 1. 8** (a) The nominal eddy diffusivity profile in our model. (b) Scatter plot of $SO_2$

and $H_2O$ mixing ratios at 64 km for various eddy diffusivity profiles. Diffusivity profiles vary from 0.1 to 4 times the nominal profile, as shown by colors. Circular markers are of cases with 1.0 ppm $SO_2$ and 1.0 ppm $H_2O$ at the lower boundary. Triangular markers are of cases with 1.7 ppm $SO_2$ and 2.5 ppm $H_2O$ at the lower boundary. Red crosses are the TEXES data with error bars.

Now we test whether the middle atmospheric dynamics can produce the variations and anti-correlation of $SO_2$ and $H_2O$ at 64 km. In the above cases we varied the lower boundary conditions and fixed the eddy diffusivity profile (nominal, Fig. 1.8a). The diffusivity profile is from Zhang et al. (2012), calculated based on measurements from Pioneer Venus (Von Zahn et al., 1979) and radio signal scintillations (Woo & Ishimaru, 1981). Here we fix the lower boundary conditions at 58 km but multiply this diffusivity profile by a constant factor ranging from 0.1 to 4, to explore the influence of the eddy mixing change on species mixing ratio variations at 64 km. We perform two sets of lower boundary conditions. In one set we use 1.0 ppm $SO_2$ and 1.0 ppm $H_2O$ at 58 km. In the other one we use 1.7 ppm $SO_2$ and 2.5 ppm $H_2O$ at 58 km. The results are shown in Fig. 1.8b. Varying eddy mixing alone above 58 km does change the mixing ratios of $SO_2$ and $H_2O$ at 64 km, but our simulations show that $SO_2$ is far more sensitive to the eddy mixing changes than $H_2O$. This difference in sensitivity of $SO_2$ and $H_2O$ to eddy mixing is qualitatively consistent with Krasnopolsky (2018) and may explain the greater variations of $SO_2$ than $H_2O$ over both space and time observed by TEXES (e.g., Encrenaz et al., 2013) and SPICAV (e.g., Vandaele et al., 2017). When we fix the lower boundary condition and vary the eddy mixing so that $SO_2$ at 64 km changes from 0 to 0.3 ppm, which is approximately the range of the observed $SO_2$ variations, $H_2O$ only varies by less than

30%. In contrast, the observed abundance of $H_2O$ has larger variations up to a factor of ~3. Also, when diffusivity increases in a large range from 0.1 to 4 times the nominal values, both $SO_2$ and $H_2O$ at 64 km generally increase. Thus, we conclude that even though the eddy mixing could vary with time above 58 km, the variations of eddy mixing alone cannot explain the observed variation range of $H_2O$ and the anti-correlation between $SO_2$ and $H_2O$ at 64 km.

### 1.5 Conclusions and Discussions

In this work we revisited the sulfur-water chemical system in the middle atmosphere of Venus, motivated by the recently and simultaneously observed $SO_2$ and $H_2O$ variations at ~64 km from TEXES/IRTF (Encrenaz et al., 2019b; 2020). Using a one-dimensional chemistry-diffusion model, we studied the co-evolution of $SO_2$ and $H_2O$ in the middle atmosphere of Venus for the first time. We first explored the variability of the chemical species in the system and the underlying mechanisms in a thorough way. We reported chemical regimes and mechanisms different from previous studies. Then we used our model to investigate the long-term anti-correlation of $SO_2$ and $H_2O$ observed by TEXES. We tested two possible mechanisms for the anti-correlation and provided implications of those TEXES observations.

The chemical system is highly dependent on $SO_2$ and $H_2O$ mixing ratios at the middle cloud top at 58 km. $SO_2$ and $H_2O$ mixing ratios above the clouds vary with mixing ratios at 58 km in three regimes: low-$SO_2$-low-$H_2O$ (regime I), low-$SO_2$-high-$H_2O$ (regime II) and high-$SO_2$ (regime III). The pattern of regime I is similar to that

in P15 but in a much smaller parameter space. There is no chemical bifurcation or abrupt transition in regime I. In regime II $SO_2$ mixing ratio above the clouds remains low and constant as $H_2O$ at 58 km increases. In regime III, $H_2O$ above the clouds increases as $SO_2$ at 58 km increases, different from $H_2O$ behavior in regimes I or II. Across the regimes there is the non-monotonic variability of $H_2O$ with respect to $SO_2$ variations at 58 km. $H_2O$ and $SO_3$ variations above the clouds are anti-symmetric for all three regimes due to sulfuric acid formation.

The $SO_3$-involved chemistry network connects $SO_2$ mixing ratio above the clouds to $H_2O$ at 58 km. The non-monotonic behavior of $H_2O$ above the clouds results from the interplay among eddy diffusion, neutral chemistry and photolysis processes. In those processes, the $SO_2$ self-shielding effect plays a crucial role.

We explored the mechanisms underlying the variations and anti-correlation between $SO_2$ and $H_2O$ at 64 km from TEXES. We tested two possibilities: eddy mixing change in the middle atmosphere and species variations at the middle cloud top. Both possibilities can originate from lower atmospheric processes. We found that the eddy mixing change alone cannot produce the observed variation range of $H_2O$ or the anti-correlation, while variations of mixing ratios at the middle cloud top with the regime I sulfur chemistry can explain both variations and the long-term anti-correlation of $SO_2$ and $H_2O$. This suggests that the observed $SO_2$ and $H_2O$ variations are more likely due to perturbations on mixing ratios at the middle cloud top rather than changes in the vertical mixing alone.

Although our 1D model provided the first and simplest explanation of the observed anti-correlation behavior of $SO_2$ and $H_2O$, our model is relatively simple with some caveats and could be improved in the future. First, our model does not include phase changes of $H_2O$ and $H_2SO_4$ that could affect trace species abundances in the middle atmosphere (e.g., Gao et al., 2014; Krasnopolsky, 2015). Second, our model does not include the coupling between the lower and middle atmosphere (e.g., Bierson & Zhang, 2020), which can directly link the lower atmospheric processes to the middle atmosphere. Third, our model does not include the local time and spatial variability across latitude and longitude (e.g., Marcq et al., 2019a). It would be important to revisit our proposed mechanism in a more realistic model in the future.

We also noticed discrepancies between different methods and observations of $SO_2$ and $H_2O$ in the middle atmosphere. Several methods have been used to infer the water vapor abundance in the mesosphere of Venus. From Venera 15 data at 30 $\mu m$, Ignatiev et al. (1999) derived a $H_2O$ volume mixing ratio of $10 \pm 2.5$ ppm at $62.5 \pm 1.3$ km for latitudes below $50°$. Using ground-based spectroscopy at 3.3 $\mu m$, Krasnopolsky et al. (2013) inferred a $H_2O$ mixing ratio of $3.2 \pm 0.4$ ppm at 74 km for latitudes below 55°. Using VIRTIS abroad Venus Express at 2.6 $\mu m$, Cottini et al. (2015) derived $3 \pm 1$ ppm for $H_2O$ at $69 \pm 1$ km; Fedorova et al. (2016), using SPICAV at 1.38 $\mu m$, inferred $H_2O$ = 6 ppm at 62 km; in both cases, low and middle latitudes were observed, and no evidence was found for local time or inter-annual variations. These results are all globally higher than the values inferred by TEXES. A possible reason is the choice of the D/H ratio in the Venus atmosphere. For the

TEXES observations, the D/H ratio is taken equal to 200 times the VSMOW (Vienna Standard Ocean Water), following Krasnopolsky (2010), but there is some uncertainty about this parameter. Another reason might be the use of different line transitions and some uncertainty in the line parameters. Finally, in the case of TEXES, the altitude of the penetration level is not precisely defined, since the spectroscopic analysis gives information on the pressure above the continuum level and not the altitude. Nevertheless, it can be seen that all observers agree on the absence of strong local and temporal variations of $H_2O$ at the cloud top of Venus. Indeed, between 2012 and 2016, the $H_2O$ volume mixing ratio inferred by TEXES was more or less constant (Encrenaz et al., 2016), as pointed out by the other teams for the same period.

The main advantage of the method used with TEXES is the fact that both the $SO_2$ and $H_2O$ volume mixing ratios are inferred simultaneously in location and time, at the same penetration level, from the same spectra and the same maps. Thus, the study of their local and temporal variations should not be significantly affected by uncertainty regarding the exact altitude of the penetration level. To our knowledge, TEXES is the only facility that offers this opportunity.

The continued observations of Venus using the TEXES/IRTF instrument will provide us with more information about atmospheric dynamics and tracer transport on Venus. However, due to the limited information in the cloud region and the lower atmosphere, it is still unclear that how dynamics and chemistry in the lower atmosphere, inside the clouds and in the middle atmosphere are coupled and

interacted. Besides, the decadal variations of $SO_2$ at the cloud top are observed since 1980s (Esposito, 1984; Esposito et al., 1988; Na et al., 1990; Marcq et al., 2013, 2019b). The underlying mechanism is elusive although our work highlights the importance of the lower atmospheric processes. It would be crucial to continue simultaneously monitoring $SO_2$ and $H_2O$ (as well as other species) in the middle and lower atmosphere, through both ground-based instruments and future spacecraft missions, to provide more clues. A three-dimensional model describing the entire Venus atmosphere involving multiple processes is expected to provide more insights into these problems in the future.

# Chapter II. Local-time Dependence of Chemical Species in the Venusian Mesosphere

## 2.1 Motivation

The Venusian mesosphere (~70-100 km) is characterized by complex photochemistry (e.g., Yung & DeMore 1982; Mills 1998; Zhang et al. 2012; Krasnopolsky 2012). Species like $SO_2$ and CO — fundamental components of the photochemical network — have shown significant spatial and temporal variabilities. For example, Venus Express detected that the $SO_2$ mixing ratio at 70-80 km varies by orders of magnitude over time and space (Vandaele et al. 2017a, 2017b). Ground-based observations by TEXES/IRTF (Texas Echelon Cross Echelle Spectrograph/Infrared Telescope Facility) show that $SO_2$ around the cloud top exhibits plumes and patchy features over the Venus disk (Encrenaz et al. 2012, 2013, 2016, 2019, 2020). Venus Express also observed that CO has strong short-term variabilities up to one order of magnitude (Vandaele et al. 2016).

Some chemical species in the Venusian mesosphere show strong local-time variabilities. Encrenaz et al. (2020) extracted the local-time dependence of $SO_2$ at ~64 km from TEXES/IRTF and found that the $SO_2$ mixing ratio generally exhibits two local maxima around the morning and evening terminators, respectively. SPICAV (Spectroscopy for the investigation of the characteristics of the atmosphere of Venus) on board Venus Express also observed a similar $SO_2$ local-time pattern at the cloud top on the dayside (Vandaele et al. 2017b; Encrenaz et al. 2019; Marcq et al. 2020).

Sandor et al. (2010) used microwave spectra to obtain day-night differences of $SO_2$ and SO at 70-100 km. Despite the scarcity of the data, $SO_2$ appears more abundant at night than that during the day, while SO is likely to have a reversed day-night difference. Belyaev et al. (2017) observed that midnight $SO_2$ abundance appears 3-4 times higher than at the terminators around 95 km through SPICAV occultations. For CO, Clancy and Muhleman (1985) observed a day-night difference from microwave measurements. They found that the CO bulge (i.e., the local maximum of CO mixing ratio) shifts from midnight to the morning as altitude decreases from above ~95 km to 80-90 km. Clancy et al. (2003) showed similar CO patterns in subsequent microwave observations. Vandaele et al. (2016) summarized the CO data observed by SOIR (Solar Occultation in the InfraRed) on board Venus Express and found a statistical difference between the morning and evening terminators, and the difference also depends on altitude. Compared to $SO_2$ and CO, $H_2O$ seems to vary insignificantly with local time. Encrenaz et al. (2012, 2013, 2016, 2019, 2020) using TEXES observed that the $H_2O$ mixing ratio at ~64 km, obtained from the HDO spectra, distributes uniformly over the Venus disk. Chamberlain et al. (2020) showed that the $H_2O$ profiles above 80 km observed by SOIR do not exhibit dependence on terminators. Sandor and Clancy (2012, 2017) using JCMT (James Clerk Maxwell Telescope) observed that HCl mixing ratio above 85 km exhibts no evident day-night difference. Krasnopolsky (2010) using the CSHELL spectrograph at NASA IRTF observed that the morning OCS can be more abundant than the afternoon OCS.

The origin of these local-time variabilities has not been thoroughly investigated but likely relates to atmospheric chemistry and dynamics. In the Venusian mesosphere occurs intense photochemistry (e.g., Zhang et al. 2012), in which the dependence of solar irradiance on local time affects the local distribution of chemical species. On Venus, the cloud region (~47-70 km) is characterized by a retrograde superrotating zonal (RSZ) flow (e.g., Sánchez-Lavega et al. 2008; Lebonnois et al. 2010; Mendonça & Read 2016; Mendonça & Buchhave 2020). In the thermosphere (>110 km), strong evidence shows a sub-solar to anti-solar (SS-AS) circulation pattern (e.g., Bougher et al. 2006). The upper mesosphere (90-110 km) might be a region where SS-AS circulation is superimposed on the RSZ flow (e.g., Lellouch et al. 1994). Besides, thermal tides excited by the solar heating also strongly perturb the temperature and winds in the mesosphere (e.g., Taylor et al. 1980; Limaye 2007; Fukuya et al. 2021). These dynamical flow patterns transport chemical species and modulate their local-time variabilities.

A few theoretical studies have investigated the local-time variabilities of chemical species. Jessup et al. (2015) studied spatial variations of $SO_2$ and SO observed by HST/STIS (Hubble Space Telescope Imaging Spectrograph). They showed through one-dimensional (1D) photochemical models that solar zenith angle could significantly affect the $SO_2$ variability. Gilli et al. (2017) presented CO and O density profiles in the upper atmosphere at different local times using a three-dimensional (3D) general circulation model (GCM) coupling chemistry and dynamics (Stolzenbach et al. 2015; Stolzenbach 2016). Their results indicate the importance of

the SS-AS circulation on the CO and O distributions. Navarro et al. (2021) and Gilli et al. (2021) used an improved GCM to study CO's spatial variabilities in the upper atmosphere. Their simulated CO pattern shows a CO bulge shift toward the morning by 2-3 hours in the mesosphere, attributed to a weak westward retrograde wind. However, a dedicated study of the local-time variability of $SO_2$ is still lacking, and mechanisms controlling CO's local-time distributions need further investigation.

As a preliminary step towards fully understanding the spatial and temporal variabilities of chemical species in the Venusian atmosphere, in this study we investigate the local-time dependence of multiple chemical species including $SO_2$ and CO using a 3D dynamical model in combination with a 2D (longitude-pressure) chemical model with the state-of-the-art full photochemical network on Venus. Our simulated local-time distributions of species like $SO_2$, CO, and $H_2O$ show agreement with observations. We explore underlying mechanisms determining species' local-time distributions and find that the relative importance of dynamics and chemistry depends on altitude and species. Our study indicates that the local-time distributions of $SO_2$ and CO can constrain important dynamical patterns in the Venusian atmosphere.

## 2.2 Methodology

We use a 3D GCM in combination with a 2D chemical-transport model (CTM) to study the local-time variabilities of chemical species in the Venusian mesosphere. We adopt this combination method because fully coupling chemistry with dynamics in

the GCM or utilizing a 3D CTM with a full chemical network is computationally expensive. A 2D (longitude-pressure) chemical model is sufficient to study the chemical species' local-time variabilities that we focused on in this work. For example, combining a 3D GCM with a 2D CTM has been used to study chemical species in Earth's atmosphere (e.g., Smyshlyaev et al. 1998).

We adopt the OASIS GCM, a novel and flexible 3D planetary model (Mendonça & Buchhave 2020). OASIS is a dedicated model that incorporates multiple self-consistent modules. For our Venus dynamical simulations, we use the non-hydrostatic dynamical core coupled with physics modules that represent a basalt soil/surface, convective adjustments, and the radiative processes from the gas and clouds (a non-grey scheme with multiple-scattering). The simulated atmosphere extends from the surface to 100 km, with a horizontal resolution of 2 degrees and a vertical resolution of ~2 km. The model was integrated for 25000 Earth days (~214 Venus solar days; one Venus solar day is ~117 Earth days) with a time-step of 50 seconds. The model and bulk planet parameters (e.g., specific heat, gravity and mean radius) are the same as the ones used in Mendonça and Buchhave (2020, see their Table 2). One of the main weaknesses of current Venus GCMs is the poor representation of the circulation in the deep atmosphere, which is also poorly constrained by observational data (refer to Mendonça & Read 2016 for more details). To represent a deep circulation in our 3D simulations closer to the observations, we applied a Newtonian relaxation method to force the zonal winds in the deep atmosphere towards the observed values. The forcing acts only at 44 km altitude, which is below the cloud region and the region

explored in this study. The equilibrium winds were constructed assuming the atmosphere at 44 km rotating as a solid body with a maximum velocity of 50 m/s at the equator based on the estimated observed values from Kerzhanovich & Limaye (1985). For the Newtonian relaxation timescale, we have assumed a value of 2000 Earth days (~17 Venus solar days), which is close to the radiative timescale at 44 km (Pollack & Young 1975). At 44 km, the temperature difference between the day- and night-side of the planet is small (less than 10K) because the radiative timescale is much longer than the dynamical timescale. The value chosen for the relaxation timescale ensures a good model performance and low impact in the wave activity in the lower atmosphere. Our converged simulations were further integrated to 5000 Earth days (~43 Venus solar days) to produce the temperature and wind fields for the CTM input.

We do not directly couple the GCM and CTM in the sense that the simulated gas distributions in the CTM are not used as the GCM input. As described in Mendonca and Buchhave (2020), the 3D GCM itself only uses simple representations of the clouds and chemistry. The cloud structure remains constant with time, and three different cloud particle size modes (Knollenberg & Hunten 1980; Crisp 1986) are used. The GCM considers four main chemical species in the atmosphere: 96.5% of $CO_2$ in mole, ~3.5% of $N_2$, 50 ppm of $H_2O$, and 100 ppm of $SO_2$. Their volume mixing ratios are assumed to be well-mixed in the GCM and not meant to be exactly equal to the values observed but to capture the main bulk conditions of the Venusian atmosphere.

The 2D CTM is generalized from the 1D state-of-the-art Caltech/JPL kinetics model (Yung & DeMore 1982; Mills 1998; Mills & Allen 2007; Zhang et al. 2010, 2012; Bierson & Zhang 2020; Shao et al. 2020). This model resolves complex chemistry for carbon, oxygen, hydrogen, nitrogen, sulfur, and chlorine species. This model includes 52 chemical species and over 400 reactions (refer to Zhang et al. 2012). We generalized this 1D model to 2D and included the advection for each chemical tracer in the longitude-(log-)pressure coordinate plane. See Appendix C for the derivation of the meridionally-mean continuity equation. The meridionally-mean advection is constructed from the output of the 3D GCM. We implemented the flux-limiting Prather scheme (Prather 1986; Shia et al. 1989, 1990) to calculate the advection of species in the 2D continuity equation. This scheme has several advantages, including the conservation of chemical species, maintenance of positive concentration, and stability for large time steps. The chemical model incorporating this scheme has been applied to the Earth's atmosphere to study variabilities of chemical species like ozone (Jiang et al. 2004). We have also implemented a parallel computing technique using Message Passing Interface (MPI) in our 2D CTM to improve simulation efficiency.

In our 2D CTM, photon density reaching the top of atmosphere (TOA) is set as equal to $\pi/4$ times the equatorial value on Venus, so as to represent the meridionally-mean value considering the latitudinal dependence of solar zenith angle. The solar zenith angle in our 2D CTM varies with longitude, and the solar zenith angle at each longitude also changes with time. Our 2D CTM has a vertical resolution of ~2 km and

a horizontal resolution of 12 degrees. The altitude range is ~58-100 km. The time step is set as 10 minutes. In Section 2.4, we show that increasing horizontal resolution does not change the simulated local-time variabilities of chemical species.

The 3D distributions of temperature and wind patterns from GCM simulations in the last ~4 Venus solar days are first averaged meridionally. To match the spatial and temporal grids in our 2D CTM, we then smooth and interpolate the GCM data to obtain temperature and wind fields in one-hour resolution. Finally, we average the fields temporally to obtain the diurnally-varying one-Venus-day (~117 Earth days) fields and repeatedly input them into the 2D CTM. Table 2.1 lists boundary conditions for several important species. For other species, zero flux at the upper boundary and maximum deposition velocity at the lower boundary (58 km) are applied. We apply the same lower and upper boundary conditions to all longitudes. The unknown sulfur reservoir in the upper atmosphere (e.g., Zhang et al. 2010, 2012; Vandaele et al. 2017a) is represented by a downward $S_8$ flux at the upper boundary in our model, as used in Bierson and Zhang (2020). The specified flux at the upper boundary (e.g., Table 2.1) is separate from the advective flux and is used to provide extra sources outside the domain (e.g., the $S_8$ flux). We calculate the advective flux above (below) the upper (lower) boundary by setting a ghost box with species' mixing ratios the same as those at the boundary. In the zonal direction, a periodic boundary condition (i.e., species abundances at 0 and 360 degrees are equal) is adopted.

**Table 2. 1** Boundary conditions for several important species in the 2D CTM.

| Species | Lower Boundary Condition | Upper Boundary Condition |
|---|---|---|
| $SO_2$ | $f = 1.0\ ppm$ | $\phi = 0$ |
| $H_2O$ | $f = 1.0\ ppm$ | $\phi = 0$ |
| CO | $f = 45\ ppm$ | $\phi = 0$ |
| NO | $f = 5.5\ ppb$ | $\phi = 0$ |
| HCl | $f = 0.4\ ppm$ | $\phi = 0$ |
| $CO_2$ | $f = 0.965$ | $\phi = 0$ |
| OCS | $f = 1.0\ ppm$ | $\phi = 0$ |
| $S_8$ | $v = v_m$ | $\phi = -6.0 \times 10^7\ cm^{-2}\ s^{-1}$ |

Note: $f$ means the fixed volume mixing ratio, $\phi$ means the diffusive boundary flux, and $v$ is the deposition velocity. Values here are referred to those in Zhang et al. (2012) and Bierson and Zhang (2020). Species not specified here all have $\phi = 0$ at the upper boundary and the maximum deposition velocity $v_m$ (see Zhang et al. 2012) at the lower boundary (58 km).

In this study, we treat the sub-grid diffusivity parameters $K_{xx}$, $K_{xz}$, $K_{zx}$, and $K_{zz}$ in the meridionally-mean continuity equation (see Appendix C) as free parameters. For simplicity, we assume zero $K_{xz}$ and $K_{zx}$. The meridionally-mean zonal wind is usually larger than the eddy wind. For example, the meridionally-mean zonal wind is ~100 m/s at ~60 km, while the eddy wind is ~10-20 m/s at ~60 km at the equatorial region in the GCM output. If we assume the sub-grid eddy length scale is 10-100 km (the horizontal grid size is about 200 km around the equator in the GCM), the horizontal diffusivity $K_{xx}$ is about $10^9 - 10^{10}\ cm^2 s^{-1}$. Here we use $K_{xx} = 10^9\ cm^2 s^{-1}$ to represent the horizontal transport by eddies. The $K_{zz}$ vertical profile in our CTM is the same as the 1D $K_{zz}$ profile in Zhang et al. (2012) and is applied to all longitudes. In Section 2.4, we will explore the sensitivity of our results to these parameters.

## 2.3 Local-time Dependence of Chemical Species

In this section, we discuss the local-time dependence of $SO_2$, CO, $H_2O$, HCl, ClO, OCS and SO. These chemical species' distributions are averaged over the last 5 Venus solar days from our simulations. To better understand the interaction between atmospheric dynamics and chemistry and the influence on local-time variability, we also estimate the chemical loss timescale $t_{Chemical}$ and horizontal transport timescale $t_{Transport}$. The chemical loss timescale for each species is equal to the number density of the species divided by its total chemical loss rate. For $SO_2$, CO and SO, the chemical loss in the fast cycles (see Appendix D) is excluded. The horizontal transport timescale is estimated using the planetary radius divided by the zonal wind speed (e.g., Zhang & Showman 2018).

The 3D GCM results show that the diurnal cycle excites various harmonics of the thermal tides in the Venus atmosphere (Fig. 2.1a-b). The thermal tides are stationary with respect to the sub-solar point. Observational (e.g., Pechmann & Ingersoll 1984; Zasova et al. 2007) and theoretical (e.g., Lebonnois et al. 2010; Mendonça & Read 2016) studies suggest that the semidiurnal component has the largest amplitude of the thermal tide harmonics in the upper cloud region. Our GCM successfully simulates this semidiurnal component in the upper cloud (58-70 km). In the vertical wind pattern shown in Fig. 2.1b, the semidiurnal tide at 58-70 km induces an upwelling branch in the afternoon. A similar branch also appears at 0:00-6:00 but with a weaker amplitude. At 18:00-0:00 and 6:00-12:00, the semidiurnal tide in the upper cloud

induces downwelling motions. The evening downwelling is stronger than the morning downwelling. Positive temperature anomalies are found around midnight and noon as a result of perturbations by the semidiurnal tide.

Above 85 km, the diurnal thermal tide dominates the wind and temperature local variations in our simulations (Fig. 2.1a-b). As altitude increases, the phase of the semidiurnal tide shifts eastward. Above 85 km, two upwelling branches of the semidiurnal tide merge into a dayside upwelling branch, while the morning downwelling of the semidiurnal tide extends and becomes the nightside downwelling branch above 85 km. In this altitude region, the vertical wind field is mainly composed of the wavenumber-one diurnal component. Temperature distribution is also affected by the diurnal thermal tide above 85 km, with positive anomaly on the dayside. At 85-100 km, the SS-AS circulation is imposed on the RSZ flows, marking a transition region from RSZ flow to SS-AS circulation where the wind pattern is important for chemical tracer exchange between the lower and higher altitudes as well as that between the dayside and the nightside. The chemical tracers at the lower altitude are first transported upward by the upwelling branch on the dayside and then delivered to the nightside by horizontal day-night flows of the SS-AS circulation. On

the nightside, the chemicals are recycled back to the lower region by the downwelling branch of the SS-AS circulation and transported to the dayside by the RSZ flows.

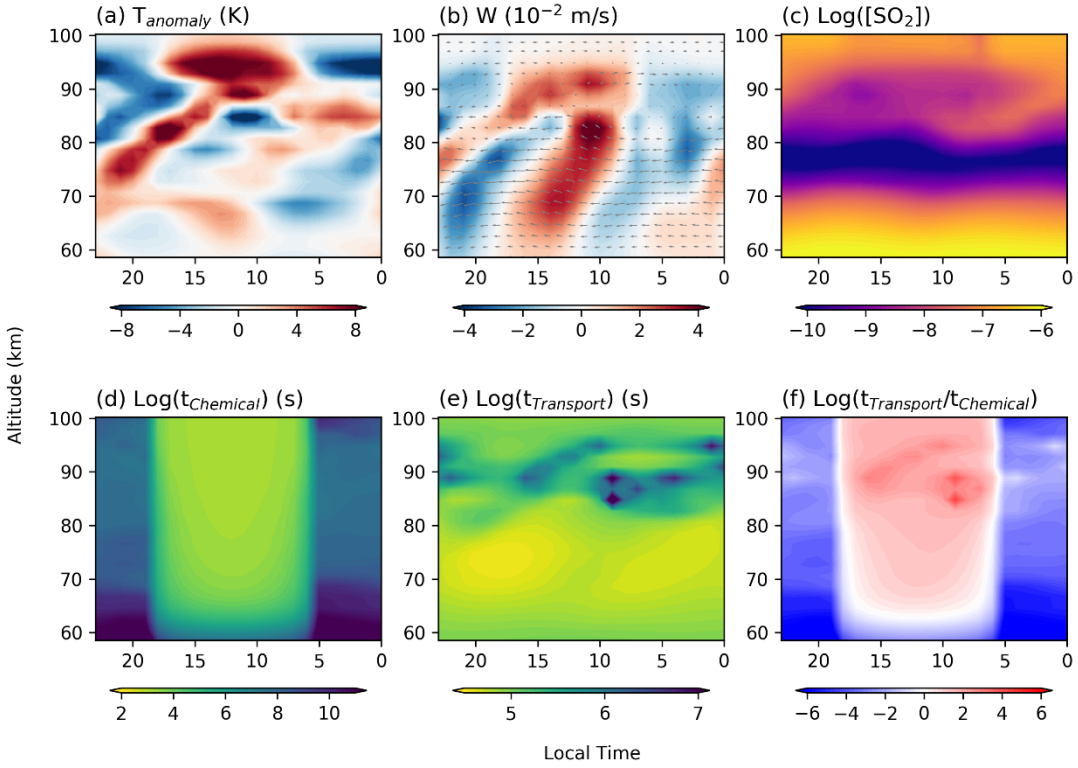


**Fig. 2. 1** Local-time dependence of (a) temperature anomalies $T_{anomaly}$, (b) vertical velocity W, (c) $SO_2$ mixing ratio, (d) $SO_2$ chemical loss timescale $t_{Chemical}$, (e) transport timescale $t_{Transport}$, and (f) ratio of $t_{Transport}$ to $t_{Chemical}$. The wind field (m/s) is superposed on panel b. Temperature and wind fields are from the OASIS simulations (Mendonça & Buchhave 2020), and the $SO_2$ mixing ratios is from the 2D CTM. Temperature anomaly is the deviation from an average temperature profile shown in Fig. S2.1. Note that both the 2D CTM and OASIS use (log-)pressure coordinate. Height at the vertical axis in this plot represents the isobaric level and is derived from pressure by using the VIRA model (cf. Table 1 of Mendonça & Read 2016). The local time 06:00 is the morning terminator, 18:00 the evening terminator, 12:00 the noon, and 00:00 the midnight. Earlier local time means eastward shift on Venus. The ratio of $t_{Transport}$ to $t_{Chemical}$ indicates the main driven mechanism for the species distribution: the ratio smaller than unity (blue region in panel f) implies a mainly transport-driven regime; the ratio larger than unity (red region in panel f) implies a mainly photochemistry-driven regime; the ratio around unity (white region in panel f) implies the transition between the two regimes.

### 2.3.1 $SO_2$

Our simulation shows that the semidiurnal thermal tide is essential to explain the $SO_2$ local-time pattern in the upper cloud region (Fig. 2.1). Below 80 km, the $SO_2$ mixing ratio decreases as altitude increases. Vertical mixing occurs when the $SO_2$-rich air is transported upward from a lower altitude, and the $SO_2$-poor air is transported downward from a higher altitude. In the upper cloud region (58-70 km), the two upwelling branches of the semidiurnal tide produce two local maxima in the $SO_2$ local-time distribution. The two maxima are shifted westward by the RSZ flow and located around two terminators. This local-time pattern is more clearly seen in Fig. 2.2. Our simulations successfully reproduce the $SO_2$ observations by TEXES at ~64 km (Encrenaz et al. 2020). Note that SPICAV also observed a similar $SO_2$ local-time distribution at ~70 km on the dayside (Vandaele et al. 2017b; Encrenaz et al. 2019; Marcq et al. 2020). The TEXES data exhibit more complicated features, like a peak around 22 hour and another around 2 hour (Fig. 2.2). The causes of these peaks are not well understood and might be associated with small-scale dynamics.

In the region above the clouds, photochemistry drives the $SO_2$ behavior on the dayside (Fig. 2.1f). Above 85 km, $SO_2$ day-night difference becomes evident; $SO_2$ is less abundant on the dayside than on the nightside. Both photochemistry and dynamics drive this day-night difference. On the dayside, photolysis destroys $SO_2$; on the nightside, the descending branch of the SS-AS circulation brings $SO_2$-rich air downward because $SO_2$ mixing ratio generally increases as altitude increases above

85 km due to the assumed $S_8$ downward flux in our model. Sandor et al. (2010) implied an $SO_2$ day-night difference from microwave measurements at 70-100 km, despite the scarcity of their data. Belyaev et al. (2017) observed 150-200 ppb $SO_2$ at midnight versus 50 ppb $SO_2$ at terminators around 95 km from SPICAV occultations. Our simulations roughly agree with the observed $SO_2$ pattern around 95 km (Fig. 2.10a).

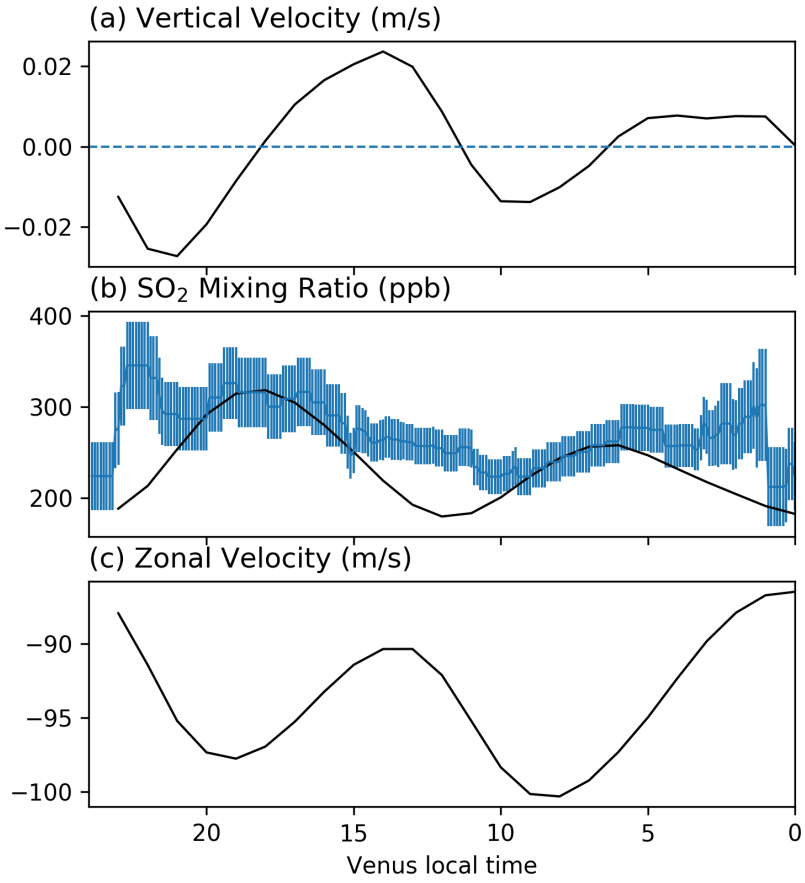


**Fig. 2. 2** Local-time distributions of (a) vertical velocity, (b) $SO_2$ mixing ratio, and (c) zonal velocity around 64 km. Observational data (error bars) in (b) are from TEXES/IRTF (Encrenaz et al. 2020). Positive vertical velocity is upward, and negative zonal velocity is westward.

### 2.3.2 CO

CO is a long-lived chemical species whose local-time distribution is determined mainly by dynamics (Fig. 2.3). Fig. 2.3b and c show that CO has a long chemical loss timescale above the clouds. Below 85 km, CO is well-mixed and almost exhibits no diurnal variations. Above 85 km, CO shows a day-night difference similar to $SO_2$ (Fig. 2.3a). This difference is caused by the SS-AS circulation. The CO mixing ratio generally increases as altitude increases above 85 km because it is mainly produced by $CO_2$ photolysis in the upper atmosphere and transported downward. Above 85 km, the SS-AS circulation reduces CO on the dayside by mixing the CO-poor air upward from below. Although photochemistry produces more CO on the dayside, the SS-AS circulation regulates and dominates the CO local-time distribution by transporting the CO from dayside to the nightside. As a result, CO is accumulated on the nightside and appears more abundant than the dayside.

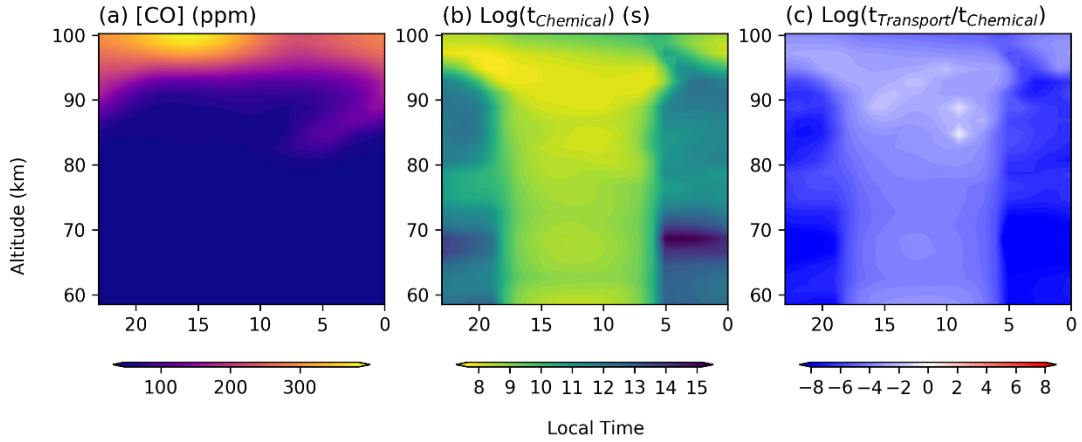


**Fig. 2. 3** Local time dependence of (a) CO mixing ratio, (b) CO chemical loss timescale $t_{Chemical}$ and (c) ratio of $t_{Transport}$ to $t_{Chemical}$.

The CO maximum is located around midnight at ~95 km and shifts to dawn at ~85 km (also see Fig. S2.3c-d). This pattern has been observed by microwave instruments (Clancy & Muhleman 1985; Clancy et al. 2003). The CO maximum is shifted westward due to zonal winds in the transition region, where SS-AS circulation transits to RSZ flow as altitude decreases. A similar CO pattern is also seen in the 3D GCM of Navarro et al. (2021) and Gilli et al. (2021). In their simulations, the CO maximum shifts westward toward the morning at 85-100 km, caused by a westward flow imposed on the SS-AS circulation. Our results overall agree with their results.

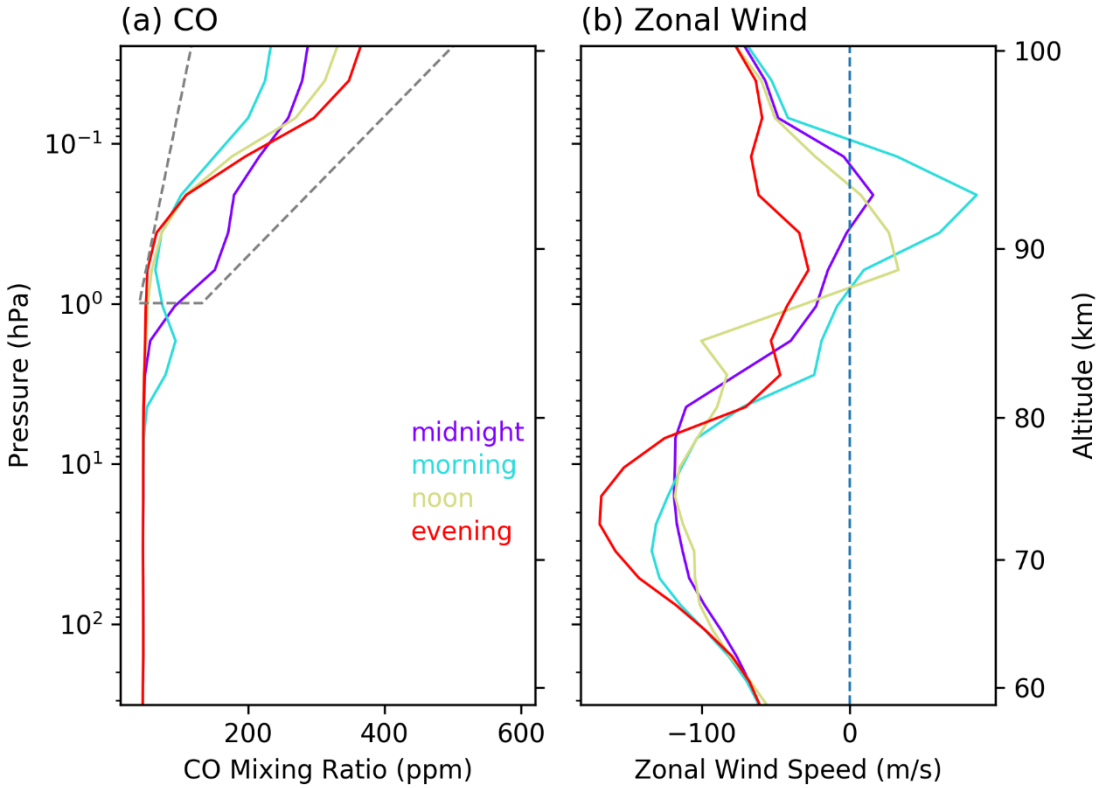


**Fig. 2. 4** Vertical profiles of (a) CO mixing ratio and (b) zonal wind at different local times. Altitude derived from the VIRA model is shown on the right axis. The grey dashed line in panel a encloses a region corresponding to a rough range of the observations by Vandaele et al. (2016). The blue dashed line in panel b is zero zonal wind.

SOIR has observed a statistical difference of the CO mixing ratio profiles between two terminators via solar occultation (Vandaele et al. 2016). In Fig. 6 of Vandaele et al. (2016), the CO mixing ratio below 95 km is larger at the morning terminator than the evening terminator, while CO above 105 km shows a reversed pattern. Our simulation reproduces such a pattern, but the reversal of the terminator difference occurs at a lower altitude (~90 km, see Fig. 2.4a) than in the SOIR observations (~90-110 km).

This reversed CO terminator difference originates from transition of atmospheric flows. At 80-90 km in our model, thermal tides transport CO-rich air downward on the nightside. The RSZ flows shift the CO-rich air toward the morning terminator. CO-poor air is pumped up by the upwelling branch of the tides on the dayside and is shifted toward the evening terminator. This process results in a larger CO mixing ratio in the morning than in the evening. Above 90 km, the SS-AS circulation transports CO produced on the dayside toward both terminators. Theoretically, if the dynamical pattern is symmetric about the noon, there should be no difference between the two terminators. However, the circulation from our 3D GCM simulations is asymmetric at these altitudes. For example, at 90-95 km, zonal flows at the two terminators have different amplitudes with opposite directions (Fig. 4b). This asymmetry could cause the terminator difference of the CO mixing ratio above 90 km. The wind pattern from the GCM in Gilli et al. (2021) is also asymmetric above 110 km due to perturbations of gravity waves. The CO observations by SOIR do not show a large difference between terminators until above 120 km (Vandaele et al.

2016). This may imply that only above 120 km, the asymmetric wind pattern becomes significant enough to affect CO local-time patterns.

The reversal altitude of the CO terminator difference might be closely related to the transition from RSZ flow to SS-AS circulation on Venus. That our simulated reversal level is lower than in the SOIR observations might imply that the transition from RSZ flow to SS-AS circulation occurs at a lower level in our GCM simulations than that in the real Venusian atmosphere. Because the transition level could also vary with time and space, future observations of CO distributions are useful to constrain the flow pattern transition in the upper atmosphere of Venus.

### 2.3.3 $H_2O$, HCl, ClO, OCS and SO

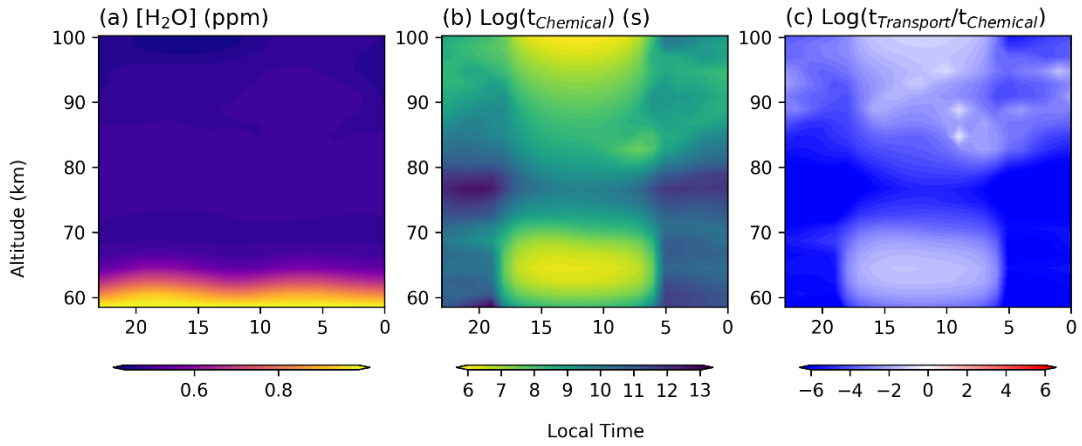


**Fig. 2. 5** Same as Fig. 2.3, but for $H_2O$.

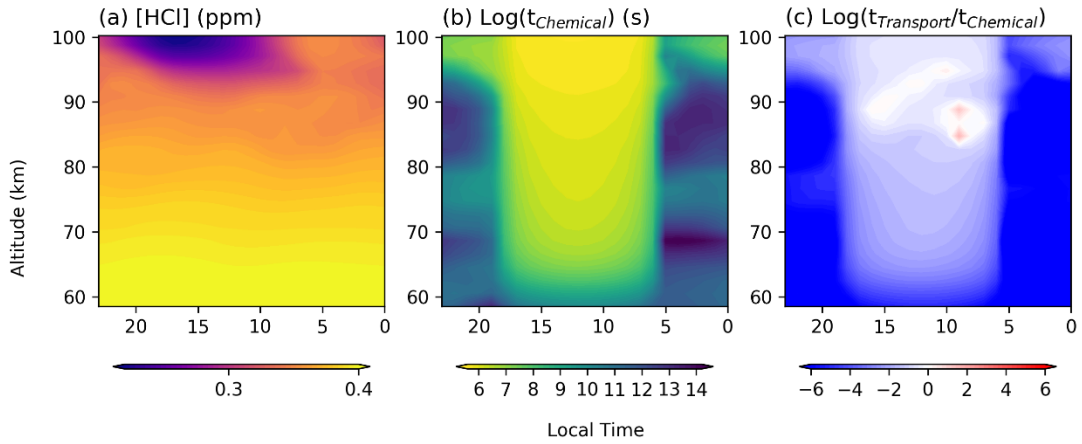


**Fig. 2. 6** Same as Fig. 2.3, but for HCl.

$H_2O$ distributes almost uniformly over local time and altitude in our simulations (Fig. 2.5a). This is because $H_2O$ is a long-lived species (Fig. 2.5b-c). Due to thermal tides, $H_2O$ exhibits small local-time variations in the upper cloud region (58-70 km), and the amplitudes of these variations are generally less than 30 percent. The uniform distribution of $H_2O$ over local time is consistent with observations by both SPICAV (e.g., Fedorova et al. 2008) and TEXES (e.g., Encrenaz et al. 2020). SOIR observations also show no significant difference of $H_2O$ between morning and evening terminators in the upper mesosphere (Chamberlain et al. 2020).

HCl, like $H_2O$, has a long chemical lifetime and distributes uniformly over space (Fig. 2.6). Its vertical profile in our simulations, like in previous 1D models (e.g., Yung & Demore 1982), shows a weak decrease from the cloud top to above 90 km. This simulated profile disagrees with JCMT (James Clerk Maxwell Telescope) observations (Sandor and Clancy 2012, 2017), which show a large decrease as altitude increases. Our model seems to support the conclusion of Sandor and Clancy

(2017) that the large decrease of HCl mixing ratio observed by JCMT does not originate from the SS-AS circulation. However, note that SOIR observed that HCl mixing ratio increases as altitude increases (Mahieux et al. 2015), which disagrees with the JCMT observations and also our model (and previous models). The SOIR observation suggests a chlorine source at high altitude, but no chemical hypothesis could support this source. Future observations are needed to further investigate the discrepancy among models and observations.

ClO is a short-lived species except at 80-95 km on the nightside (Fig. 2.7). In the entire mesosphere, ClO mixing ratio is rather small, mostly < 1 ppb. But at 80-95 km on the nightside, where ClO chemical lifetime is longer, ClO can reach a few tens of ppb (Fig. S2.6). Our simulated nightside ClO is roughly consistent with the results in a 1D nightside model from Krasnopolky (2013) but the abundance is much larger than the 1D diurnal-mean photochemical model results from Zhang et al. (2012) and Krasnopolsky (2012). Sandor and Clancy (2018) observed the nighttime ClO using JCMT and retrieved a few ppb of ClO above 85 km, which is an order of magnitude smaller than our simulated ClO mixing ratio on the nightside. Because the observed

HCl from JCMT is also smaller than our simulated HCl in the upper atmosphere, we hypothesize there might be some unidentified sinks for ClO and HCl.

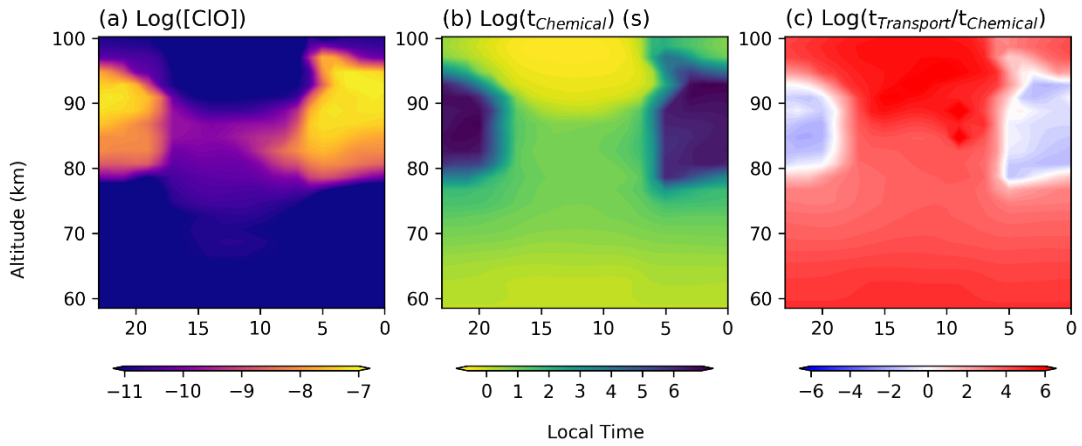


**Fig. 2. 7** Same as Fig. 2.3, but for ClO.

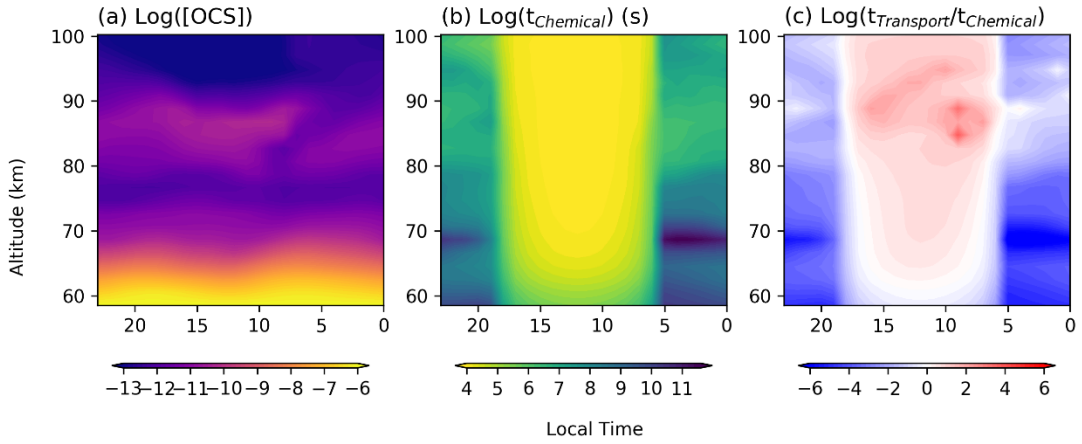


**Fig. 2. 8** Same as Fig. 2.3, but for OCS.

The vertical profile of OCS mixing ratio shows a small peak at 80-90 km. This peak is due to the downward $S_8$ flux from the top boundary in order to explain the $SO_2$ inversion. Part of the $S_8$ also converts to OCS to form a peak at 80-90 km. OCS is a short-lived chemical species on the dayside above the clouds and long-lived

species on the nightside (Fig. 2.8). Its distribution thus is largely affected by photochemistry on the dayside in the upper atmosphere and by dynamics on the nightside. OCS around 95 km exhibits a smaller mixing ratio on the dayside than the nightside and a reversed local-time pattern around 85 km (Fig. S2.7), as a result of competition between photochemistry and dynamics. However, since OCS mixing ratios at these altitudes do not exceed 1 ppb, these local time variations are not easily observed. At ~65 km in the upper cloud, OCS mixing ratio can exceed 1 ppb, and the local time difference of the OCS mixing ratio can reach ~10 ppb. This may be an observable pattern in the future. OCS also exhibits a two-maxima local time pattern at ~65 km, similar to $SO_2$. But the larger maximum of OCS locates around the morning terminator while that of SO2 is around the evening terminator. Krasnopolsky (2010) observed a few ppb of OCS near 65 km using the CSHELL spectrograph at NASA IRTF, and indicated a pattern in which the morning OCS is more abundant than the afternoon OCS, supporting our simulated OCS local-time pattern here (Fig. 2.10c). The OCS decrease from morning to afternoon should be related to that around 65 km, the OCS behavior is both driven by photochemistry and dynamics (Fig. 2.8c), unlike $SO_2$, which is more driven by dynamics.

SO exhibits a complex spatial pattern (Fig. 2.9). Since SO is a short-lived species and mainly produced by $SO_2$ photolysis, SO is more abundant on the dayside than the nightside. But in the upper cloud region on the nightside, SO has a longer chemical lifetime than the transport timescale by the RSZ flow (Fig. 2.9c), leading to a smaller day-night contrast than that at 70-95 km. The day-night difference of SO in the upper

mesosphere is consistent with the JCMT observation by Sandor et al. (2010) (Fig. 2.10b). However, the SO mixing ratio around 95 km is lower in our model than the SPICAV observations (Belyaev et al. 2012). The SO mixing ratio shows a very strong local-time dependence (Fig. 2.9a). Therefore, only observing the terminator SO is insufficient to understand the SO behavior. To better understand the sulfur cycle in the upper mesosphere of Venus, observations covering multiple local times on both dayside and nightside are required.

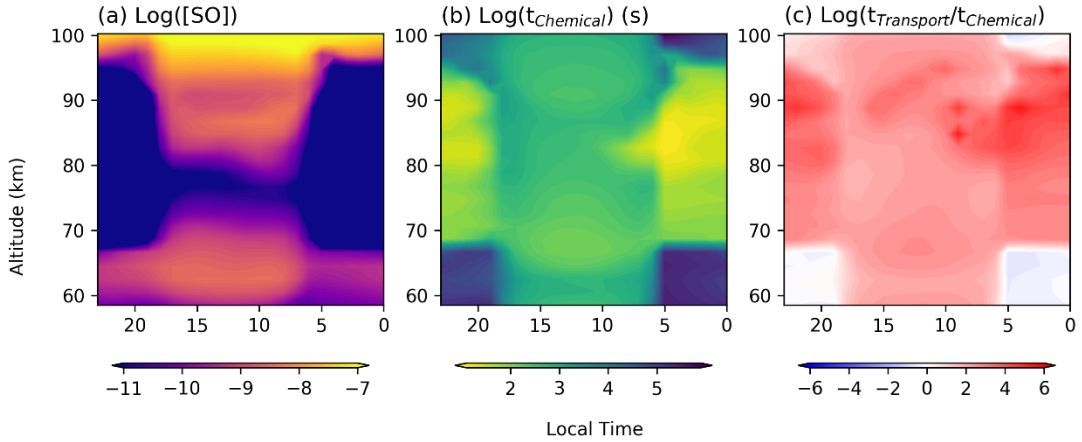


**Fig. 2. 9** Same as Fig. 2.3, but for SO.

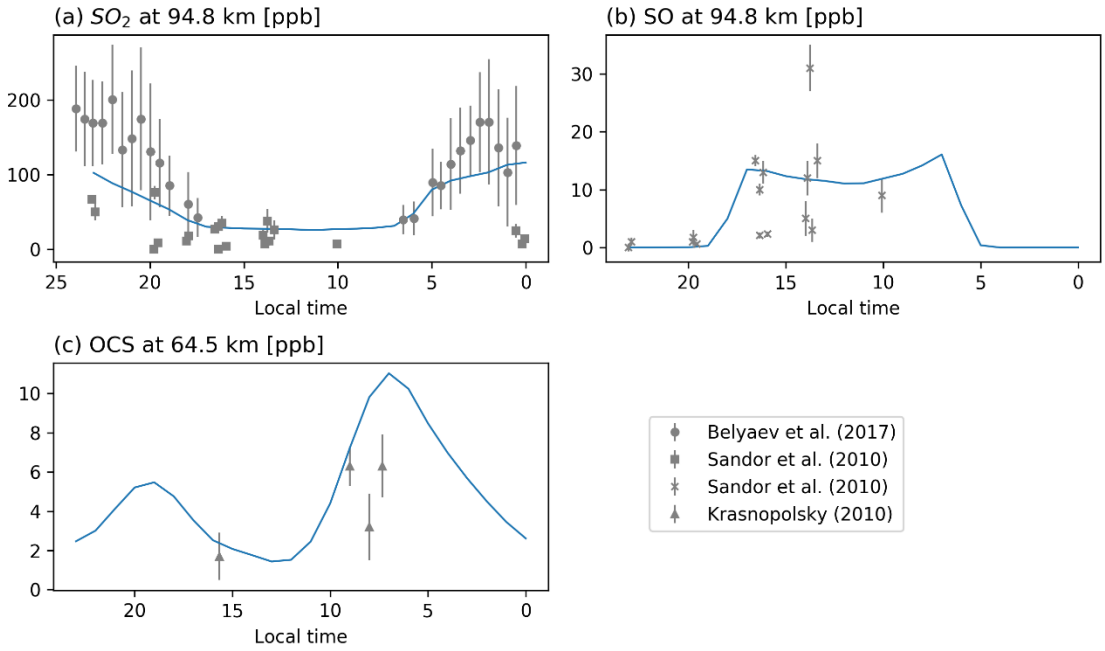


**Fig. 2. 10** Local time variations of volume mixing ratios of $SO_2$, SO and OCS from both our model and observations (Fig. 11b of Belyaev et al. 2017; Sandor et al. 2010; Krasnopolsky 2010). Note that the observation altitude is not necessarily exactly the value shown in this plot (refer to Table 2.2 to see the observation altitude range).

**Table 2. 2** Observations used in this paper.

| Observation | Altitude, km | Species | Mixing ratio range | Reference |
|---|---|---|---|---|
| TEXES | ~64 km | $SO_2$ | 150-400 ppb | Encrenaz et al. (2020) |
| JCMT | 70-100 km | | 0-90 ppb | Sandor et al. (2010) |
| SPICAV | 95-100 km | | 50-200 ppb | Belyaev et al. (2017) |
| Microwave | 80-100 km | CO | 30-1000 ppm | Clancy and Muhleman (1985) |
| JCMT | 75-100 km | | 50-1000 ppm | Clancy et al. (2003) |
| SOIR | 85-130 km | | $10^{-4}$-$10^{-1}$ | Vandaele et al. (2016) |
| TEXES | ~64 km | $H_2O$ | ~1 ppm | Encrenaz et al. (2020) |
| JCMT | 70-100 km | HCl | 0-450 ppb | Sandor and Clancy (2012,2017) |
| SOIR | 70-105 km | | 30-800 ppb | Mahieux et al. (2015) |

| | | | | |
|---|---|---|---|---|
| JCMT | 70-100 km | ClO | 1.5-3.7 ppb | Sandor and Clancy (2018) |
| CSHELL | ~65 km | OCS | 0.3-9 ppb | Krasnopolsky (2010) |
| JCMT | 70-100 km | SO | 0-30 ppb | Sandor et al. (2010) |
| SPICAV | 85-105 km | | 10-1000 ppb | Belyaev et al. (2012) |

**2.4 Sensitivity Test**

We conduct sensitivity tests to explore the effects of the horizontal diffusion coefficient $K_{xx}$, the vertical diffusion coefficient $K_{zz}$, and the horizontal resolution on our results. For simplicity, we still assume the diffusion coefficients $K_{xz}$ and $K_{zx}$ as zero.

Our sensitivity tests show that $K_{zz}$ augment does not affect the overall local-time patterns of all species discussed above (Fig. S2.2-2.8). For example, the two-maximum pattern of $SO_2$ at ~64 km is still well produced in the cases with a larger $K_{zz}$ (Fig. S2.2a). The major effect of increasing $K_{zz}$ is to increase the $SO_2$ mixing ratio below 80 km. The increase below 80 km is due to more diffusion from the lower sulfur reservoir (at ~58 km in our model). As a result, the mixing ratio of SO—a photochemical product of $SO_2$—below 80 km also increases. OCS is also sensitive to $K_{zz}$ value. As $K_{zz}$ increases, the amplitude of the OCS local-time variation at ~65 km increases despite the qualitative pattern unchanged (Fig. S2.7a). This implies that the OCS local-time pattern at ~65 km can be a good indicator of the strength of atmospheric vertical mixing.

Changing $K_{xx}$ from $10^9\ cm^2 s^{-1}$ (the value in the nominal case) by a factor of 10 does not affect the local-time patterns of all species discussed above (Fig. S2.2-2.8). It exerts almost no effect on the mixing ratios of the species. This is because horizontal transport by eddies only contributes a small proportion to chemical transport compared to the meridionally-mean zonal wind; the horizontal diffusion timescale is ~$10^7$-$10^9$ s (estimated by $L^2/K_{xx}$, where $L$ is planetary radius) compared to the advection timescale of ~$10^4$ s in the upper cloud (Fig. 2.1e). Our test also shows that increasing the horizontal resolution from 12 degrees to 6 degrees does not change the local-time patterns of the species discussed in this work (Fig. S2.2-2.8).

**2.5 Conclusion and Discussions**

In this paper, we investigated the local-time dependence of chemical species in the Venusian mesosphere. We used a 3D GCM and a 2D CTM to simulate species' local-time distributions and investigate the underlying mechanisms. Our models reproduce the observed local-time patterns of many chemical species such as $SO_2$ and CO. Dynamics and photochemistry play different roles in controlling the local-time patterns for different chemical species in the Venusian atmosphere.

As observed by TEXES, the local-time pattern of the $SO_2$ at ~64 km features two local maxima around terminators (Encrenaz et al. 2020). Using our model, we found that this feature is caused by the superposition of the semidiurnal thermal tide and the RSZ flow in the upper cloud. The two upwelling branches of the semidiurnal tide produce two local $SO_2$ maxima, and the superrotating wind advects the maxima

toward terminators. $SO_2$ above 85 km has a large day-night difference with more $SO_2$ on the nightside, due to both chemistry and dynamics; $SO_2$ on the dayside is destroyed by photolysis, while $SO_2$ on the nightside is enriched by downwelling motions. This day-night difference of $SO_2$ in our model agrees with SPICAV occultation observations.

Circulation patterns control the CO local-time pattern over photochemical processes in the upper mesosphere. Above 80 km, CO increases as altitude increases. The upwelling of SS-AS circulation transports the CO-poor air on the dayside, while the downwelling does the opposite on the nightside. This circulation pattern decreases CO on the dayside and increases CO on the nightside. The CO local-time maximum shifts westward from midnight to the morning as altitude decreases in the upper mesosphere. This shift is consistent with microwave observations and is due to the transition from the SS-AS circulation to the RSZ flow. Below 80 km, the CO mixing ratio is nearly constant over space due to its long chemical loss timescale.

Our models also explain the CO terminator difference observed by SOIR. CO at the morning terminator is more abundant than that at the evening terminator at lower altitudes, while this pattern is reversed at higher altitudes. The difference at lower altitudes is due to thermal tides combined with the RSZ flows. The difference at higher altitudes might relate to the zonally asymmetric circulation. The reversal level simulated by our models is lower than the SOIR observations. This could indicate that the transition level from RSZ flow to SS-AS circulation in our GCM is lower than

that in the Venusian atmosphere. The CO local-time variability could thus be used to constrain the atmospheric circulation of Venus.

$H_2O$ and HCl are long-lived like CO and distribute almost uniformly over both local time and altitude. The uniform distribution of $H_2O$ is qualitatively consistent with the TEXES observations. HCl vertical profiles simulated by our models disagree with JCMT observations and support that SS-AS circulation is unlikely to produce the large decrease of HCl in the upper mesosphere. ClO shows a maximum at 80-95 km on the nightside. OCS is observable in the upper cloud and also exhibits a two-maxima local-time pattern in the upper cloud. SO is a short-lived species whose mixing ratio is larger on the dayside than the nightside.

The disagreement of RSZ-to-SS-AS transition level between the model and the SOIR data needs further investigation. This transition occurs where the semidiurnal tides dissipate in the upper mesosphere. The thermal tidal waves transport retrograde angular momentum downwards to the superrotation region and decelerate the atmosphere above (Mendonca & Read 2016). These waves dissipate/break in the upper layers by radiative damping. Improving the representation of gas absorbers in the upper atmospheric region of the 3D simulations and moving the top of the model domain to higher altitudes might help reduce the disagreement in the RSZ-to-SS-AS transition altitude between the data and the model. The latter will mitigate the inaccuracies due to the top rigid model boundary, which may impact the atmospheric flow in the transition region. Also, moving the top

boundary to a higher altitude will diminish the impact of the sponge layer scheme in the model's uppermost layers in the GCM.

Furthermore, in the future, new observations from the Venus missions (DAVINC+, VERITAS and EnVision) will reveal more spatial and temporal variabilities of chemical species on Venus. To understand these variabilities, the 3D GCM + 3D CTM approach could be a better way than our current approach despite a more expensive computational cost. A future 3D GCM + 3D CTM model set will show how 3D circulations (including meridional circulations) and photochemistry together control species' variabilities in the middle atmosphere of Venus.

# Chapter III. Evolution of the Ice Shell on Enceladus

## 3.1 Introduction

Enceladus is the third geologically active body whose internal heat can be detected by remote sensing (Spencer et al. 2006), following the Earth and Io. A high heat flow, ~5-15 GW, is observed by Cassini's Composite Infrared Spectrometer (CIRS) on the south polar terrain (SPT) of Enceladus (Spencer et al. 2006, 2013; Howett et al. 2011). Gravity, shape and libration data from Cassini demonstrate the existence of a global subsurface ocean (e.g., Iess et al. 2014; Beuthe et al. 2016; Thomas et al. 2016; Čadek et al. 2016). If the freezing point of the ocean is close to 273 K, the implied conductive heat flow is a few tens of GW at present (Hemingway et al. 2018). Thus, if Enceladus is now in steady state and the ocean is not freezing with time, a corresponding endogenic heat production must be taking place.

Because radiogenic heating at Enceladus is only ~0.3 GW (Roberts and Nimmo 2008), by far the most likely heat source is tidal dissipation. Until recently, it was unclear whether sufficient tidal heat was available. However, recent astrometric results (e.g., Lainey et al. 2020) have demonstrated that Saturn is transferring energy and momentum to its orbiting satellites at a much higher rate than previously thought (Meyer and Wisdom 2007). Thus, even with the current small eccentricity, tidal dissipation can be sufficient to maintain Enceladus in a conductively steady state (Fuller et al. 2016; Nimmo et al. 2018).

However, several puzzles remain. One is where in Enceladus the tidal heat is dissipated. Initial studies focused on the ice shell (e.g., Roberts and Nimmo 2008; Shoji et al. 2013; Běhounková et al. 2015), but more recent studies have found it difficult to generate enough heat in the ice shell (Souček et al. 2016; Beuthe 2019). Instead, water-filled fractures (Kite and Rubin 2016), the ocean beneath (Chen and Nimmo 2011; Tyler 2011; Wilson and Kerswell 2018; Rovira-Navarro et al. 2019, 2020), or the porous silicate core (Roberts 2015; Choblet et al. 2017; Liao et al. 2020) have been suggested as alternatives. A second is whether Enceladus is actually in steady state. In principle, tidal-orbital feedbacks can arise and generate time-variable heating rates and eccentricities (e.g., Ojakangas and Stevenson 1986). Furthermore, the presence of deformed terrains with indications of high heat flux elsewhere on Enceladus (Giese et al. 2008) suggests some kind of time-variable behaviour. We will examine both of these questions through the prism of ice shell librations.

In a reference frame fixed to the surface of Enceladus, librations result in a periodic motion of Saturn across the sky. Librations can be either physical - variations in the ice shell rotation rate, driven by time-variable torques from the primary – or optical – driven by the time-variable orbital speed of Enceladus in its eccentric orbit (Hurford et al. 2009). Either kind results in motion of the tidal bulge relative to the solid surface and can thus produce deformation and heating. In general, librations are forced at various distinct periods arising from the various orbital periodicities. However, Enceladus also has free libration periods, the natural frequencies of the system. In the case of an ice shell, the natural frequency depends on the ice shell

thickness. As with any oscillator, if the natural libration frequency is close to the forcing frequency, resonant amplification will occur.

An early suggestion that Enceladus's high heating rate was driven by a 3:1 libration resonance (Wisdom 2004) was not borne out by subsequent Cassini gravity measurements. Rambaux et al. (2011) investigated forced librations at Europa and argued that a similar resonance might occur, with the very interesting possibility of a thermal runaway. However, this paper did not include the effect of a shell of *finite* rigidity on the libration amplitude (cf. Van Hoolst et al. 2013). Luan and Goldreich (2017) proposed a thermal runaway for Enceladus. Eccentricity growth of Enceladus produces more tidal dissipation and melts the ice shell. The thinner ice shell in turn leads to enhancement of tidal dissipation. Runaway melting follows until the decrease of shell thickness leads to large eccentricity damping. One goal of our study is to investigate whether a libration-driven thermal runaway could take place at Enceladus or whether thermal equilibrium of the ice shell can be maintained against small perturbations.

Rambaux et al. (2010) investigated forced librations at Enceladus, but their results did not include the effect of a subsurface ocean. As shown by Van Hoolst et al. (2013), inclusion of an ocean overlain by an elastic shell can completely change the librational response of a body. Van Hoolst et al. (2016) included this effect in their study of Enceladus's librations but did not address the issue of heat generation. This is because the present-day libration amplitude is known (Thomas et al. 2016) and is too small to generate sufficient heat. However, since Enceladus's eccentricity and

libration amplitudes could have been higher in the past, we wish to investigate whether a thermal runaway could have operated recently, so that it is contributing to the present-day energy budget.

In this work we calculate the forced librations of Enceladus's ice shell using the model of Van Hoolst et al. (2013). We compare the resulting ice shell tidal dissipation rate to the present-day heat flow on Enceladus to understand the thermal state of Enceladus. We find, in common with other studies, that the ice shell heating is insufficient to compensate for the high conductive heat loss on Enceladus. We then investigate whether a thermal runaway of the kind proposed above could occur on Enceladus. We find that even with a higher eccentricity in the past, Enceladus could have been in a stable, high-heat-flux equilibrium resistant to small perturbations, and that no thermal runaway is likely.

### 3.2 Methodology

We follow the elastic libration model established by Van Hoolst et al. (2013, hereafter VB13) to calculate the forced libration amplitude. This model is developed for a tidally locked satellite with three homogeneous layers: an ice shell, a subsurface ocean and a rocky core. Compared to previous libration models assuming infinite rigidity of the ice shell (e.g., Van Hoolst et al. 2009; Rambaux et al. 2011), this model includes the effect of the finite elasticity of the shell.

In this libration model, the gravitational torques the satellite experiences can be divided into two major parts. One is the total torque applied by the external gravitational potential on both the periodic and static bulges

$$\Gamma_t = \frac{3}{2}\frac{k_f - k_2}{k_f}(B - A)\frac{GM_p}{d^3}\sin 2\psi\,, \qquad (3.1)$$

where $k_f$ and $k_2$ are the fluid Love number and classical dynamical Love number. $(B - A)$ is the equatorial moment-of-inertia difference. $G$ is the gravitational constant, $M_p$ is the mass of the primary, and $d$ is the distance between the satellite and the primary. $\psi$ is the angle between the long axis of the satellite and the direction to the primary. This external torque expression is from equation (12 or 30) in VB13 and is applicable for each internal layer of the satellite. To get an expression for a specific layer, Love numbers, moment-of-inertia difference and the angle $\psi$ need to be specified for that layer. Note that if the satellite has no rigidity, then $k_2 = k_f$ and the total torque is zero.

The other part is the torques between internal layers. The pressure torque from the subsurface ocean can be divided into two components which can be incorporated into the expressions of the external and internal gravitational torques. The combined effect of the external gravitational torque above and the contribution from the oceanic pressure torque is

$$\Gamma_{pe,i} = \frac{3}{2}\left[(B_i - A_i)\frac{k_f^i - k_2^i}{k_f^i} + (B_{ob} - A_{ob})\frac{k_f^{ob} - k_2^{ob}}{k_f^{ob}}\right]\frac{GM_p}{d^3}\sin 2\psi_i\,, \qquad (3.2)$$

for the rocky core. Subscript or superscript $i$ represents the core (or the rocky interior), and $ob$ refers to the bottom of the ocean. This expression is from equation (34) in VB13. A similar expression can be written for the ice shell layer, with subscript or superscript substituted.

The other component of the oceanic pressure torque goes into the expression of the internal gravitational torque. The final expression of the internal torque including the contribution from the pressure torque and associated with the static bulge is

$$\Gamma_{pg,i}^{static} = \frac{4\pi G}{5}\left[(B_i - A_i) + (B_{ob} - A_{ob})\right]\left[\rho_o\beta_o + \rho_s(\beta_s - \beta_o)\right]\sin 2(\gamma_s - \gamma_i)\,, \quad (3.3)$$

where subscript or superscript *o* and *s* represent the ocean layer and the shell layer, respectively. $\rho$ and $\beta$ are the density and the equatorial flattening ($\beta = (a-b)/a$, where a and b are the radii of the two equatorial principal axes of inertia). $\gamma$ is the small libration angle. This expression is from Eq. (37) in VB13. This expression is the internal torque exerted on the core, and the same torque with an opposite direction is exerted on the shell. The internal torque associated with the periodic bulge and including the contribution from the pressure torque is

$$\Gamma_{pg,i}^{per} = 2K_{im}L_{osc} + 2K_{ii}\gamma_i - 2K_{is}\gamma_s, \qquad (3.4)$$

for the core layer. Here the coefficients $K_{im}$, $K_{ii}$ and $K_{is}$ refer to equation (39-41) in VB13. $L_{osc}$ is the oscillation part of the true longitude at the diurnal frequency (refer to equation (11) in Rambaux et al. 2011). This expression is from equation (38) in VB13. A torque equal to (3.4) but with an opposite direction is exerted on the shell

layer. Note that here we only consider the internal torque related to the periodic tidal bulge at the diurnal frequency. The torque related to the periodic bulge at long-term frequency is not considered in this study.

The deformation of each layer also changes the polar moment of inertia. The change of the polar moment of inertia due to the variable centrifugal acceleration has negligible effect (Van Hoolst et al. 2008, 2013) and is thus not considered here. The change due to zonal tides at the diurnal frequency gives an additional forcing of a few percent (Van Hoolst et al. 2008, 2013) and is included in our calculations. Refer to equation (44) in VB13 for the expression of this effect. Here we ignore the effect on the polar moment of inertia from zonal tides at long-term periods.

The final equations to calculate the forced librations are

$$C_s\ddot{\gamma}_s + K_1\gamma_s + K_2\gamma_i = 2K_3L_{osc}, \qquad (3.5)$$

$$C_i\ddot{\gamma}_i + K_4\gamma_s + K_5\gamma_i = 2K_6L_{osc}, \qquad (3.6)$$

where $C$ is the polar moment of inertia. The expressions of the coefficients $K_1$ to $K_6$ refer to Equations (47-52) in VB13. To allow readers to verify our calculations, an example of this calculation is shown in Appendix G.

In the libration calculations, the dynamical Love number $k_2^j$ for each layer needs to be specified. This Love number can be acquired from the radial displacement:

$$k_2^j = \frac{4\pi G\rho_j}{5R^3}\left(R_j^4 y^j - R_{j-1}^4 y^{j-1}\right), \qquad (3.7)$$

where $R$ is the radius of the satellite. $R_j$ is the radius of the upper surface of layer $j$. $j-1$ refers to the layer below layer $j$. $y^j$ is the radial displacement at the upper surface of layer $j$. This expression is from equation (24) in VB13. Here we calculate the radial displacement using the viscoelastic model developed by Roberts and Nimmo (2008). The input of this model is the physical properties of each homogeneous layer, including rigidity and viscosity. In our work, to better represent the viscosity profile in the ice shell, we divide the shell region into multiple layers with different viscosity values. The details of this division are described in Appendix F.

The true-longitude oscillation ($L_{osc}$) is obtained from the JPL/Horizons database (https://ssd.jpl.nasa.gov/horizons.cgi). This database conveniently provides the time series of orbital osculating elements for different astronomical bodies. Here we obtain the time series of the orbital elements of Enceladus for 300 years (1850-2150) with a time interval of one hour. The reference frame is ICRF/J2000.0, and the center is Saturn. We detrend the calculated true-longitude data to get its oscillations. Then through Fourier decomposition, the orbital forcings at different frequencies are obtained (see Table 3.1). Finally, the libration amplitudes are calculated via (3.5-3.6), and the libration heating is calculated via (3.8) in Section 3.5.

### 3.3 Forcings in JPL/Horizons Data

**Table 3. 1** Fourier decomposition of true-longitude oscillations of Enceladus based on data from JPL/Horizons Ephemeris.

| Frequency (rad/day) | Period (days) | Magnitude (arc second) | Phase (degree) |
|---|---|---|---|
| 4.579656 | 1.371978 | 1671.31 | 111.64 |
| 0.001548 | 4058.259259 | 901.51 | 163.83 |
| 0.004415 | 1423.025974 | 623.74 | 46.61 |
| 4.578107 | 1.372442 | 36.39 | -112.19 |

Table 3.1 gives the main orbital perturbing terms of Enceladus, obtained from a frequency analysis of true-longitude oscillations via the fast Fourier transform (FFT) method. The first three forcing terms are the mean anomaly, the Dione-Enceladus resonance and the Dione proper pericenter, respectively (Rambaux et al. 2010). The fourth, small term is FFT spectral leakage from the mean anomaly.

Comparing this table to that in Rambaux et al. (2010), here we obtain a slightly smaller amplitude for the mean-anomaly forcing. This is due to spectral leakage of the FFT method. Reducing this leakage effect by using the Hann window is shown in Table S3.1. However, since this leakage does not significantly affect our results, we will still show the results without applying the Hann window in the following sections. The phases of the first three terms here are different from those in Rambaux et al. (2010) because of difference in selected datasets (e.g., different initial starting points of time series of orbital elements). This phase difference does not affect

accuracy of our calculations; in Fig. S3.1, we show that our dataset and method give results consistent with Fig. 2a in Rambaux et al. (2010) if the same interior model is used.

### 3.4 Interior Models and Librational Response

We first need to specify the interior structure of Enceladus to calculate forced librations from equations (3.5-3.6). We use a three-layer model here: core, ocean and shell. Based on Cassini's measurement of the mean moment of inertia (0.331±0.002), the core size of Enceladus is inferred as ~190 km (Hemingway et al. 2018), assuming Enceladus has fully differentiated. We adopt this core size as a constraint. For the ice shell thickness, various estimates give a range of results based on different methods (Iess et al. 2014; McKinnon 2015; Beuthe et al. 2016; Thomas et al. 2016; Čadek et al. 2016; Van Hoolst et al. 2016; Hemingway and Mittal 2019). Therefore, here we take the shell thickness as a free parameter, ranging from 5 to 50 km, and construct 41 interior models with different shell thicknesses.

Table 3.2 shows major physical properties of our interior models. Bulk modulus, shear modulus and viscosity are required to calculate the radial displacement (equation E7) in the tidal model of Roberts and Nimmo (2008). The bulk modulus (not shown in Table 3.2) is set as $10^{19}$ Pa for all layers (effectively incompressible). The shear modulus assumed for the core is $10^{10}$ Pa and for the ice shell is $3.3\times10^{9}$ Pa. The core viscosity is $10^{25}$ Pa s. Because the code of Roberts and Nimmo (2008) cannot treat a purely fluid layer, the ocean is represented as a layer with low viscosity

and rigidity. As long as this layer's Maxwell time is well away from the forcing period, this approximation works reasonably well. To better account for the viscosity effect of the ice shell, here we divide the shell into multiple sub-layers with viscosity changing by orders of magnitude. Details of this treatment are described in Appendix F.

**Table 3. 2** Physical properties of interior models of Enceladus

| | Core | Ocean | Shell |
|---|---|---|---|
| Density (kg/m$^3$) | Calculated[(a)] | 1000 | 900 |
| Radius of upper boundary (km) | 190 [(b)] | 202.3-247.3 | 252.3 |
| Shear modulus (Pa) | $10^{10}$ | $10^6$ | $3.3\times10^9$ |
| Viscosity (Pa s) | $10^{25}$ | $10^8$ | $10^{14}$ [(c)] |

[(a)] Core's density is calculated using the constraint of the total mass of Enceladus

[(b)] See Hemingway et al. (2018)

[(c)] This value is the basal viscosity of ice shell. Viscosity varies within ice shell; See Appendix A for details

In common with earlier works (e.g., Van Hoolst et al. 2016), our calculations show that the diurnal libration amplitude is greatly dependent on the shell thickness (Fig. 3.1a). The diurnal libration amplitude increases from a few hundred meters to a few kilometers as the shell thickness decreases from 50 km to 5 km. This is because one of the two free frequencies gets closer to the diurnal frequency as the shell becomes thinner, which amplifies the diurnal libration. On the contrary, the libration amplitudes at long periods, 1423 days and 4058 days, are almost constant for

different interior models. This is because when the interior structure changes, the free-libration periods change but are still around a few days. The long forcing periods are always far away from the free libration periods. This insensitivity has also been seen in the long-term librations of Europa (Rambaux et al. 2011).

Despite the insensitivity to the shell thickness, the long-term libration amplitudes are not negligible (~0.7 and ~1.1 km) compared to the diurnal libration amplitude. When observations are being interpreted, it is important to disentangle the diurnal and long-term librations. Once the diurnal libration is extracted from observations, then utilizing the sensitivity of this libration, the shell thickness can be constrained. This was done by Van Hoolst et al. (2016), who used the libration data from Thomas et al. (2016) and got an average shell thickness of 14-26 km for Enceladus. Using our model, we infer a shell thickness of 15-19 km corresponding to the libration data of Thomas et al. (2016) (Fig. 3.1a).

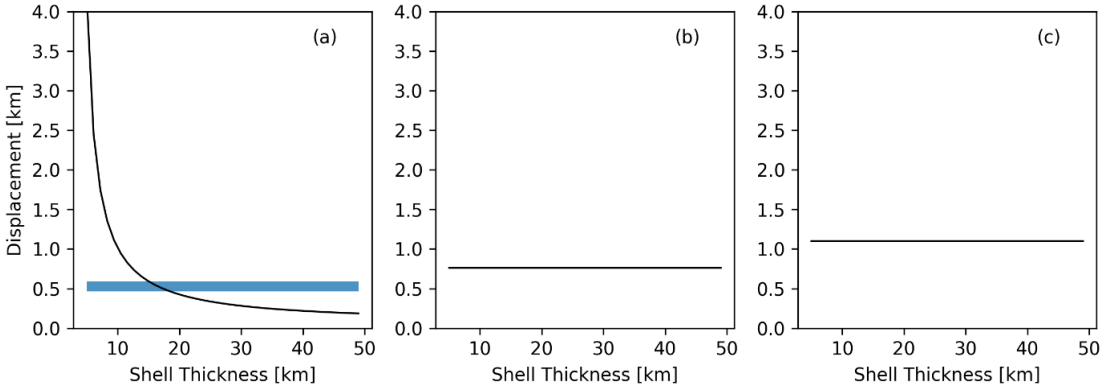


**Fig. 3. 1** Dependence of libration amplitudes (or displacements) at (a) 1.37-day, (b) 1423-day and (c) 4058-day periods on shell thickness. Blue region gives the observed libration amplitude at equator (Thomas et al. 2016).

### 3.5 Diurnal Libration Heating

Here we consider the heating effect of the diurnal forced libration. The heat contributed by long-term forced librations is assumed to be insignificant and not included here. The total tidal dissipation in the ice shell, including the diurnal libration heating effect, can be approximated by a simple equation (Wisdom 2004; Hurford et al. 2009):

$$E_t = \left[\frac{9}{2}e^2 + \frac{3}{2}(2e + F)^2\right] \times \frac{k_2}{Q_s}\frac{GM_p^2 n R_s^5}{a^6}, \qquad (3.8)$$

where $e$ is eccentricity, and $F$ is libration amplitude. $k_2$ and $Q_s$ are the Love number and the dissipation factor of the satellite. Note that $k_2$ here is for the whole satellite, different from that in equation (3.7) for a specific layer. $G$ is the gravitational constant. $M_p$ is the mass of the primary. $a$ is orbital radius. $n$ and $R_s$ are the mean motion and the radius of the satellite. This equation requires that the diurnal forced libration is out-of-phase with the optical libration (Hurford et al. 2009; Tiscareno et al. 2009), which is true for all our cases.

$k_2$ and $Q_s$ here are obtained from the complex degree-2 tidal Love number $\widetilde{k_2}$ calculated by the tidal model of Roberts and Nimmo (2008)

$$k_2 = Real\left(\widetilde{k_2}\right), \qquad Q_s = \frac{Real\left(\widetilde{k_2}\right)}{Imag\left(\widetilde{k_2}\right)}. \quad (3.9)$$

The complex Love number $\widetilde{k_2}$ relates to the surface value of the potential $\widetilde{y_5}$ solved by the correspondence principle (Tobie et al. 2005; Roberts and Nimmo 2008)

$$\widetilde{k_2} = -\left(\widetilde{y_5}|_{r=R_s,l=2}\right) - 1. \quad (3.10)$$

The tilde indicates a complex number, and $l$ is the spherical harmonic degree.

Our calculations show that the total tidal dissipation in the ice shell is dependent on the shell thickness (Fig. 3.2). The total tidal heating in the ice shell increases as the shell becomes thinner. This is due to the increase of both the Love number $k_2$ and the diurnal libration amplitude $F$ (Fig. 3.1a). The dissipation factor $Q_s$ increases (i.e., becomes less dissipative) by a factor of ~2 as the shell thickness decreases from 50 to 5 km, due to the decreased volume of low-viscosity ice region. The combined effect of the three factors, $k_2$, $F$ and $Q_s$, gives the dependency of the tidal heating in Fig. 3.2a: from 50 km to 10 km for the shell thickness, the heating increases slowly; from 10 km to 5 km, the heating rapidly increases. When the ice shell is ~5 km thick, the tidal heating in the ice shell could reach ~10 GW.

Enhancement of the shell tidal dissipation due to including the diurnal forced libration increases as the shell gets thinner (Fig. 3.2a). When the shell is ~17 km thick (within the inferred shell thickness range from our model and the libration observation), the diurnal forced libration increases the shell heating by ~27%. This percentage is consistent with that in Beuthe (2019), ~28% (the small difference of this value comes from the small difference between our calculated libration and the libration value used in that paper). When the shell is very thin, the heating

enhancement due to the forced libration dominates over that due to regular eccentricity tides.

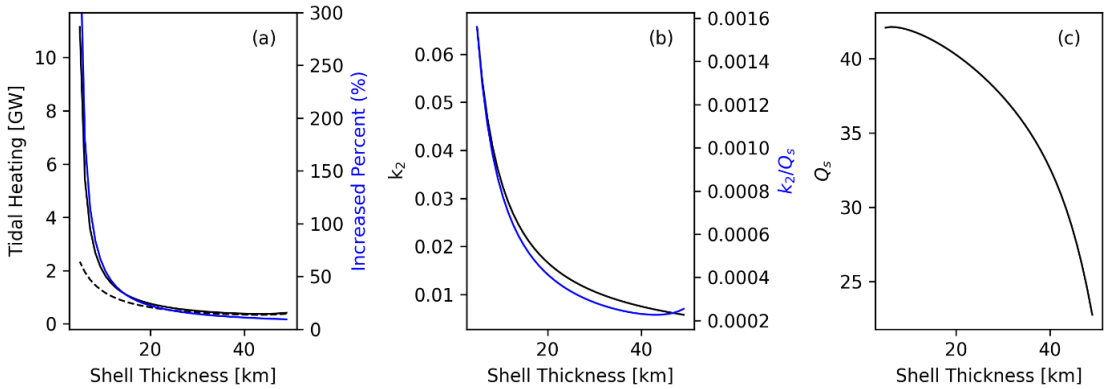


**Fig. 3. 2** (a) Shell tidal dissipation rate with (black solid line) and without (black dashed line) the diurnal forced libration included. Blue line shows the increased percentage of shell dissipation by including the diurnal forced libration. (b) Love number $k_2$ for different interior models. (c) Dissipation factor $Q_s$ for different interior models. The ratio of $k_2$ to $Q_s$ is also shown by the blue line in panel b.

We compare the total tidal heating rate to the surface heat flow of Enceladus to understand its current thermal state. Under the assumption that the ice shell is conductive and other assumptions as in Ojakangas and Stevenson (1989), the heat flow can be approximated as

$$H = -S\frac{c}{d}\ln\left(\frac{T_s}{T_b}\right), \qquad (3.11)$$

(Hemingway et al. 2018). $S$ is satellite global area. $c$ is a constant (567 W/m, e.g., Klinger 1980). $d$, $T_s$ and $T_b$ are the shell thickness, the surface temperature and the bottom temperature of the ice shell, respectively. The surface temperature is set at 75 K, and the bottom temperature at 273 K. A shell thickness of ~17 km implies a global conductive heat flow of ~34 GW.

However, even with the diurnal libration heating included, the total heating rate in the shell is still insufficient to explain the high heat flow on Enceladus's surface. In the model with the shell thickness of ~17 km, the total shell heating rate is ~0.9 GW (Fig 2a), less than the observed high heat flow on the SPT (~5-15 GW, Spencer et al. 2006, 2013; Howett et al. 2011) and certainly much less than the global conductive heat flow of ~34 GW required to maintain the shell in equilibrium. Only in extreme cases with very thin shells can the total shell heating rate approach 10 GW (Fig. 3.2a). However, these extreme cases also have extreme conductive cooling rates, and the shell's tidal heating in total is still not enough to balance the heat budget. Thus, if Enceladus is currently balancing its heat generation and loss, dissipation must be happening in either the ocean or the silicate interior, as well as in the ice shell.

### 3.6 Possible Thermal Equilibrium States of Enceladus

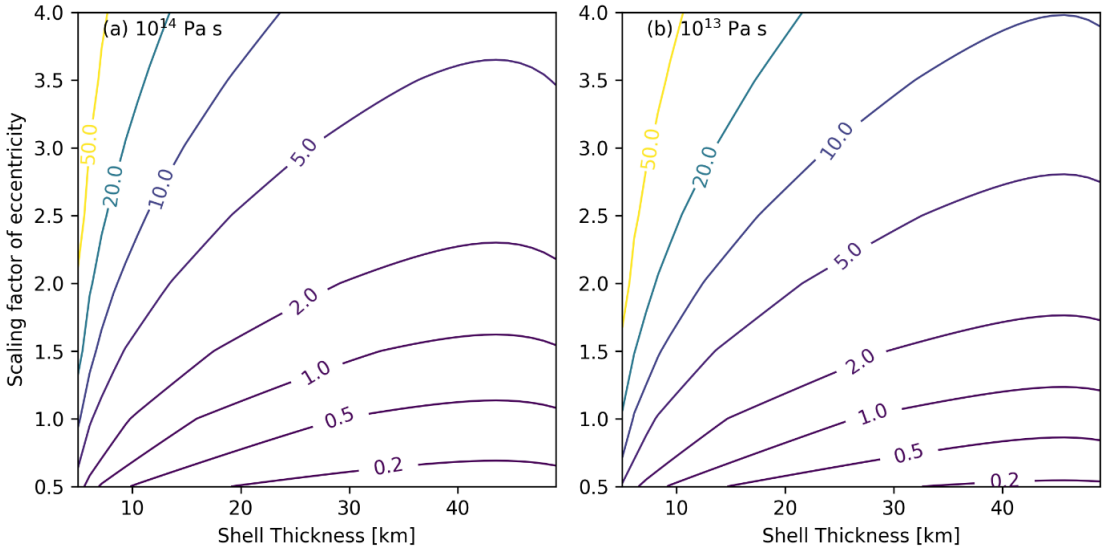


**Fig. 3. 3** Dependence of total shell heating rate (in GW) on shell thickness and eccentricity. Value of y axis is the scaling factor with respect to the current eccentricity of Enceladus (0.0047). Bottom viscosity of the ice shell is $10^{14}$ Pa s for (a) and $10^{13}$ Pa s for (b).

To consider Enceladus's possible thermal states in its past, we calculated the shell's total tidal dissipation with different eccentricities (Fig. 3.3). Different shell basal viscosities are also considered. Basically, larger eccentricity and lower viscosity produce more heat in the ice shell. From equation (3.8) the shell heating rate is proportional to $e^2$; if the eccentricity was 2 times the current value, the shell heating rate would have been 4 times the current value. As for the basal viscosity, the lower basal viscosity means larger low-viscosity volume in the ice shell and thus more tidal dissipation. For a fixed eccentricity the heat production generally decreases as shell thickness increases, because $k_2/Q$ and the forced libration amplitude both generally decrease with increasing shell thickness (Fig. 3.2).

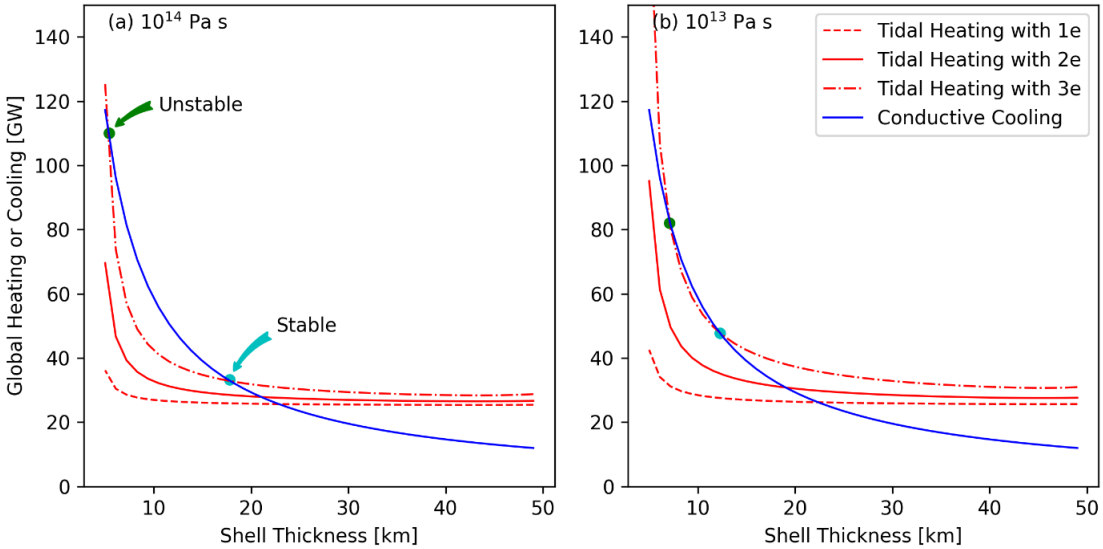


**Fig. 3. 4** Total global heating rate (red) versus conductive cooling rate (blue) for interior models with the shell basal viscosity of (a) $10^{14}$ Pa s and (b) $10^{13}$ Pa s. The heating consists of dissipation in the ice shell and a heat source of 25 GW below the shell. Different line styles indicate different orbital eccentricities. Enceladus's surface temperature is taken as 75 K. Stable and unstable equilibrium points are marked out.

Assuming Enceladus's shell is losing heat through conduction, we determine possible thermal equilibria of the shell. As mentioned in previous section, there are possibly other heat sources inside Enceladus beside those in the shell. Perhaps tidal friction in a porous core (Roberts 2015; Choblet et al. 2017; Liao et al. 2020) or turbulent dissipation in the ocean (e.g., Wilson and Kerswell 2018) could generate a significant amount of heat. Here we do not identify other heat sources; instead, we simply use an additional constant heating rate to represent the unknown heating mechanism(s) inside Enceladus. Note that the constant value assumed, 25 GW, is consistent with the astrometrically-derived heating rates (Fuller et al. 2016).

With this additional heating, present-day Enceladus could readily be in a stable thermal-equilibrium state resistant to small perturbations. The total tidal heating of Enceladus's ice shell is relatively insensitive to the shell thickness, inherited from our assumption that the unknown heating mechanism(s) is(are) independent of the shell thickness. In this situation, once thermal equilibrium is reached, a small perturbation to the shell thickness would be resisted by this thermal state. For example, if the shell thickness is decreased by a small percentage, the conductive cooling rate will become larger than the total heating rate (Fig. 3.4). This would cause the ice shell to freeze and return to the original equilibrium point. At the present day, therefore, it appears that heat in the ice shell represents a small fraction of the total heat, and Enceladus could maintain thermal equilibrium against small perturbations to ice shell thickness.

However, it is also possible that Enceladus is not heat-balanced. In this situation, Enceladus is cooling, and its subsurface ocean is freezing with time (i.e., to the left of

the stable point in Fig. 3.4). Or on the contrary, Enceladus is heating, and its ice shell is melting (i.e., to the right of the stable point in Fig. 3.4). In either case Enceladus will tend to move back towards equilibrium, but the details would depend on the melting/freezing timescale of the ice shell compared to the eccentricity damping timescale and could in principle result in oscillatory behaviour. Coupled thermal-orbital models of this kind have been investigated in the past (e.g., Ojakangas & Stevenson 1986; Shoji et al. 2014), but are beyond the scope of this work.

Even with a higher eccentricity, Enceladus will still generally be in stable thermal equilibrium (Fig. 3.4). Thus, a thermal runaway of the kind envisaged by Luan and Goldreich (2017) is unlikely to occur in the recent past. In the thermal-runaway scenario, when the ice shell thickness decreases, tidal dissipation increases, and this in turn melts ice and decreases the ice shell thickness further. Runaway melting may occur. Our results, however, do not support this scenario. In our work, equation (3.11) gives a strong dependence of conductive loss on shell thickness. In Fig. 3.4, conductive heat loss increases more rapidly than tidal dissipation as ice shell gets thinner, and this prevents the thermal runaway of Enceladus from occurring. This stable equilibrium implies that the multiple resurfacing events inferred for the past of Enceladus (e.g., Giese et al. 2008) may not have arisen from some intrinsic instability of ice shell. More likely possibillities include passage through earlier orbital mean-motion resonances (e.g. Meyer & Wisdom 2008a) or (perhaps) impactors (Roberts and Stickle 2021).

In some extreme cases (thin ice shell, high eccentricity and low viscosity), there is an unstable equilibrium point vulnerable to small perturbations (Fig. 3.4). If Enceladus was once in this point, a runaway process as described above could have occurred. But, quite apart from the extreme parameter choices required, we are then faced with the question of how to put Enceladus into such an unstable point. More information about Enceladus's past is needed to facilitate the investigation of such an unstable thermal state.

### 3.7 Discussion and Conclusions

In this study, we investigated the libration heating effect on Enceladus's thermal state. We found that the ice shell tidal dissipation including the diurnal libration heating is significantly dependent on ice shell thickness, and a ~17 km thick ice shell can generate heat of ~0.9 GW. When the ice shell is very thin, heat enhancement due to the diurnal forced libration dominates the heat generation in the ice shell. The ice shell dissipation is far from being sufficient to match the conductive cooling rate (~34 GW for a ~17 km thick shell) required for Enceladus to be in steady state. Either present-day Enceladus is not in thermal equilibrium, or there are additional large heating sources beneath the ice shell, keeping Enceladus in steady state. If, as seems likely, these additional heating sources are independent of shell thickness, Enceladus could be in a thermal equilibrium state where small perturbations to shell thickness are resisted.

A higher eccentricity Enceladus in the past would also likely have been in a similar, thermally stable state resistant to small perturbations. Any runaway melting process (if it occurred) or episodic heating is unlikely to have originated from librations of the ice shell. There are unstable equilibrium points under some extreme cases (thin shell, high eccentricity and low viscosity), but many unknowns about Enceladus's history leave the investigation of such an unstable point to the future.

One deficit of our study is that we do not calculate the mutual feedbacks between thermal evolution and orbital evolution. Ojakangas and Stevenson (1986) did this coupling for Io and found that unstable or periodic regime can occur. Even though they focused on the convective heat flow on Io, their results also implied a possible cyclic solution for the resurfacing of Enceladus. Meyer and Wisdom (2008b) found that the Ojakangas and Stevenson (1986) mechanism did not produce periodic behavior at Enceladus, but there are certainly other possible modes of cyclic behavior, including that suggested by Luan and Goldreich (2017). While our results do not suggest that librationally-driven thermal runaways occur at Enceladus, coupling of thermal evolution and orbital evolution is a rich topic, and whether it can solve the question of episodic heating events at Enceladus deserves more attention in the future.

# Appendices

## Appendix A. Steady State Problem in the Kinetics Model

As stated in the main text, using the traditional convergence criterion, that is, checking the abundance differences of the chemical species in two successive time steps, we can reproduce the simulation results of P15. But we found in some cases the eddy diffusion and net production terms in the right hand side of Equation (1) do not balance each other for every species. For example, in Fig. S1.1 (a-c), we show diffusive flux divergence and net chemical production for three species, $SO_2$, $H_2O$ and $SO_3$, respectively. For each species, the two terms differ by several orders of magnitude, although the model claims it has reached the apparent "steady state" under the traditional convergence criterion. We attribute the reason to the exponential time marching scheme used in the implicit solver in the model. This scheme can make the traditional convergence criterion not accurate for the stiff system because the time step could become very large as time evolves. We went back to check published JPL/Caltech Kinetics Venus models prior to P15 (e.g., Yung & DeMore, 1982; Mills, 1998; Zhang et al., 2012), which usually fixed the $H_2O$ abundance profile (but P15 did not) and employed the exponential time marching. But we found those models reached the steady states. The exact cause for the different behaviors between P15 and earlier models is still not very clear and probably depends on the stiffness of the specific chemical system and how fast we increase the time step in the simulations. Our exercise implies that one should be cautious about the exponential time marching scheme in the stiff chemical system simulations.

To ensure that the model simulations reach the real steady states, that is, diffusion and net production are equal to each other for each species, we take the apparent "steady state" output by the model as the new initial condition and restart the model from a small time step. We repeat this process until the steady state satisfies Equation (1) for each species. Using this new criterion, the model can reach the real steady state. Fig. S1.1 (d-f) show diffusive flux divergence and net production of $SO_2$, $H_2O$ and $SO_3$ for one case. The case has the same parameter setting with that of P15 shown in Fig. S1.1 but now the two terms are equal for each species. Consequently, our simulation results are very different from that in P15, as shown in Fig. S1.2.

## Appendix B. Supporting Figures for Chapter I

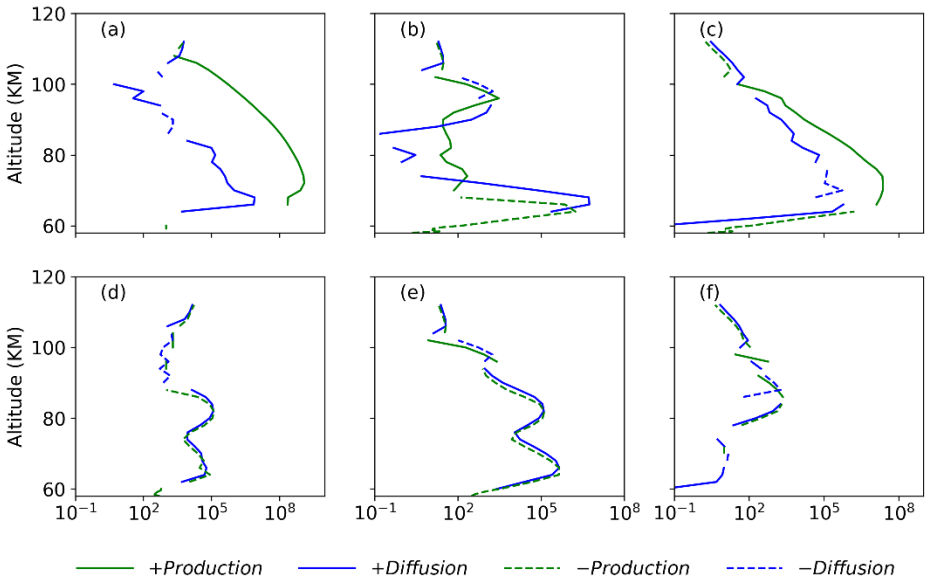


**Fig. S1. 1** Net production rates (green) and divergences of eddy diffusive fluxes (blue) for $SO_2$ (left), $H_2O$ (middle) and $SO_3$ (right) from P15 (top) and our work (bottom). The results are from a case with 40 ppm $SO_2$ and 10 ppm $H_2O$ at the lower boundary at 58 km. Solid lines are positive values and dashed are negative. Units of those values are $cm^{-3} \cdot s^{-1}$.

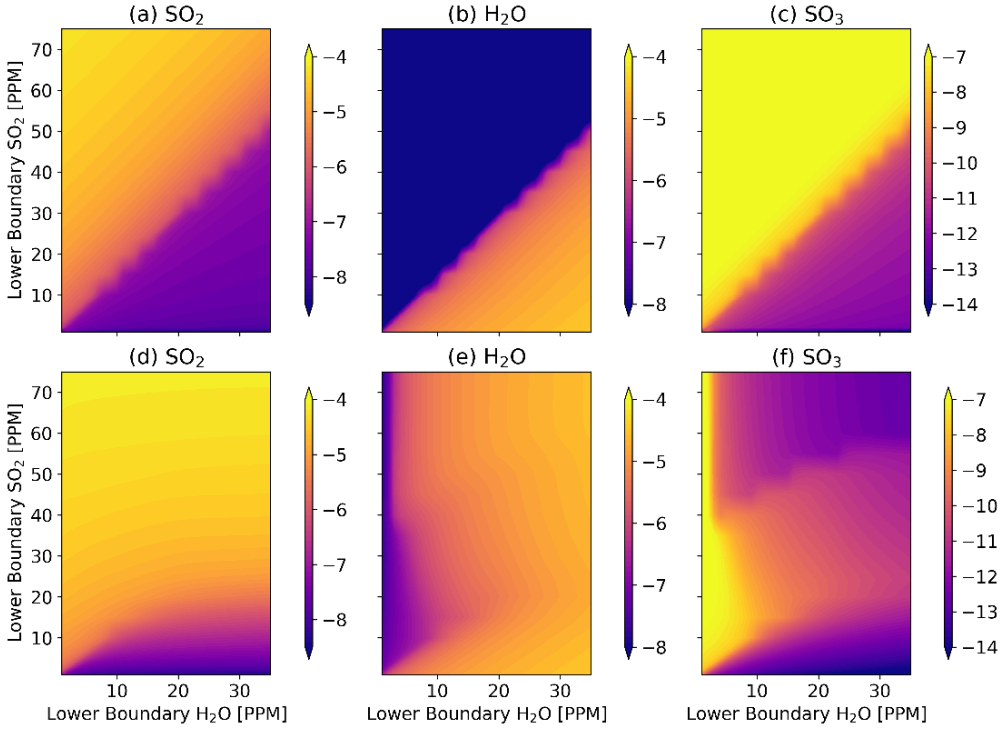

**Fig. S1. 2** Mixing ratios of $SO_2$ (left), $H_2O$ (middle), and $SO_3$ (right) at 80 km as functions of $SO_2$ and $H_2O$ mixing ratios at 58 km from simulations of P15 (top) and our work (bottom). Colors are volume mixing ratios in a logarithmic scale. Lower boundary $H_2O$ ranges from 1 to 35 ppm, and lower boundary $SO_2$ ranges from 1 to 75 ppm.

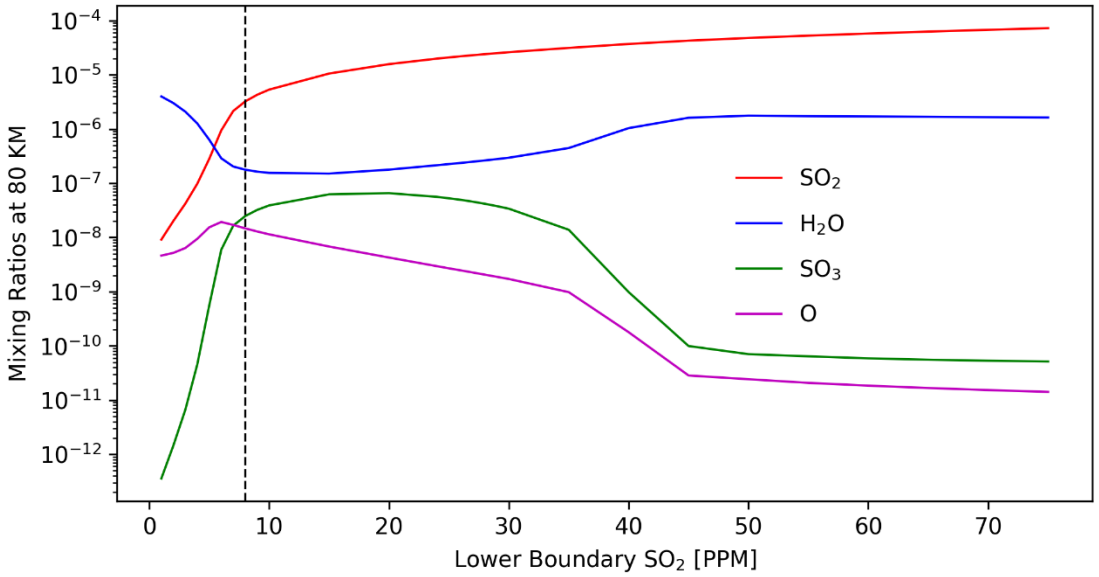


**Fig. S1. 3** Same as Fig.2 except that $H_2O$ mixing ratio at 58 km is fixed as 5 ppm.

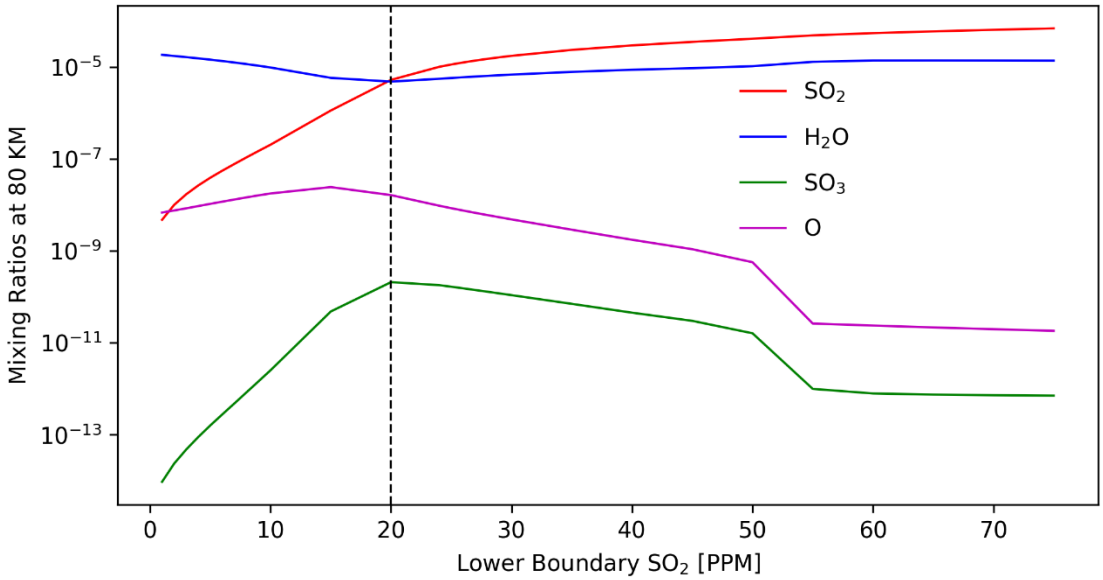


**Fig. S1. 4** Same as Fig.2 except that $H_2O$ mixing ratio at 58 km is fixed as 20 ppm.

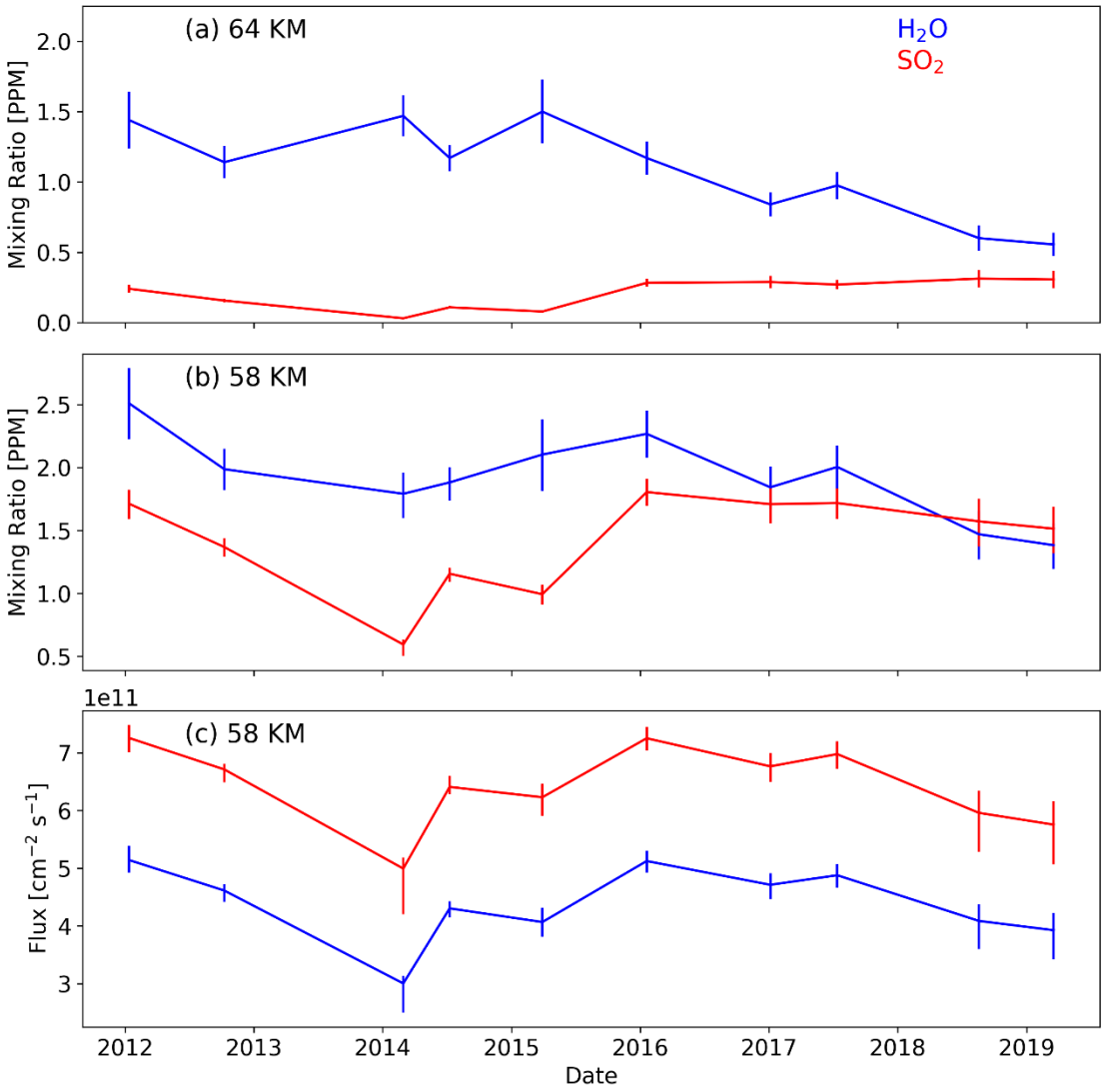


**Fig. S1. 5** (a)Time series of $H_2O$ (blue) and $SO_2$ (red) disk-averaged mixing ratios at 64 km from the TEXES/IRTF. (b) Time series of mixing ratios and (c) fluxes at 58 km from the simulations that match the TEXES observations.

## Appendix C. Meridionally-mean Chemical Transport Equation

Our CTM uses the log-pressure-longitude coordinate to solve the continuity equation. From Chapter 9 and 10 in Andrews et al. (1987), the continuity equation for volume mixing ratio $\chi$ of a minor species is

$$(\rho_0\chi)_t + \frac{(\rho_0\chi u)_\lambda + (\rho_0\chi v\cos\phi)_\phi}{a\cos\phi} + (\rho_0\chi w)_z = \rho_0 S. \quad (C1)$$

Here $\rho_0 = \rho_s \exp\{-z/H\}$ is the reference background density, and $\rho_s$ and $H$ are the density at a reference level (bottom boundary) and a characteristic scale height that does not vary with height. $t$ is time. $\lambda$, $\phi$, and $z$ are longitude, latitude, and height in the log-pressure coordinate, respectively, and $u$, $v$, and $w$ are velocities in three directions. $a$ is the planetary radius. $\rho_0 S$ represents chemical production and loss rates. Subscript represents the partial derivative with respect to each coordinate.

Multiplying equation (C1) by $\cos\phi\ d\phi$, integrating it from one pole to the other pole over the meridional direction, and dividing it by $\int_{-\pi/2}^{\pi/2}\cos\phi\, d\phi$, we get

$$(\rho_0\overline{\chi}\,)_t + \frac{\left(\rho_0\overline{\chi u^*}\,\right)_\lambda}{a} + (\rho_0\overline{\chi w})_z = \rho_0\overline{S}, \qquad (C2)$$

where the overbar represents the average of any quantity $x$ over latitude

$$\overline{x} = \frac{\int_{-\pi/2}^{\pi/2} x\cos\phi\, d\phi}{\int_{-\pi/2}^{\pi/2}\cos\phi\, d\phi}, \qquad (C3)$$

and $u^* = u/\cos\phi$.

Doing the same operation to the continuity equation for the background atmosphere

$$\frac{(\rho_0 u)_\lambda + (\rho_0 v\cos\phi)_\phi}{a\cos\phi} + (\rho_0 w)_z = 0, \qquad (C4)$$

we can get a similar expression

$$\frac{\left(\rho_0\overline{u^*}\right)_\lambda}{a} + (\rho_0\overline{w})_z = 0. \quad (C5)$$

Combining equations (C2) and (C5) and using

$$\overline{x_1 x_2} = \overline{x_1}\,\overline{x_2} + \overline{x_1' x_2'}, \quad (C6)$$

where $x_1$ and $x_2$ are any two quantities, and $x_i' = x_i - \overline{x_i}$ $(i = 1, 2)$ is the deviation from the mean, we get

$$(\rho_0\overline{\chi})_t + \frac{\rho_0\overline{u^*}\,(\overline{\chi})_\lambda}{a} + \rho_0\overline{w}(\overline{\chi})_z = \rho_0\overline{S} - \left\{\frac{\left(\rho_0\overline{\chi' u^{*\prime}}\right)_\lambda}{a} + \left(\rho_0\overline{\chi' w'}\right)_z\right\}. \quad (C7)$$

We can parameterize the deviation term in the curly bracket as diffusion:

$$\begin{aligned}(\rho_0\overline{\chi})_t + \frac{\rho_0\overline{u^*}\,(\overline{\chi})_\lambda}{a} + \rho_0\overline{w}(\overline{\chi})_z \\ = \rho_0\overline{S} \\ - \left\{\left(\frac{\rho_0}{a^2}K_{xx}\overline{\chi}_\lambda + \frac{\rho_0}{a}K_{xz}\overline{\chi}_z\right)_\lambda + \left(\rho_0 K_{zz}\overline{\chi}_z + \frac{\rho_0}{a}K_{zx}\overline{\chi}_\lambda\right)_z\right\}. \quad (C8)\end{aligned}$$

This is the tracer continuity equation in the log-pressure-longitude plane, derived based on the traditionally defined longitude-latitude coordinate.

**Appendix D. Fast Chemical Cycles**

When calculating the chemical lifetimes of $SO_2$, SO and CO, we exclude some fast chemical cycles. We list these cycles here for a reference.

There are two fast cycles in the $SO_2$-related network. One involves species $Cl_2$:

$$\left.\begin{array}{c} 2Cl + 2SO_2 + 2M \rightarrow 2ClSO_2 + 2M \\ 2ClSO_2 \rightarrow Cl_2 + 2SO_2 \\ Cl_2 \rightarrow 2Cl \end{array}\right\}. \quad (D1)$$

The other involves species SO:

$$\left.\begin{array}{c} Cl + SO_2 + M \rightarrow ClSO_2 + M \\ SO + ClSO_2 \rightarrow OSCl + SO_2 \\ OSCl + M \rightarrow Cl + SO + M \end{array}\right\}. \quad (D2)$$

For SO, besides the cycle (B2), there is another fast cycle involving the SO dimer:

$$\left.\begin{array}{c} 2SO + M \rightarrow (SO)_2 + M \\ (SO)_2 + M \rightarrow 2SO + M \end{array}\right\}. \quad (D3)$$

For CO, there are two fast cycles:

$$\left.\begin{array}{c} Cl + CO + CO_2 \rightarrow ClCO + CO_2 \\ ClCO + CO_2 \rightarrow Cl + CO + CO_2 \end{array}\right\}, \quad (D4)$$

and

$$\left.\begin{array}{c} Cl + CO + N_2 \rightarrow ClCO + N_2 \\ ClCO + N_2 \rightarrow Cl + CO + N_2 \end{array}\right\}. \quad (D5)$$

In Fig. 2.1, 2.3 and 2.9, we have shown the chemical lifetime calculations for $SO_2$, CO and SO with these fast cycles excluded. Fig. D1 shows the chemical lifetime calculations when these cycles are included. Comparing Fig. D1 to Fig. 2.1, 2.3 and 2.9, we found that including these cycles when calculating the chemical lifetime would give unreasonable results. For example, CO appears short-lived in the upper cloud on the dayside (panel e of Fig. D1).

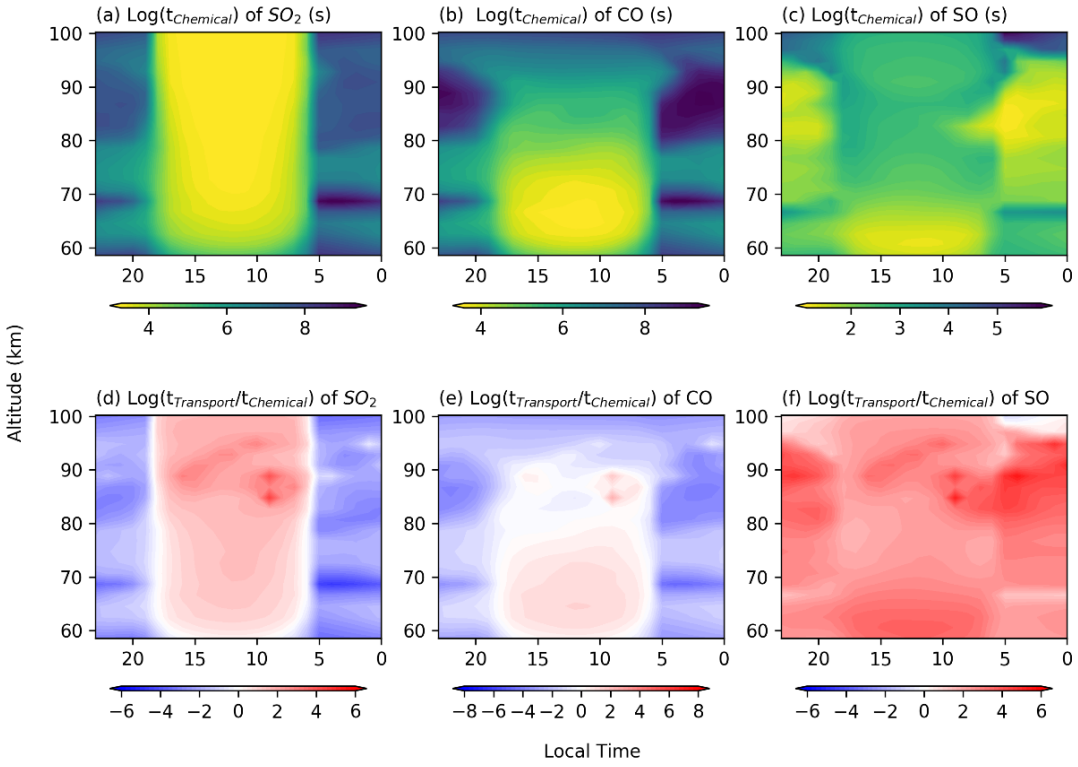


**Fig. D 1** Chemical lifetimes of (a) $SO_2$, (b) CO and (c) SO if the fast cycles in Appendix D are included. Panels d-f are the ratios of $t_{Transport}$ to $t_{Chemical}$ for the three species when the fast cycles are included.

## Appendix E. Supporting Figures for Chapter II

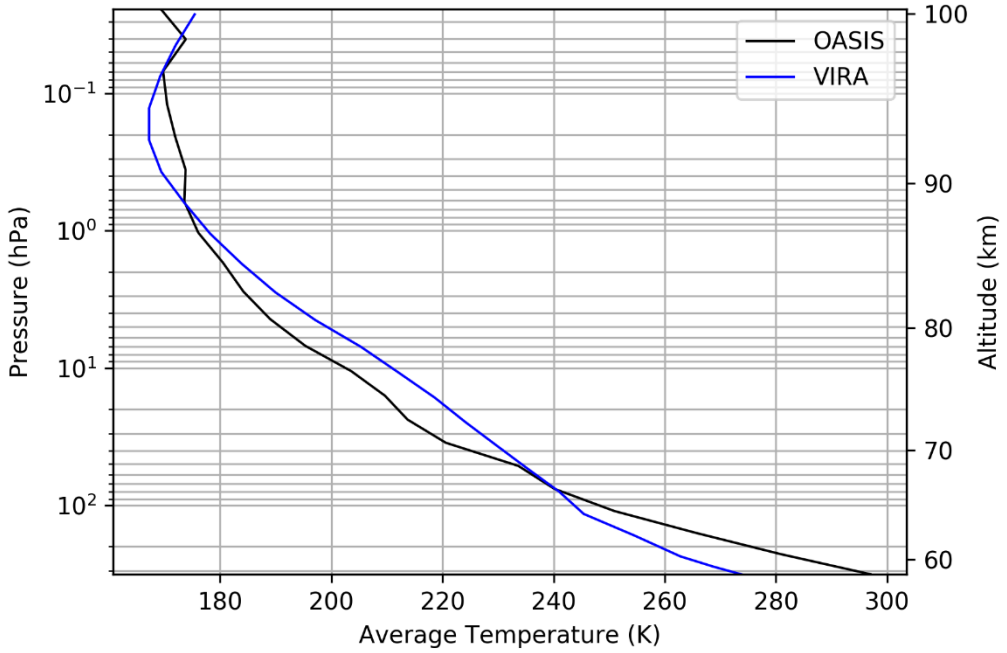


**Fig. S2. 1** Average temperature profile simulated by our GCM (black) and VIRA temperature profile (blue). The temperature anomaly in Fig. 2.1 is the deviation from this GCM's average temperature profile.

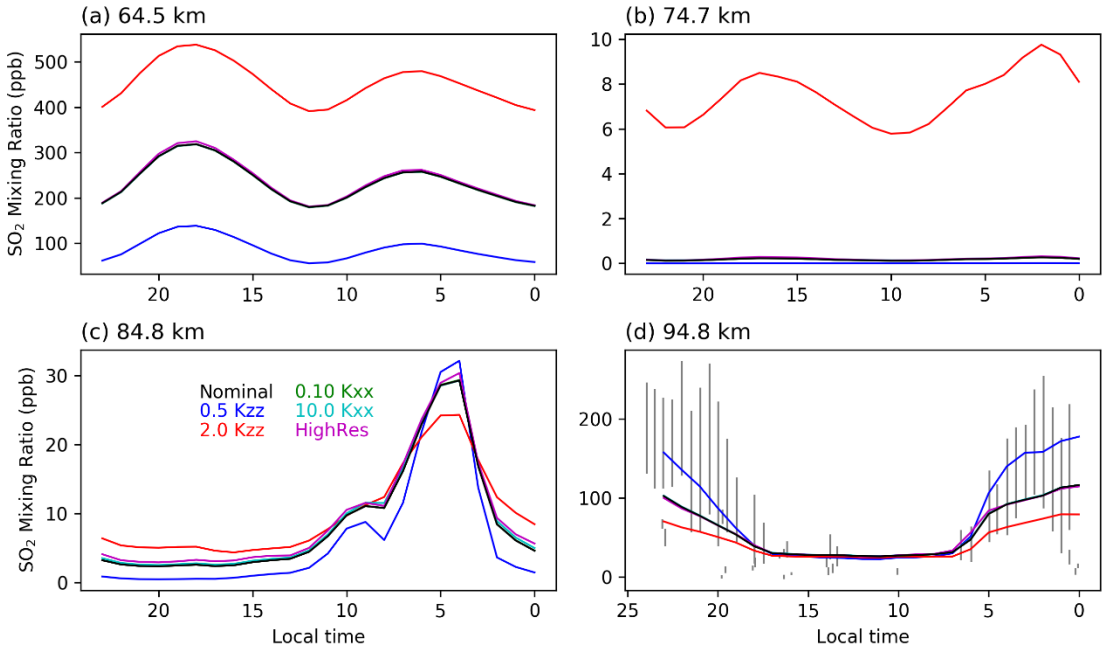

**Fig. S2. 2** Local-time distributions of $SO_2$ mixing ratio at different altitudes (a-d) for different cases: our nominal case (black); cases with Kzz enlarged by 1.5 (blue) and 2.0 (red); cases with $K_{xx}$ changed by a factor of 0.1 (green) and 10.0 (cyan); case with a higher (double) horizontal resolution (magenta). Note that green, cyan, and black lines are almost overlapping with each other. In panel d, error bars show observations at 95-100 km from SPICAV/VEx by Belyaev et al. (2017) and observations at 70-100 km from JCMT by Sandor et al. (2010).

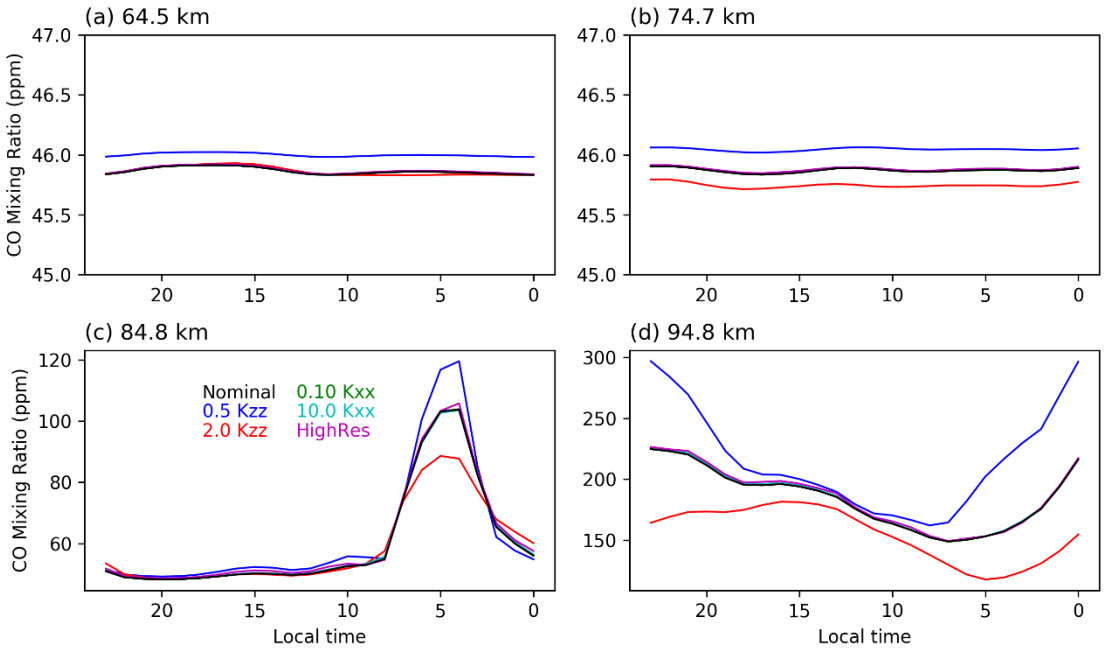


**Fig. S2. 3** Same as Fig. S2.2 but for CO.

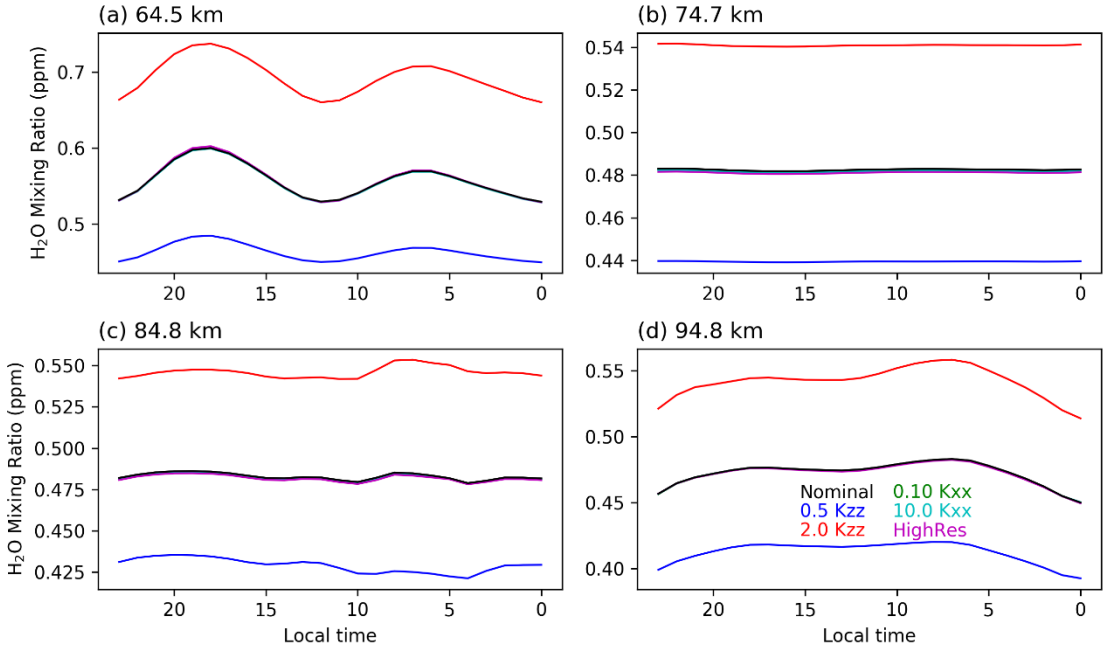


**Fig. S2. 4** Same as Fig. S2.2 but for $H_2O$.

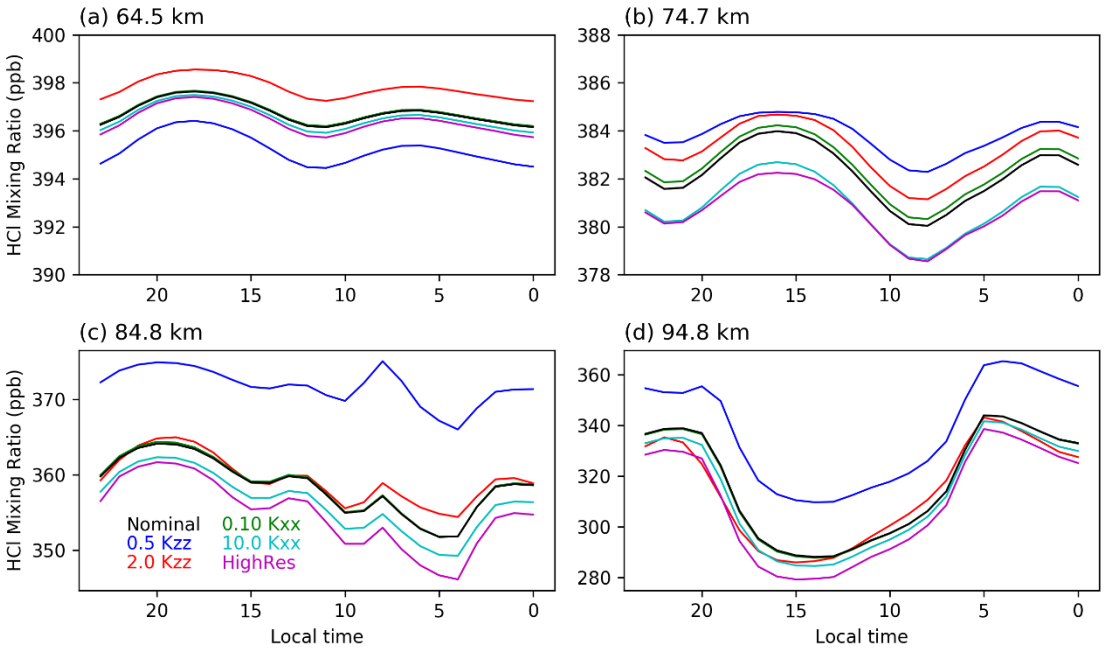


**Fig. S2. 5** Same as Fig. S2.2 but for HCl.

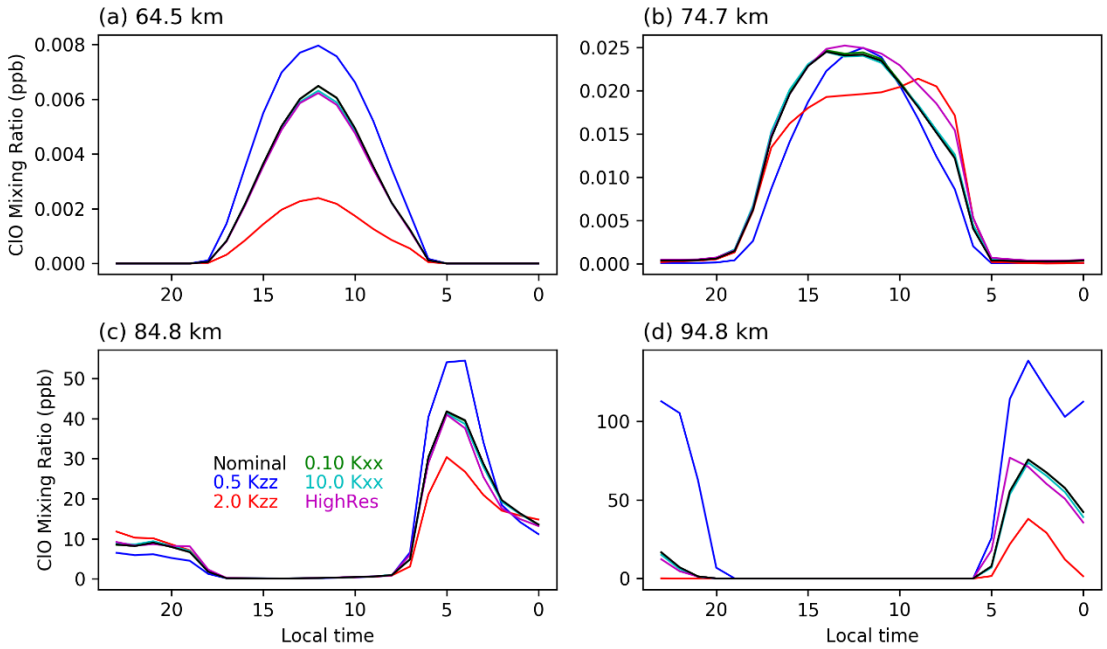


**Fig. S2. 6** Same as Fig. S2.2 but for ClO.

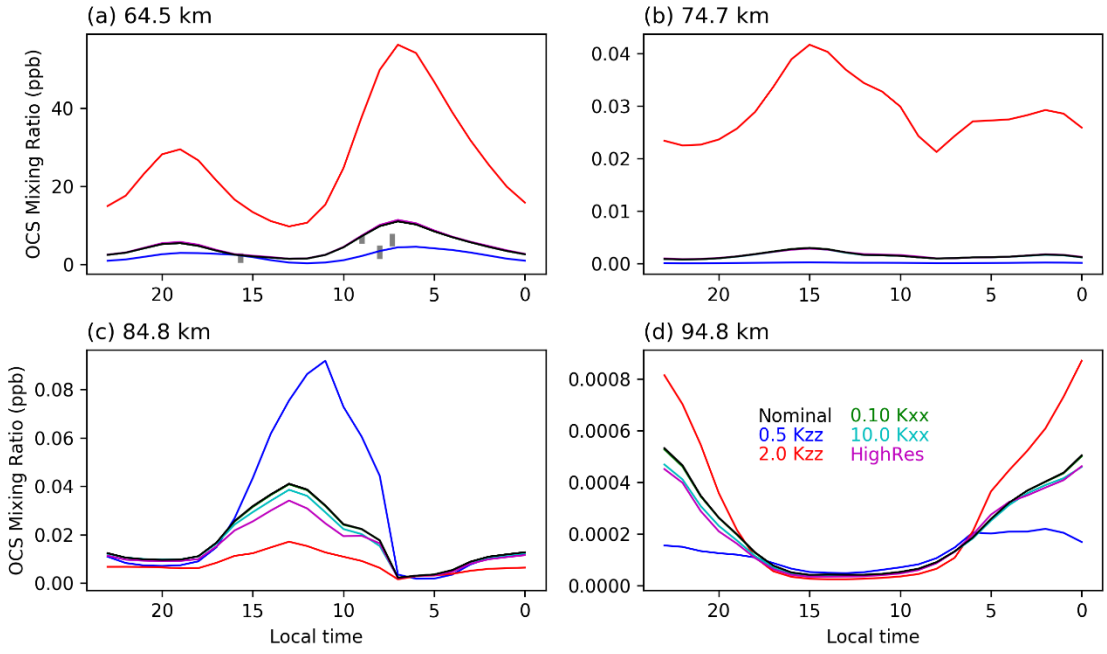


**Fig. S2. 7** Same as Fig. S2.2 but for OCS. In panel a, grey bars show a few observation points near 65 km from CSHELL/IRTF by Krasnopolsky (2010).

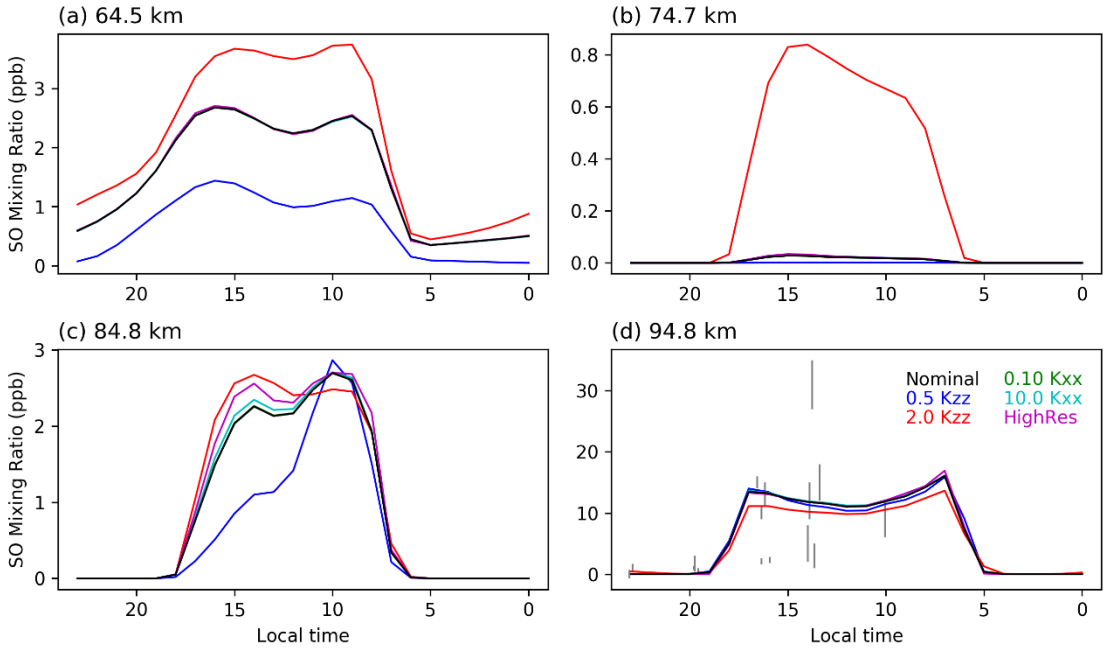


**Fig. S2. 8** Same as Fig. S2.2 but for SO. In panel d, error bars show observations at 70-100 km from JCMT by Sandor et al. (2010).

## Appendix F. Viscosity Profile in the Ice Shell

The tidal model of Roberts and Nimmo (2008) requires specification of viscosity for each layer. For viscosity of the silicate core, we adopt a large value, $10^{25}$ Pa s (Table 3.2). For the viscosity of the ocean, we adopt a small value, $10^{8}$ Pa s (Table 3.2). For the viscosity of the ice shell, we further divide the shell into multiple sub-layers with different viscosities to more accurately calculate Enceladus's radial displacements and dissipation factor.

According to Ojakangas and Stevenson (1989), under reasonable assumptions, the gradient of ln $(T)$ is nearly constant through the majority of the ice shell, where $T$ is temperature. Thus, the temperature profile can be approximated as

$$\ln T = \frac{\ln (T_b/T_s)}{d} z + \ln T_s, \qquad (F1)$$

where $T_b$ and $T_s$ are the bottom and surface temperature of the ice shell, $d$ is the shell thickness, and $z$ is the vertical coordinate (positive being downward). Ice viscosity $\eta$ relates to temperature through the Arrhenius relation

$$\eta = \eta_0 \exp\left\{l\left(\frac{T_M}{T} - 1\right)\right\}. \quad (F2)$$

Here $T_M$ is the melting temperature of ice, $l$ is a coefficient, and $\eta_0$ is the viscosity at the melting temperature. In this paper, we assume $T_b = T_M = 273\ K$, $l = 24.0$, and $\eta_0 = 10^{14}\ Pa \cdot s$. $\eta_0$ is also the basal viscosity of the ice shell.

We use equations (F1-2) to construct the sub-layers in the ice shell. We first set the viscosity ranging from $10^{14}$ to $10^{22}$ Pa s (values above $10^{22}$ Pa s will contribute negligible dissipation), then use equation (F2) to derive the temperature, and finally use equation (F1) to derive the ratio $z/d$. This ratio is assumed as the radial position of the midpoint of each sub-layer, and then the positions of the lower and upper surfaces for each sub-layer can be obtained through average of adjacent midpoints. Table F1 shows the calculated results for each sub-layer.

**Table F 1** Viscosity for each sub-layer.

| Sub-layer Index | Viscosity (Pa s) | Temperature (K) | Ratio *z/d* |
|---|---|---|---|
| 1 | $10^{14}$ | 273.0 | 1.00 |
| 2 | $10^{15}$ | 249.1 | 0.93 |
| 3 | $10^{16}$ | 229.0 | 0.86 |
| 4 | $10^{17}$ | 212.0 | 0.80 |
| 5 | $10^{18}$ | 197.3 | 0.75 |
| 6 | $10^{19}$ | 184.5 | 0.70 |
| 7 | $10^{20}$ | 173.3 | 0.65 |
| 8 | $10^{21}$ | 163.3 | 0.60 |
| 9 | $10^{22}$ | 154.5 | 0.56 |

## Appendix G. Example of Libration Calculations

Here we give an example of calculation using the methodology described in Section 3.2. In this example, the interior model has a shell thickness of 20.4 km. Table G1 gives the calculations.

**Table G 1** Example of libration calculation for the shell thickness of 20.4 km

| Physical quantity | Symbol | Value |
|---|---|---|
| Shell thickness (km) | d | 20.4 |
| Radial displacements at the upper surface of each layer | $y^i$ | 0.00426098 |
| | $y^o$ | 0.405993 |
| | $y^s$ | 0.394497 |
| Dynamical Love number of each layer | $k_2^i$ | 0.000143322 |
| | $k_2^{ob}$ | -0.000057987 |
| | $k_2^{ot}$ | 0.012261138 |
| | $k_2^s$ | 0.003988245 |
| Coefficients in equations (3.5-3.6) | $K_1$ | $3.05 \times 10^{20}$ |
| | $K_2$ | $-6.02 \times 10^{19}$ |
| | $K_3$ | $1.23 \times 10^{20}$ |
| | $K_4$ | $-5.88 \times 10^{19}$ |
| | $K_5$ | $1.44 \times 10^{20}$ |
| | $K_6$ | $4.28 \times 10^{19}$ |
| Polar moment of inertia for the shell and the core | $C_s$ | $5.36 \times 10^{29}$ |
| | $C_i$ | $1.03 \times 10^{30}$ |
| Total dynamical Love number | $k_2$ | 0.0163274 |
| Dissipation factor | $Q_s$ | 40.18 |
| Diurnal libration amplitude (km) | $\gamma_s \cdot R_s$ | 0.414 |

*Physical quantity uses the SI unit if its unit is not specified.

## Appendix H. Supporting Tables and Figures for Chapter III

**Table S3. 1** Similar to Table 3.1, but using the Hann window.

| Frequency (rad/day) | Period (days) | Magnitude (arc second) | Phase (degree) |
|---|---|---|---|
| 4.579656 | 1.371978 | 1841.35 | 111.63 |
| 0.001548 | 4058.259259 | 925.12 | 163.82 |
| 0.004415 | 1423.025974 | 656.43 | 46.87 |
| 4.578107 | 1.372442 | 33.22 | -142.22 |
| 0.000057 | 109573.000000 | 16.21 | -110.52 |
| 0.005849 | 1074.245098 | 14.92 | -122.53 |
| 0.002179 | 2883.500000 | 9.52 | 136.39 |
| 0.001147 | 5478.650000 | 8.56 | -153.91 |
| 4.575183 | 1.373319 | 8.29 | -25.24 |
| 3.771700 | 1.665876 | 7.64 | -99.41 |
| 5.028934 | 1.249407 | 7.44 | -102.55 |
| 0.000573 | 10957.300000 | 6.53 | 50.04 |
| 2.514467 | 2.498814 | 6.51 | 83.72 |
| 4.581204 | 1.371514 | 6.48 | 5.24 |
| 0.008831 | 711.512987 | 5.69 | -176.28 |
| 1.257233 | 4.997628 | 5.40 | -93.14 |

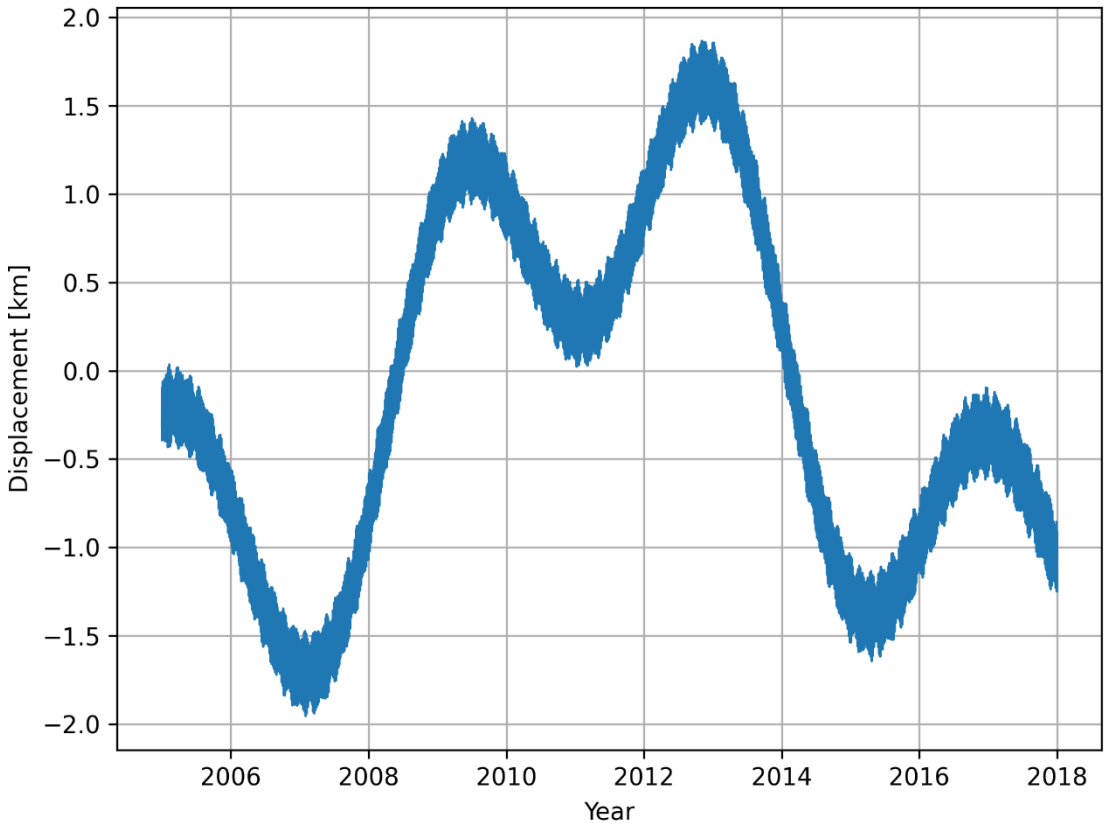


**Fig. S3. 1** Variation of physical libration displacement (km) of Enceladus over 2005-2018 period. In this calculation, we used the same interior model as that for Fig. 2a in Rambaux et al. (2010). We did not include viscosity effect here since it only gives a small change to the results (refer to Rambaux et al. 2010). We did not include the free libration here since our model may break around the free frequency due to the small amplitude assumption (Rambaux et al. 2011), and libration terms in Rambaux et al. (2010) also did not include the free-frequency term. This figure is aimed to be a reproduction of Fig. 2a in Rambaux et al. (2010) to validate the accuracies of both the dataset and the method we used in this work.

# Bibliography


Andrews, D. G., Holton, J. R., & Leovy, C. B. (1987). *Middle Atmosphere Dynamics*. Academic Press.

Běhounková, M., Tobie, G., Čadek, O., Choblet, G., Porco, C., & Nimmo, F. (2015). Timing of water plume eruptions on Enceladus explained by interior viscosity structure. *Nature Geoscience*, *8*(8), 601–604. https://doi.org/10.1038/ngeo2475

Belyaev, D. A., Evdokimova, D. G., Montmessin, F., Bertaux, J.-L., Korablev, O. I., Fedorova, A. A., Marcq, E., Soret, L., & Luginin, M. S. (2017). Night side distribution of SO2 content in Venus' upper mesosphere. *Icarus*, *294*, 58–71. https://doi.org/10.1016/j.icarus.2017.05.002

Belyaev, D. A., Montmessin, F., Bertaux, J.-L., Mahieux, A., Fedorova, A. A., Korablev, O. I., Marcq, E., Yung, Y. L., & Zhang, X. (2012). Vertical profiling of SO2 and SO above Venus' clouds by SPICAV/SOIR solar occultations. *Icarus*, *217*(2), 740–751. https://doi.org/10.1016/j.icarus.2011.09.025

Bertaux, J.-L., Vandaele, A.-C., Korablev, O., Villard, E., Fedorova, A., Fussen, D., Quémerais, E., Belyaev, D., Mahieux, A., Montmessin, F., Muller, C., Neefs, E., Nevejans, D., Wilquet, V., Dubois, J. P., Hauchecorne, A., Stepanov, A., Vinogradov, I., & Rodin, A. (2007). A warm layer in Venus' cryosphere and high-altitude measurements of HF, HCl, H2O and HDO. *Nature*, *450*(7170), 646–649. https://doi.org/10.1038/nature05974

Beuthe, M. (2019). Enceladus's crust as a non-uniform thin shell: II tidal dissipation. *Icarus*, *332*, 66–91. https://doi.org/10.1016/j.icarus.2019.05.035

Beuthe, M., Rivoldini, A., & Trinh, A. (2016). Enceladus's and Dione's floating ice shells supported by minimum stress isostasy. *Geophysical Research Letters*, *43*(19), 10,088-10,096. https://doi.org/10.1002/2016GL070650

Bierson, C. J., & Zhang, X. (2020). Chemical cycling in the Venusian atmosphere: A full photochemical model from the surface to 110 km. *Journal of Geophysical Research: Planets*, *125*(7), e2019JE006159.

Bougher, S. W., Rafkin, S., & Drossart, P. (2006). Dynamics of the Venus upper atmosphere: Outstanding problems and new constraints expected from Venus Express. *Planetary and Space Science*, *54*(13), 1371–1380. https://doi.org/10.1016/j.pss.2006.04.023

Čadek, O., Tobie, G., Van Hoolst, T., Massé, M., Choblet, G., Lefèvre, A., Mitri, G., Baland, R.-M., Běhounková, M., Bourgeois, O., & Trinh, A. (2016). Enceladus's internal ocean and ice shell constrained from Cassini gravity, shape, and libration data. *Geophysical Research Letters*, *43*(11), 5653–5660. https://doi.org/10.1002/2016GL068634

Chamberlain, S., Mahieux, A., Robert, S., Piccialli, A., Trompet, L., Vandaele, A. C., & Wilquet, V. (2020). SOIR/VEx observations of water vapor at the terminator in the Venus mesosphere. *Icarus*, *346*, 113819. https://doi.org/10.1016/j.icarus.2020.113819

Chen, E. M. A., & Nimmo, F. (2011). Obliquity tides do not significantly heat Enceladus. *Icarus*, *214*(2), 779–781. https://doi.org/10.1016/j.icarus.2011.06.007

Choblet, G., Tobie, G., Sotin, C., Běhounková, M., Čadek, O., Postberg, F., & Souček, O. (2017). Powering prolonged hydrothermal activity inside Enceladus. *Nature Astronomy*, *1*(12), 841–847. https://doi.org/10.1038/s41550-017-0289-8

Clancy, R. T., & Muhleman, D. O. (1985). Diurnal CO variations in the Venus mesophere from CO microwave spectra. *Icarus*, *64*(2), 157–182. https://doi.org/10.1016/0019-1035(85)90084-3

Clancy, R. T., Sandor, B. J., & Moriarty-Schieven, G. H. (2003). Observational definition of the Venus mesopause: Vertical structure, diurnal variation, and temporal instability. *Icarus*, *161*(1), 1–16. https://doi.org/10.1016/S0019-1035(02)00022-2

Cottini, V., Ignatiev, N. I., Piccioni, G., & Drossart, P. (2015). Water vapor near Venus cloud tops from VIRTIS-H/Venus express observations 2006–2011. *Planetary and Space Science*, *113–114*, 219–225. https://doi.org/10.1016/j.pss.2015.03.012

Cottini, V., Ignatiev, N. I., Piccioni, G., Drossart, P., Grassi, D., & Markiewicz, W. J. (2012). Water vapor near the cloud tops of Venus from Venus Express/VIRTIS dayside data. *Icarus*, *217*(2), 561–569.

Crisp, D. (1986). Radiative forcing of the Venus mesosphere: I. Solar fluxes and heating rates. *Icarus*, *67*(3), 484–514. https://doi.org/10.1016/0019-1035(86)90126-0

Encrenaz, T., Greathouse, T. K., Marcq, E., Sagawa, H., Widemann, T., Bézard, B., Fouchet, T., Lefèvre, F., Lebonnois, S., & Atreya, S. K. (2019). HDO and SO2 thermal mapping on Venus-IV. Statistical analysis of the SO2 plumes. *Astronomy & Astrophysics*, *623*, A70.

Encrenaz, T., Greathouse, T. K., Marcq, E., Sagawa, H., Widemann, T., Bézard, B., Fouchet, T., Lefèvre, F., Lebonnois, S., Atreya, S. K., Lee, Y. J., Giles, R., Watanabe, S., Shao, W., Zhang, X., & Bierson, C. J. (2020). HDO and SO2 thermal mapping on Venus—V. Evidence for a long-term anti-correlation. *Astronomy & Astrophysics*, *639*, A69. https://doi.org/10.1051/0004-6361/202037741

Encrenaz, T., Greathouse, T. K., Richter, M. J., DeWitt, C., Widemann, T., Bézard, B., Fouchet, T., Atreya, S. K., & Sagawa, H. (2016). HDO and SO2 thermal mapping on Venus—III. Short-term and long-term variations between 2012 and 2016. *Astronomy & Astrophysics*, *595*, A74. https://doi.org/10.1051/0004-6361/201628999

Encrenaz, T., Greathouse, T. K., Richter, M. J., Lacy, J., Widemann, T., Bézard, B., Fouchet, T., deWitt, C., & Atreya, S. K. (2013). HDO and SO2 thermal mapping on Venus—II. The SO2 spatial distribution above and within the clouds. *Astronomy & Astrophysics*, *559*, A65. https://doi.org/10.1051/0004-6361/201322264

Encrenaz, T., Greathouse, T. K., Roe, H., Richter, M., Lacy, J., Bézard, B., Fouchet, T., & Widemann, T. (2012). HDO and SO2 thermal mapping on Venus: Evidence for strong SO2 variability. *Astronomy & Astrophysics*, *543*, A153.

Encrenaz, T., Greathouse, T., Marcq, E., Sagawa, H., Widemann, T., Bezard, B., Fouchet, T., Lefèvre, F., Lebonnois, S., & Atreya, S. (2019). Ground-based mapping of SO2 and HDO on Venus in the thermal infrared. *EPSC-DPS Joint Meeting*, EPSC-DPS2019.

Esposito, L. W. (1984). Sulfur Dioxide: Episodic Injection Shows Evidence for Active Venus Volcanism. *Science*, *223*(4640), 1072–1074. https://doi.org/10.1126/science.223.4640.1072

Esposito, L. W., Copley, M., Eckert, R., Gates, L., Stewart, A. I. F., & Worden, H. (1988). Sulfur dioxide at the Venus cloud tops, 1978–1986. *Journal of Geophysical Research: Atmospheres*, *93*(D5), 5267–5276. https://doi.org/10.1029/JD093iD05p05267

Fedorova, A., Korablev, O., Vandaele, A.-C., Bertaux, J.-L., Belyaev, D., Mahieux, A., Neefs, E., Wilquet, W. V., Drummond, R., Montmessin, F., & Villard, E. (2008). HDO and H2O vertical distributions and isotopic ratio in the Venus mesosphere by Solar Occultation at Infrared spectrometer on board Venus Express. *Journal of Geophysical Research: Planets*, *113*(E5). https://doi.org/10.1029/2008JE003146

Fedorova, A., Marcq, E., Luginin, M., Korablev, O., Bertaux, J.-L., & Montmessin, F. (2016). Variations of water vapor and cloud top altitude in the Venus' mesosphere from SPICAV/VEx observations. *Icarus*, *275*, 143–162. https://doi.org/10.1016/j.icarus.2016.04.010

Fukuya, K., Imamura, T., Taguchi, M., Fukuhara, T., Kouyama, T., Horinouchi, T., Peralta, J., Futaguchi, M., Yamada, T., Sato, T. M., Yamazaki, A., Murakami, S., Satoh, T., Takagi, M., & Nakamura, M. (2021). The nightside cloud-top circulation of the atmosphere of Venus. *Nature*, *595*(7868), 511–515. https://doi.org/10.1038/s41586-021-03636-7

Fuller, J., Luan, J., & Quataert, E. (2016). Resonance locking as the source of rapid tidal migration in the Jupiter and Saturn moon systems. *Monthly Notices of the Royal Astronomical Society*, *458*(4), 3867–3879. https://doi.org/10.1093/mnras/stw609

Gao, P., Zhang, X., Crisp, D., Bardeen, C. G., & Yung, Y. L. (2014). Bimodal distribution of sulfuric acid aerosols in the upper haze of Venus. *Icarus*, *231*, 83–98. https://doi.org/10.1016/j.icarus.2013.10.013

Giese, B., Wagner, R., Hussmann, H., Neukum, G., Perry, J., Helfenstein, P., & Thomas, P. C. (2008). Enceladus: An estimate of heat flux and lithospheric thickness from flexurally supported topography. *Geophysical Research Letters*, *35*(24). https://doi.org/10.1029/2008GL036149

Gilli, G., Lebonnois, S., González-Galindo, F., López-Valverde, M. A., Stolzenbach, A., Lefèvre, F., Chaufray, J. Y., & Lott, F. (2017). Thermal structure of the upper atmosphere of Venus simulated by a ground-to-thermosphere GCM. *Icarus*, *281*, 55–72. https://doi.org/10.1016/j.icarus.2016.09.016

Gilli, G., Navarro, T., Lebonnois, S., Quirino, D., Silva, V., Stolzenbach, A., Lefèvre, F., & Schubert, G. (2021). Venus upper atmosphere revealed by a GCM: II. Model validation with temperature and density measurements. *Icarus*, 114432. https://doi.org/10.1016/j.icarus.2021.114432

Hansen, J. E., & Hovenier, J. W. (1974). Interpretation of the Polarization of Venus. *Journal of the Atmospheric Sciences*, *31*(4), 1137–1160. https://doi.org/10.1175/1520-0469(1974)031<1137:IOTPOV>2.0.CO;2

Hemingway, D., Iess, L., Tajeddine, R., & Tobie, G. (2018). The interior of Enceladus. *Enceladus and the Icy Moons of Saturn*, 57–77.

Hemingway, D. J., & Mittal, T. (2019). Enceladus's ice shell structure as a window on internal heat production. *Icarus*, *332*, 111–131. https://doi.org/10.1016/j.icarus.2019.03.011

Howett, C. J. A., Spencer, J. R., Pearl, J., & Segura, M. (2011). High heat flow from Enceladus' south polar region measured using 10–600 cm−1 Cassini/CIRS data. *Journal of Geophysical Research: Planets*, *116*(E3). https://doi.org/10.1029/2010JE003718

Hurford, T. A., Bills, B. G., Helfenstein, P., Greenberg, R., Hoppa, G. V., & Hamilton, D. P. (2009). Geological implications of a physical libration on Enceladus. *Icarus*, *203*(2), 541–552. https://doi.org/10.1016/j.icarus.2009.04.025

Iess, L., Stevenson, D. J., Parisi, M., Hemingway, D., Jacobson, R. A., Lunine, J. I., Nimmo, F., Armstrong, J. W., Asmar, S. W., Ducci, M., & Tortora, P. (2014). The Gravity Field and Interior Structure of Enceladus. *Science*, *344*(6179), 78–80. https://doi.org/10.1126/science.1250551

Ignatiev, N. i., Moroz, V. i., Zasova, L. V., & Khatuntsev, I. v. (1999). Water vapour in the middle atmosphere of Venus: An improved treatment of the Venera 15 ir spectra. *Planetary and Space Science*, *47*(8), 1061–1075. https://doi.org/10.1016/S0032-0633(99)00030-6

Imamura, T., Ando, H., Tellmann, S., Pätzold, M., Häusler, B., Yamazaki, A., Sato, T. M., Noguchi, K., Futaana, Y., Oschlisniok, J., Limaye, S., Choudhary, R. K., Murata, Y., Takeuchi, H., Hirose, C., Ichikawa, T., Toda, T., Tomiki, A., Abe, T., … Nakamura, M. (2017). Initial performance of the radio occultation experiment in the Venus orbiter mission Akatsuki. *Earth, Planets and Space*, *69*(1), 137. https://doi.org/10.1186/s40623-017-0722-3

Jessup, K. L., Marcq, E., Mills, F., Mahieux, A., Limaye, S., Wilson, C., Allen, M., Bertaux, J.-L., Markiewicz, W., Roman, T., Vandaele, A.-C., Wilquet, V., & Yung, Y. (2015). Coordinated Hubble Space Telescope and Venus Express Observations of Venus' upper cloud deck. *Icarus*, *258*, 309–336. https://doi.org/10.1016/j.icarus.2015.05.027

Jiang, X., Camp, C. D., Shia, R., Noone, D., Walker, C., & Yung, Y. L. (2004). Quasi-biennial oscillation and quasi-biennial oscillation–annual beat in the tropical total column ozone: A two-dimensional model simulation. *Journal of Geophysical Research: Atmospheres*, *109*(D16). https://doi.org/10.1029/2003JD004377

Kerzhanovich, V. V., & Limaye, S. S. (1985). Circulation of the atmosphere from the surface to 100 km. *Advances in Space Research*, *5*(11), 59–83. https://doi.org/10.1016/0273-1177(85)90198-X

Kite, E. S., & Rubin, A. M. (2016). Sustained eruptions on Enceladus explained by turbulent dissipation in tiger stripes. *Proceedings of the National Academy of Sciences*, *113*(15), 3972–3975. https://doi.org/10.1073/pnas.1520507113

Klinger, J. (1980). Influence of a Phase Transition of Ice on the Heat and Mass Balance of Comets. *Science*, *209*(4453), 271–272. https://doi.org/10.1126/science.209.4453.271

Knollenberg, R. G., & Hunten, D. M. (1980). The microphysics of the clouds of Venus: Results of the Pioneer Venus Particle Size Spectrometer Experiment. *Journal of Geophysical Research: Space Physics*, *85*(A13), 8039–8058. https://doi.org/10.1029/JA085iA13p08039

Krasnopolsky, V. A. (2010). Spatially-resolved high-resolution spectroscopy of Venus 2. Variations of HDO, OCS, and SO2 at the cloud tops. *Icarus*, *209*(2), 314–322. https://doi.org/10.1016/j.icarus.2010.05.008

Krasnopolsky, V. A. (2012). A photochemical model for the Venus atmosphere at 47–112km. *Icarus*, *218*(1), 230–246. https://doi.org/10.1016/j.icarus.2011.11.012

Krasnopolsky, V. A. (2013a). S3 and S4 abundances and improved chemical kinetic model for the lower atmosphere of Venus. *Icarus*, *225*(1), 570–580. https://doi.org/10.1016/j.icarus.2013.04.026

Krasnopolsky, V. A. (2013b). Nighttime photochemical model and night airglow on Venus. *Planetary and Space Science*, *85*, 78–88. https://doi.org/10.1016/j.pss.2013.05.022

Krasnopolsky, V. A. (2015). Vertical profiles of H2O, H2SO4, and sulfuric acid concentration at 45–75km on Venus. *Icarus*, *252*, 327–333. https://doi.org/10.1016/j.icarus.2015.01.024

Krasnopolsky, V. A. (2018). Disulfur dioxide and its near-UV absorption in the photochemical model of Venus atmosphere. *Icarus*, *299*, 294–299. https://doi.org/10.1016/j.icarus.2017.08.013

Krasnopolsky, V. A., Belyaev, D. A., Gordon, I. E., Li, G., & Rothman, L. S. (2013). Observations of D/H ratios in H2O, HCl, and HF on Venus and new DCl and DF line strengths. *Icarus*, *224*(1), 57–65. https://doi.org/10.1016/j.icarus.2013.02.010

Lainey, V., Casajus, L. G., Fuller, J., Zannoni, M., Tortora, P., Cooper, N., Murray, C., Modenini, D., Park, R. S., Robert, V., & Zhang, Q. (2020). Resonance locking in giant planets indicated by the rapid orbital expansion of Titan. *Nature Astronomy*, *4*(11), 1053–1058. https://doi.org/10.1038/s41550-020-1120-5

Lebonnois, S., Hourdin, F., Eymet, V., Crespin, A., Fournier, R., & Forget, F. (2010). Superrotation of Venus' atmosphere analyzed with a full general circulation

model. *Journal of Geophysical Research: Planets*, *115*(E6). https://doi.org/10.1029/2009JE003458

Lefèvre, M., Lebonnois, S., & Spiga, A. (2018). Three-Dimensional Turbulence-Resolving Modeling of the Venusian Cloud Layer and Induced Gravity Waves: Inclusion of Complete Radiative Transfer and Wind Shear. *Journal of Geophysical Research: Planets*, *123*(10), 2773–2789. https://doi.org/10.1029/2018JE005679

Lefèvre, M., Spiga, A., & Lebonnois, S. (2020). Mesoscale modeling of Venus' bow-shape waves. *Icarus*, *335*, 113376. https://doi.org/10.1016/j.icarus.2019.07.010

Lellouch, E., Goldstein, J. J., Rosenqvist, J., Bougher, S. W., & Paubert, G. (1994). Global Circulation, Thermal Structure, and Carbon Monoxide Distribution in Venus' Mesosphere in 1991. *Icarus*, *110*(2), 315–339. https://doi.org/10.1006/icar.1994.1125

Liao, Y., Nimmo, F., & Neufeld, J. A. (2020). Heat Production and Tidally Driven Fluid Flow in the Permeable Core of Enceladus. *Journal of Geophysical Research: Planets*, *125*(9), e2019JE006209. https://doi.org/10.1029/2019JE006209

Limaye, S. S. (2007). Venus atmospheric circulation: Known and unknown. *Journal of Geophysical Research: Planets*, *112*(E4). https://doi.org/10.1029/2006JE002814

Limaye, S. S., Grassi, D., Mahieux, A., Migliorini, A., Tellmann, S., & Titov, D. (2018). Venus Atmospheric Thermal Structure and Radiative Balance. *Space Science Reviews*, *214*(5), 102. https://doi.org/10.1007/s11214-018-0525-2

Luan, J., & Goldreich, P. (2017). Enceladus: Three-act play and current state. *AGU Fall Meeting Abstracts*, *51*. http://adsabs.harvard.edu/abs/2017AGUFM.P51F..04L

Mahieux, A., Wilquet, V., Vandaele, A. C., Robert, S., Drummond, R., Chamberlain, S., Grau Ribes, A., & Bertaux, J. L. (2015). Hydrogen halides measurements in the Venus mesosphere retrieved from SOIR on board Venus express. *Planetary and Space Science*, *113–114*, 264–274. https://doi.org/10.1016/j.pss.2014.12.014

Marcq, E., Baggio, L., Lefèvre, F., Stolzenbach, A., Montmessin, F., Belyaev, D., Korablev, O., & Bertaux, J.-L. (2019). Discovery of cloud top ozone on Venus. *Icarus*, *319*, 491–498. https://doi.org/10.1016/j.icarus.2018.10.006

Marcq, E., Bertaux, J.-L., Montmessin, F., & Belyaev, D. (2013). Variations of sulphur dioxide at the cloud top of Venus's dynamic atmosphere. *Nature Geoscience*, *6*(1), 25–28.

Marcq, E., Lea Jessup, K., Baggio, L., Encrenaz, T., Lee, Y. J., Montmessin, F., Belyaev, D., Korablev, O., & Bertaux, J.-L. (2020). Climatology of SO2 and UV absorber at Venus' cloud top from SPICAV-UV nadir dataset. *Icarus*, *335*, 113368. https://doi.org/10.1016/j.icarus.2019.07.002

McKinnon, W. B. (2015). Effect of Enceladus's rapid synchronous spin on interpretation of Cassini gravity. *Geophysical Research Letters*, *42*(7), 2137–2143. https://doi.org/10.1002/2015GL063384

Mendonça, J. M., & Buchhave, L. A. (2020). Modelling the 3D climate of Venus with oasis. *Monthly Notices of the Royal Astronomical Society*, *496*(3), 3512–3530. https://doi.org/10.1093/mnras/staa1618

Mendonça, J. M., & Read, P. L. (2016). Exploring the Venus global super-rotation using a comprehensive general circulation model. *Planetary and Space Science*, *134*, 1–18. https://doi.org/10.1016/j.pss.2016.09.001

Meyer, J., & Wisdom, J. (2007). Tidal heating in Enceladus. *Icarus*, *188*(2), 535–539. https://doi.org/10.1016/j.icarus.2007.03.001

Meyer, J., & Wisdom, J. (2008a). Tidal evolution of Mimas, Enceladus, and Dione. *Icarus*, *193*(1), 213–223. https://doi.org/10.1016/j.icarus.2007.09.008

Meyer, J., & Wisdom, J. (2008b). Episodic volcanism on Enceladus: Application of the Ojakangas–Stevenson model. *Icarus*, *198*(1), 178–180. https://doi.org/10.1016/j.icarus.2008.06.012

Mills, F. P. (1998). *I. Observations and photochemical modeling of the Venus middle atmosphere. II. Thermal infrared spectroscopy of Europa and Callisto* [PhD Thesis]. California Institute of Technology.

Mills, F. P., & Allen, M. (2007). A review of selected issues concerning the chemistry in Venus' middle atmosphere. *Planetary and Space Science*, *55*(12), 1729–1740. https://doi.org/10.1016/j.pss.2007.01.012

Na, C. Y., Esposito, L. W., & Skinner, T. E. (1990). International ultraviolet explorer observation of Venus SO2 and SO. *Journal of Geophysical Research: Atmospheres*, *95*(D6), 7485–7491. https://doi.org/10.1029/JD095iD06p07485

Navarro, T., Gilli, G., Schubert, G., Lebonnois, S., Lefèvre, F., & Quirino, D. (2021). Venus' upper atmosphere revealed by a GCM: I. Structure and variability of the circulation. *Icarus*, 114400. https://doi.org/10.1016/j.icarus.2021.114400

Nimmo, F., Barr, A. C., Běhounková, M., & McKinnon, W. B. (2018). The thermal and orbital evolution of Enceladus: Observational constraints and models. In *Enceladus and the Icy Moons of Saturn* (Vol. 475, pp. 79–94).

Ojakangas, G. W., & Stevenson, D. J. (1986). Episodic volcanism of tidally heated satellites with application to Io. *Icarus*, *66*(2), 341–358. https://doi.org/10.1016/0019-1035(86)90163-6

Ojakangas, G. W., & Stevenson, D. J. (1989). Thermal state of an ice shell on Europa. *Icarus*, *81*(2), 220–241. https://doi.org/10.1016/0019-1035(89)90052-3

Parkinson, C. D., Gao, P., Esposito, L., Yung, Y., Bougher, S., & Hirtzig, M. (2015). Photochemical control of the distribution of Venusian water. *Planetary and Space Science*, *113–114*, 226–236. https://doi.org/10.1016/j.pss.2015.02.015

Pechmann, J. B., & Ingersoll, A. P. (1984). Thermal Tides in the Atmosphere of Venus: Comparison of Model Results with Observations. *Journal of the Atmospheric Sciences*, *41*(22), 3290–3313. https://doi.org/10.1175/1520-0469(1984)041<3290:TTITAO>2.0.CO;2

Peralta, J., Luz, D., Berry, D. L., Tsang, C. C. C., Sánchez-Lavega, A., Hueso, R., Piccioni, G., & Drossart, P. (2012). Solar migrating atmospheric tides in the winds of the polar region of Venus. *Icarus*, *220*(2), 958–970. https://doi.org/10.1016/j.icarus.2012.06.015

Pollack, J. B., & Young, R. (1975). Calculations of the Radiative and Dynamical State of the Venus Atmosphere. *Journal of the Atmospheric Sciences*, *32*(6), 1025–1037. https://doi.org/10.1175/1520-0469(1975)032<1025:COTRAD>2.0.CO;2

Prather, M. J. (1986). Numerical advection by conservation of second-order moments. *Journal of Geophysical Research: Atmospheres*, *91*(D6), 6671–6681. https://doi.org/10.1029/JD091iD06p06671

Rambaux, N., Castillo-Rogez, J. C., Williams, J. G., & Karatekin, Ö. (2010). Librational response of Enceladus. *Geophysical Research Letters*, *37*(4). https://doi.org/10.1029/2009GL041465

Rambaux, N., Hoolst, T. V., & Karatekin, Ö. (2011). Librational response of Europa, Ganymede, and Callisto with an ocean for a non-Keplerian orbit. *Astronomy & Astrophysics*, *527*, A118. https://doi.org/10.1051/0004-6361/201015304

Roberts, J. H. (2015). The fluffy core of Enceladus. *Icarus*, *258*, 54–66. https://doi.org/10.1016/j.icarus.2015.05.033

Roberts, J. H., & Nimmo, F. (2008). Tidal heating and the long-term stability of a subsurface ocean on Enceladus. *Icarus*, *194*(2), 675–689. https://doi.org/10.1016/j.icarus.2007.11.010

Roberts, J. H., & Stickle, A. M. (2021). Breaking the symmetry by breaking the ice shell: An impact origin for the south polar terrain of Enceladus. *Icarus*, *359*, 114302. https://doi.org/10.1016/j.icarus.2021.114302

Rovira-Navarro, M., Gerkema, T., Maas, L. R. M., van der Wal, W., van Ostayen, R., & Vermeersen, B. (2020). Tides in subsurface oceans with meridional varying thickness. *Icarus*, *343*, 113711. https://doi.org/10.1016/j.icarus.2020.113711

Rovira-Navarro, M., Rieutord, M., Gerkema, T., Maas, L. R. M., van der Wal, W., & Vermeersen, B. (2019). Do tidally-generated inertial waves heat the subsurface oceans of Europa and Enceladus? *Icarus*, *321*, 126–140. https://doi.org/10.1016/j.icarus.2018.11.010

Sánchez-Lavega, A., Hueso, R., Piccioni, G., Drossart, P., Peralta, J., Pérez-Hoyos, S., Wilson, C. F., Taylor, F. W., Baines, K. H., Luz, D., Erard, S., & Lebonnois, S. (2008). Variable winds on Venus mapped in three dimensions. *Geophysical Research Letters*, *35*(13). https://doi.org/10.1029/2008GL033817

Sandor, B. J., & Clancy, R. T. (2005). Water vapor variations in the Venus mesosphere from microwave spectra. *Icarus*, *177*(1), 129–143. https://doi.org/10.1016/j.icarus.2005.03.020

Sandor, B. J., & Clancy, R. T. (2012). Observations of HCl altitude dependence and temporal variation in the 70–100km mesosphere of Venus. *Icarus*, *220*(2), 618–626. https://doi.org/10.1016/j.icarus.2012.05.016

Sandor, B. J., & Clancy, R. T. (2017). Diurnal observations of HCl altitude variation in the 70–100 km mesosphere of Venus. *Icarus*, *290*, 156–161. https://doi.org/10.1016/j.icarus.2017.02.017

Sandor, B. J., & Clancy, R. T. (2018). First measurements of ClO in the Venus atmosphere – Altitude dependence and temporal variation. *Icarus*, *313*, 15–24. https://doi.org/10.1016/j.icarus.2018.04.022

Sandor, B. J., Clancy, R. T., & Moriarty-Schieven, G. (2012). Upper limits for H2SO4 in the mesosphere of Venus. *Icarus*, *217*(2), 839–844. https://doi.org/10.1016/j.icarus.2011.03.032

Sandor, B. J., Todd Clancy, R., Moriarty-Schieven, G., & Mills, F. P. (2010). Sulfur chemistry in the Venus mesosphere from SO2 and SO microwave spectra. *Icarus*, *208*(1), 49–60. https://doi.org/10.1016/j.icarus.2010.02.013

Shao, W. D., Zhang, X., Bierson, C. J., & Encrenaz, T. (2020). Revisiting the Sulfur-Water Chemical System in the Middle Atmosphere of Venus. *Journal of Geophysical Research: Planets*, *125*(8), e2019JE006195. https://doi.org/10.1029/2019JE006195

Shia, R.-L., Ha, Y. L., Wen, J.-S., & Yung, Y. L. (1990). Two-dimensional atmospheric transport and chemistry model: Numerical experiments with a new advection algorithm. *Journal of Geophysical Research: Atmospheres*, *95*(D6), 7467–7483. https://doi.org/10.1029/JD095iD06p07467

Shia, R.-L., Yung, Y. L., Allen, M., Zurek, R. W., & Crisp, D. (1989). Sensitivity study of advection and diffusion coefficients in a two-dimensional stratospheric model using excess carbon 14 data. *Journal of Geophysical Research: Atmospheres*, *94*(D15), 18467–18484. https://doi.org/10.1029/JD094iD15p18467

Shoji, D., Hussmann, H., Kurita, K., & Sohl, F. (2013). Ice rheology and tidal heating of Enceladus. *Icarus*, *226*(1), 10–19. https://doi.org/10.1016/j.icarus.2013.05.004

Shoji, D., Hussmann, H., Sohl, F., & Kurita, K. (2014). Non-steady state tidal heating of Enceladus. *Icarus*, *235*, 75–85. https://doi.org/10.1016/j.icarus.2014.03.006

Smyshlyaev, S. P., Dvortsov, V. L., Geller, M. A., & Yudin, V. A. (1998). A two-dimensional model with input parameters from a general circulation model: Ozone sensitivity to different formulations for the longitudinal temperature variation. *Journal of Geophysical Research: Atmospheres*, *103*(D21), 28373–28387. https://doi.org/10.1029/98JD02354

Souček, O., Hron, J., Běhounková, M., & Čadek, O. (2016). Effect of the tiger stripes on the deformation of Saturn's moon Enceladus. *Geophysical Research Letters*, *43*(14), 7417–7423. https://doi.org/10.1002/2016GL069415

Spencer, J. R., Howett, C. J. A., Verbiscer, A., Hurford, T. A., Segura, M., & Spencer, D. C. (2013). *Enceladus heat flow from high spatial resolution thermal emission observations. 8*, 840–841.

Spencer, J. R., Pearl, J. C., Segura, M., Flasar, F. M., Mamoutkine, A., Romani, P., Buratti, B. J., Hendrix, A. R., Spilker, L. J., & Lopes, R. M. C. (2006). Cassini Encounters Enceladus: Background and the Discovery of a South Polar Hot Spot. *Science*, *311*(5766), 1401–1405. https://doi.org/10.1126/science.1121661

Stolzenbach, A. (2016). *Etude de la photochimie de Vénus à l'aide d'un modèle de circulation générale* [These de doctorat, Paris 6]. https://www.theses.fr/2016PA066413

Stolzenbach, A., Lefèvre, F., Lebonnois, S., Maattanen, A. E., & Bekki, S. (2015). Three-Dimensional Modelling of Venus Photochemistry. *AGU Fall Meeting Abstracts*, *23*, P23A-2108.

Taylor, F. W., Beer, R., Chahine, M. T., Diner, D. J., Elson, L. S., Haskins, R. D., McCleese, D. J., Martonchik, J. V., Reichley, P. E., Bradley, S. P., Delderfield, J., Schofield, J. T., Farmer, C. B., Froidevaux, L., Leung, J., Coffey, M. T., & Gille, J. C. (1980). Structure and meteorology of the middle atmosphere of Venus: Infrared remote sensing from the Pioneer Orbiter. *Journal of Geophysical Research: Space Physics*, *85*(A13), 7963–8006. https://doi.org/10.1029/JA085iA13p07963

Tellmann, S., Pätzold, M., Häusler, B., Bird, M. K., & Tyler, G. L. (2009). Structure of the Venus neutral atmosphere as observed by the Radio Science experiment VeRa on Venus Express. *Journal of Geophysical Research: Planets*, *114*(E9). https://doi.org/10.1029/2008JE003204

Thomas, P. C., Tajeddine, R., Tiscareno, M. S., Burns, J. A., Joseph, J., Loredo, T. J., Helfenstein, P., & Porco, C. (2016). Enceladus's measured physical libration requires a global subsurface ocean. *Icarus*, *264*, 37–47. https://doi.org/10.1016/j.icarus.2015.08.037

Tiscareno, M. S., Thomas, P. C., & Burns, J. A. (2009). The rotation of Janus and Epimetheus. *Icarus*, *204*(1), 254–261. https://doi.org/10.1016/j.icarus.2009.06.023

Tobie, G., Mocquet, A., & Sotin, C. (2005). Tidal dissipation within large icy satellites: Applications to Europa and Titan. *Icarus*, *177*(2), 534–549. https://doi.org/10.1016/j.icarus.2005.04.006

Tyler, R. (2011). Tidal dynamical considerations constrain the state of an ocean on Enceladus. *Icarus*, *211*(1), 770–779. https://doi.org/10.1016/j.icarus.2010.10.007

Van Hoolst, T., Baland, R.-M., & Trinh, A. (2013). On the librations and tides of large icy satellites. *Icarus*, *226*(1), 299–315. https://doi.org/10.1016/j.icarus.2013.05.036

Van Hoolst, T., Baland, R.-M., & Trinh, A. (2016). The diurnal libration and interior structure of Enceladus. *Icarus*, *277*, 311–318. https://doi.org/10.1016/j.icarus.2016.05.025

Van Hoolst, T., Rambaux, N., Karatekin, Ö., & Baland, R.-M. (2009). The effect of gravitational and pressure torques on Titan's length-of-day variations. *Icarus*, *200*(1), 256–264. https://doi.org/10.1016/j.icarus.2008.11.009

Van Hoolst, T., Rambaux, N., Karatekin, Ö., Dehant, V., & Rivoldini, A. (2008). The librations, shape, and icy shell of Europa. *Icarus*, *195*(1), 386–399. https://doi.org/10.1016/j.icarus.2007.12.011

Vandaele, A. C., Korablev, O., Belyaev, D., Chamberlain, S., Evdokimova, D., Encrenaz, T., Esposito, L., Jessup, K. L., Lefèvre, F., & Limaye, S. (2017a). Sulfur dioxide in the Venus atmosphere: I. Vertical distribution and variability. *Icarus*, *295*, 16–33.

Vandaele, A. C., Korablev, O., Belyaev, D., Chamberlain, S., Evdokimova, D., Encrenaz, T., Esposito, L., Jessup, K. L., Lefèvre, F., & Limaye, S. (2017b). Sulfur dioxide in the Venus Atmosphere: II. Spatial and temporal variability. *Icarus*, *295*, 1–15.

Vandaele, A. C., Mahieux, A., Chamberlain, S., Ristic, B., Robert, S., Thomas, I. R., Trompet, L., Wilquet, V., & Bertaux, J. L. (2016). Carbon monoxide observed in Venus' atmosphere with SOIR/VEx. *Icarus*, *272*, 48–59. https://doi.org/10.1016/j.icarus.2016.02.025

von Zahn, U., Krankowsky, D., Mauersberger, K., Nier, A. O., & Hunten, D. M. (1979). Venus Thermosphere: In situ Composition Measurements, the Temperature Profile, and the Homopause Altitude. *Science*, *203*(4382), 768–770. https://doi.org/10.1126/science.203.4382.768

Wilson, A., & Kerswell, R. R. (2018). Can libration maintain Enceladus's ocean? *Earth and Planetary Science Letters*, *500*, 41–46. https://doi.org/10.1016/j.epsl.2018.08.012

Wisdom, J. (2004). Spin-Orbit Secondary Resonance Dynamics of Enceladus. *The Astronomical Journal*, *128*(1), 484. https://doi.org/10.1086/421360

Woo, R., & Ishimaru, A. (1981). Eddy diffusion coefficient for the atmosphere of Venus from radio scintillation measurements. *Nature*, *289*(5796), 383–384. https://doi.org/10.1038/289383a0

Young, A. T. (1973). Are the clouds of venus sulfuric acid? *Icarus*, *18*(4), 564–582. https://doi.org/10.1016/0019-1035(73)90059-6

Yung, Y. L., & DeMore, W. B. (1982). Photochemistry of the stratosphere of Venus: Implications for atmospheric evolution. *Icarus*, *51*(2), 199–247.

Zasova, L. V., Ignatiev, N., Khatuntsev, I., & Linkin, V. (2007). Structure of the Venus atmosphere. *Planetary and Space Science*, *55*(12), 1712–1728. https://doi.org/10.1016/j.pss.2007.01.011

Zasova, L. V., Khatountsev, I. V., Ignatiev, N. I., & Moroz, V. I. (2002). Local time variations of the middle atmosphere of Venus: Solar-related structures. *Advances in Space Research*, *29*(2), 243–248. https://doi.org/10.1016/S0273-1177(01)00574-9

Zhang, X., Liang, M. C., Mills, F. P., Belyaev, D. A., & Yung, Y. L. (2012). Sulfur chemistry in the middle atmosphere of Venus. *Icarus*, *217*(2), 714–739.

Zhang, X., Liang, M.-C., Montmessin, F., Bertaux, J.-L., Parkinson, C., & Yung, Y. L. (2010). Photolysis of sulphuric acid as the source of sulphur oxides in the mesosphere of Venus. *Nature Geoscience*, *3*(12), 834–837.

Zhang, X., Shia, R.-L., & Yung, Y. L. (2013). JOVIAN STRATOSPHERE AS A CHEMICAL TRANSPORT SYSTEM: BENCHMARK ANALYTICAL SOLUTIONS. *The Astrophysical Journal*, *767*(2), 172. https://doi.org/10.1088/0004-637X/767/2/172

Zhang, X., & Showman, A. P. (2018). Global-mean Vertical Tracer Mixing in Planetary Atmospheres. I. Theory and Fast-rotating Planets. *The Astrophysical Journal*, *866*(1), 1. https://doi.org/10.3847/1538-4357/aada85